Politecnico di Milano

Scuola di Ingegneria Industriale e dell'Informazione

Corso di Laurea Magistrale in Ingegneria Fisica

FABRICATION OF A POLARIZATION INSENSITIVE PHOTONIC LATTICE FOR PERFECT STATE TRANSFER EXPERIMENTS

Relatore:

Prof. Roberto OSELLAME

Correlatore:

Dott. Andrea CRESPI

Candidato:

Matteo SANTANDREA

Matr. 797484

Anno Accademico 2013/2014

Wisdom is not the product of schooling,
but of the lifelong attempt to acquire it.
(A. Einstein)

Contents

List of Figures

List of Tables

Abstract

One of the most promising innovations of the quantum information theory - which merges quantum physics with classical information theory - is the realization of a quantum computer, that should enable to overcome the limitations of classical computers. Like their classical counterparts, quantum computer will most likely be constituted by processors and memories that will store and elaborate data, and by some physical channels that enable the communications among the processors, the memories and other peripherals.

An interesting solution for the implementation of data bus in quantum computers is the exploitation of the characteristics of spin chains to enable high-fidelity transmission of one or more quantum states from one end of the chain to the other. A number of theoretical works on the properties of spin chains and on the communication protocols available on these systems have been published in the last ten years, but the practical implementation of these studies is still difficult to achieve. For this reason, in the last few years there has been an active interest in simulating these systems with photonic devices to study experimentally their properties.

This has been possible also thanks to the peculiar properties of the femtosecond laser writing technology. This technology allows to induce a permanent local modification of the refractive index of a glass substrate, thus allowing the realization of structures that can guide light radiation, from simple waveguides to more complex photonic structures.

The experimental activity of this thesis is centred on the fabrication of a quantum optical analogue of a spin chain using the femtosecond laser technology. This device will constitute the main component of an experiment performed at the Quantum Photonics Lab of the Sydney University, whose aim is to study experimentally the evolution of entangled states into spin chain by means of photonic simulators.

The first part of this thesis aims to introduce and motivate theoretical and experimental research on spin chains and to present the techniques employed in the fabrication and characterization of the photonic devices, while the second part will address the realization and the analysis of these devices.

In the *first chapter* we review some of the main concepts at the basis of quantum information theory, we describe the main technological platforms for the implementation of quantum computers and we introduce the issue of quantum state transfer between the components of quantum computers.

The *second chapter* is centred on spin chains: we describe some typologies of spin chains, analyse the problems connected to the transfer of quantum states between the edges of the chain and discuss how these system can be simulated through photonic devices.

In the *third chapter*, the femtosecond laser writing technology is described and some devices realized are shown to underline the versatility and the capabilities of this technology.

The *fourth chapter* describes the writing and characterization setup used throughout the thesis activity to fabricate and analyse the devices.

In the *fifth chapter* we briefly describe the experiment that will be performed at the Quantum Photonics Lab in Sydney to identify the minimal characteristics of the device we are going to design.

The *sixth chapter* describes the design and realization of a first prototype, whose non-idealities are analysed through numerical simulations in the *seventh chapter*.

In the *eighth chapter* we study experimentally some possible causes of non-ideality of the device and we propose a possible engineering of the structure to overcome these issues.

Finally, in the *appendices* there are a short summary of the main properties of the Pauli matrices and the mathematical discussion of the spin chain Hamiltonian of interest in this thesis.

Introduzione

Una delle più attese innovazioni promesse dalla teoria quantistica dell'informazione - la teoria nata fondendo la fisica quantistica con la teoria classica dell'informazione - è l'implementazione di un calcolatore quantistico, che abbatterebbe diversi limiti computazionali dei calcolatori disponibili attualmente. Come per i loro corrispettivi classici, i calcolatori quantistici saranno probabilmente costituiti da processori e memorie, per l'elaborazione e l'immagazzinamento dei dati, e da *bus dati* per permettere la comunicazione tra i processori, le memorie e le altre periferiche.

Per quanto riguarda l'implementazione dei *bus dati*, un'interessante soluzione teorica è l'utilizzo di catene di spin adeguatamente ingegnerizzate per consentire la trasmissione fedele di uno o più stati quantistici da un capo all'altro della catena in un tempo prefissato. Sono stati condotti numerosi studi teorici negli ultimi dieci anni, ma l'implementazione di tali sistemi è ancora molto difficoltosa. Per tale ragione, al fine di studiare le proprietà di questi sistemi, negli ultimi anni si è iniziato a simularli mediante dispositivi fotonici.

Ciò è stato possibile anche grazie alle particolari proprietà della tecnologia della scrittura laser a femtosecondi. Essa permette, infatti, di ottenere una modifica locale e permanente dell'indice di rifrazione di un substrato vetroso sfruttando un fascio laser a femtosecondi focalizzato, consentendo dunque la fabbricazione di strutture in grado di guidare la radiazione luminosa, da singole guide d'onda a strutture fotoniche più complesse.

L'attività sperimentale di questa tesi è incentrata sulla fabbricazione mediante laser a femtosecondi di un dispositivo fotonico che simuli una catena di spin. Questo dispositivo è il componente principale di un esperimento, svolto presso il Quantum Photonics Lab dell'Università di Sydney, il cui scopo è quello di studiare sperimentalmente l'evoluzione di stati entangled

nelle catene di spin.

La prima parte di questa tesi è finalizzata a contestualizzare e motivare la ricerca teorica e sperimentale sulle catene di spin e di presentare i metodi di fabbricazione e caratterizzazione dei dispositivi fotonici, la cui realizzazione verrà discussa nella seconda parte.

Nel *primo capitolo* vengono discussi alcuni dei concetti alla base della teoria quantistica dell'informazione, vengono descritte le principali piattaforme tecnologiche per l'implementazione di computer quantistici e si accenna alle problematiche del trasporto di stati quantistici all'interno di un calcolatore quantistico.

Nel *secondo capitolo* si affronta la descrizione delle catene di spin, si analizza la problematica del trasferimento di uno stato quantistico all'interno di questi sistemi e si discute la possibilità di simularli mediante dispositivi fotonici.

All'interno del *terzo capitolo* viene descritta la tecnica di fabbricazione a femtosecondi e vengono mostrati alcuni esempi di strutture fotoniche realizzate con questa tecnologia per mostrarne la versatilità e le potenzialità.

Il *quarto capitolo* è dedicato alla descrizione dei setup di scrittura e di caratterizzazione dei dispositivi fabbricati nel corso della tesi.

Nel *quinto capitolo* è trattato brevemente l'esperimento condotto a Sydney al fine di identificare i requisiti minimi dei dispositivi da fabbricare.

Il *sesto capitolo* è incentrato sulla realizzazione di un primo prototipo del dispositivo fotonico che simula la catena di spin.

Le non idealità del dispositivo realizzato vengono analizzate mediante simulazioni numeriche nel *settimo capitolo*.

Nell'*ottavo capitolo* vengono infine studiati in dettaglio le possibili cause di non idealità del dispositivo mendiante esperimenti mirati e viene proposto una possibile ingegnerizzazione per superare i limiti identificati.

Infine, nelle *appendici* ci sono una breve ricapitolazione delle proprietà principali delle matrici di Pauli e la trattazione matematica del sistema di catene di spin che interessa maggiormente il lavoro di questa tesi.

Part I

Background

Chapter 1

Quantum information

1.1 The science of information

Since the first steps of mankind on Earth, we have managed to survive into the wild thanks to our ability to gather and process information. The capability to codify the world around us in order to recognize its threats and opportunities and the capability to process and share this knowledge with our kins has allowed us to evolve and rise above all the other animals in the world. The number of soldiers in an enemy army, the time needed for a crop to grow, the amount of wheat stocked in the storehouse of a city, the timetable of a train are but a few examples of what information is to us. Anyway, information is nothing without the technology to deal with it. How could we elaborate and transmit data without the ability to represent and process them physically? Thus, the need to share public and private data has been a driver to develop new languages, new technologies, new alphabets, new cyphers. In a way, information shaped technology. But also the contrary is true: as our ability to build more complex devices evolved, it changed also the way we conceive information. This can be easily seen from the history of cryptography: from the first scytale used by the Romans, based on a cylinder with a strip of paper rolled onto it, to the Enigma machine used during World War II, the cryptographic algorithms had to keep the pace of the technological development, culminated in the 20th century with the advent of the computer.

One of the most striking example of how technology shapes the way we think data and data processing is the dramatic change of paradigm that

invested the world of information in the '70s. Until then, information has always been thought as a classic entity. Quantum physics was helpful in building more powerful computers, but its application was limited only to hardware design. When, in the second half of 20th century, scientists had to face the limits of classical computers, they started thinking whether the laws of quantum physics could change the way we intend and process information. Since the realization that the classical Shannon theory of information could not be generalized to quantum systems [1], a full quantum theory of information and information processing has been developed [2], as well as a large plethora of devices that implement this theory.

Here we mention but few examples to show the improvements that quantum theory of information offers with respect to classical theories.

Factorization of large integers. Shor's quantum algorithm for factorizing large numbers [3, 4] is a demonstration of how even a modest-size quantum computer could in principle outperform its classical counterpart: it can factorize a large integer N in a polynomial time (that is, polynomial in $\log N$), while the fastest known classical algorithm, the *general number sieve*, works in sub-exponential time [5]. This would pose a serious threat to current encryption methods, like RSA, that rely on the fact that factorization of large number is hugely demanding on classical computer and supercomputers.

Simulation of quantum systems. In the '80s, Feynman [6] highlighted that a classical computer cannot describe efficiently large quantum systems, since the required resources increase exponentially with the complexity of the systems; for this reason, he envisioned the employment of a device based on the laws of quantum physics to simulate the quantum system of interest with greater precision and efficiency.

Several simulations of quantum systems have already been successfully implemented [7–9]; anyway, the efficiency of these *quantum simulators* is still below the classical limit.

Quantum key distribution. Quantum key distribution (QKD) is an important branch of quantum cryptography and it studies how to share a perfect secure cryptographic key between two parties, usually labelled as Alice,

the sender, and Bob, the receiver. In 1984, Bennet and Brassard proposed the first algorithm for QKD, known as BB84, and showed that it was theoretically unbreakable [10, 11]. In 1992, they demonstrated the validity of their protocol through a physical implementation [12], posing an important milestone in this field.

To understand better why quantum information processing (QIP) and quantum computers are such a breakthrough, we need to understand what makes them so different from their classical counterparts.

1.2 The fundamental units of quantum information

The key difference between classical and quantum theory of information is the way data is described and processed [13, 14].

Classical computers represent data as sequences of bits - collections of 0s and 1s. Any physical system that presents two macroscopic states separated by an energy barrier large enough to prevent spontaneous transitions from one state to the other can be used to implement a classical bit: a light bulb can be on or off, a voltage can be high or low (for example 5 V and 0 V) and so on. In this way, a n-bit system can represent a set of 2^n discrete logical state, from $0000\ldots00$ to $1111\ldots11$.

In quantum theory of information, data are described by quantum bits, or *qubits*. A qubit is generally defined as a system with two different quantum states, which can be labelled for simplicity $|0\rangle$ and $|1\rangle$. Qubits can be implemented in several physical systems, such as photons, ions and atoms (the most important will be reviewed in the following); moreover, within these systems, qubits can be encoded in different degrees of freedom - e.g., they can be encoded in photon polarization, in their angular momentum or in the path they are travelling (linear momentum). Qubits exhibit three peculiar behaviours that make them radically different from classical bits: coherent superposition, entanglement and the impossibility of cloning. We will explain these features in the following, considering qubits encoded in the polarization of photons.

Coherent superposition of states.

Coherent superposition of states is a direct consequence of the linearity of quantum physics. In the following, we will identify the boolean states 0 and 1 with the horizontal and vertical polarization of one photon: $|H\rangle = |0\rangle$ and $|V\rangle = |1\rangle$. Starting from this *basis set*, the linearity of quantum mechanics allows to construct qubits that are in a continuum of intermediate states. This is obtained through a complex linear combination of the basis set states, i.e.

$$|\psi\rangle = \alpha\,|0\rangle + \beta\,|1\rangle \tag{1.1}$$

where α and β are complex number that must satisfy $|\alpha|^2 + |\beta|^2 = 1$.

One may think that also classical bits have a continuum of states: actually, it is the physical variable, which encodes the classical bit, that can assume a continuum of values but the logical value of the bit is discrete, since it is always relative to one (or more) fixed threshold. On the other hand, for qubits, it is their logical value that is in a continuum of states.

Another important aspect of superposition is that it literally expands the space where calculation is performed: a string of n bits can be in 2^n different *states*, while a string of n qubits can be any state described by a complex, unitary vector in a 2^n *dimensions* Hilbert space. In other words, a string of n bits can be in all states spanning from $000\ldots00$ to $111\ldots11$, while a string of n qubits can be in all states described by

$$|\Psi\rangle = \sum_{x=000\ldots00}^{111\ldots11} c_x\,|x\rangle \tag{1.2}$$

as long as $\sum_{x=000\ldots00}^{111\ldots11} |c_x|^2 = 1$.

For example, two classical bits can be in one of the states 00, 01, 10 and 11, while two qubits can be in every state describable by $|\Psi\rangle = \alpha\,|00\rangle + \beta\,|01\rangle + \gamma\,|10\rangle + \delta\,|11\rangle$. The classical 2-bit system operates in a 2-dimensional space, while the 2-qubit system operates in a 4-dimensional space. It is evident that the dimensions of the space in which the computation is performed depend linearly on the number of bits in the classical case and exponentially in the quantum one. Anyway, it is important to underline that from an n-qubit system can be *accessed* (or retrieved) exactly the same quantity of information as from an n-bit classical system. This is a consequence of the

Holevo's theorem [15] and it is related to the fact that to access the information represented by a n-qubit it is necessary to measure the qubits: this operation destroys the coherent superposition of the qubits and collapses their states to either $|0\rangle$ or $|1\rangle$ so that, at the end, the set of the possible outcomes is the set of the possible n-bit states. Thus, the improvement granted by a quantum computer is not related to the amount of information retrieved but to the way it is processed.

Entanglement.

When two or more particles are generated or interact simultaneously, they form a new system, which can be described by a wavefunction $|\Psi\rangle$. In some particular cases, the particles can be distinguished after the interaction: in these cases, the wavefunction of the state of the whole system can be described by the tensor product of the single components of the system

$$\Psi = \otimes_{n=1}^{N} |x_n\rangle = |x_1\rangle \otimes |x_2\rangle \otimes \ldots \otimes |x_N\rangle \tag{1.3}$$

For example, after an interaction, if you could distinguish that photon A has horizontal polarization and photon B has vertical polarization, then the final state of the whole system is $|\Psi\rangle = |HV\rangle = |H\rangle_A \otimes |V\rangle_B$.

More generally, though, it is impossible to describe the system with such decomposition. For example, consider the spontaneous parametric down conversion (SPDC) in a beta-barium borate (BBO) crystal, in which a high intensity laser beam is directed onto the crystal and occasionally a single photon splits into two photons, $\hbar\omega_0 \to \hbar\omega_1 + \hbar\omega_2$. In type II SPDC, these photons have the property that if one is found to have vertical polarization, the other has horizontal polarization, and viceversa. The peculiarity is that, while this relationship is certain, there is no way to predict which photon will be measured as horizontally polarized and which will be measured as vertically polarized[1].

The system of the two photons we are considering can be described by the wavefunction

$$|X\rangle = \frac{|H_A V_B\rangle + e^{i\alpha} |V_A H_B\rangle}{\sqrt{2}} \tag{1.4}$$

[1]Note that quantum physics says that, until you perform a measurement, the photons will have no defined polarization, so there is no point in asking what is the polarization of that photon: the correct question is what is the outcome of the measurement.

which cannot be decomposed any more in the tensor product of the two particles: the particles are *entangled*.

The strangeness of entanglement lies in the fact that, once the particles become entangled, they start behaving as a single system, independently on how far they are: as soon as one particle is measured, the wavefunction of the system collapses and the other particle *instantly* assumes a determined state, depending on the outcome of the measurement. This may seem to violate Einstein's theory of relativity, but since it is impossible to retrieve information from an entangled system without a classically-assisted communication, special relativity is not violated.

Entanglement is important because it is one of the key elements of quantum teleportation and QKD protocols [12, 16],

No cloning theorem.

Classical bits can be easily copied by measuring their state and then replicating it with another system: for example, a simple measurement of voltage give access to the logical value of the bit and then it can be generated again with another voltage source. On the other hand, quantum states cannot be cloned, i.e. it is impossible to make an exact copy of a quantum system without somehow changing it [17].

This has profound implication on the quantum theory of information. For example, the simplest way to reduce errors in classical communications is to have *redundancy*, i.e. 0 is coded as 000 and 1 as 111; as a consequence of the no cloning theorem, the mere application of this protocol is impossible for qubits, since it is impossible to clone the state of a qubit to exploit redundancy ($|\psi\rangle \nrightarrow |\psi\psi\psi\rangle$), so new protocols had to be studied to reduce errors. Another example is related to QKD: the no cloning theorem implies that an eavesdropper cannot copy faithfully the qubits of the communication without changing their characteristics, theoretically enabling the two parties to recognize if someone is listening to their communication and interrupt the unsafe transmission.

Decoherence

From what stated before, it appears that quantum systems are very fragile and complex to handle. This is true especially when we consider interaction

with the environment. In fact, every non-isolated quantum system suffers the phenomenon known as *decoherence*. One way to interpret decoherence is to consider it as the leakage of the information stored into a quantum system: the interaction of the system with the environment entangles these two entities, so that the information now is distributed in the whole environment, thus preventing the possibility of a correct retrieval of the data [13]. Even though this may seem to be an insurmountable hindrance towards the realization of a quantum computer, there are strategies to overcome this problem.

Obviously, since the main issue is the environment, the first way to reduce decoherence is to choose an implementation that interacts as little as possible with the surrounding systems - but this is not an easy task. Another possibility is to implement a quantum computer exploiting *quantum error correction* (QEC) techniques and *quantum fault-tolerant computation* (QFTC)[18]. They are both techniques that encode informations in such ways that enable data retrieval even if some errors occurs. The main concept is to encode information into an entangled state involving a large number of qubits. In this way, one cannot directly access the data, since it is spread all over the entangled system, but for exactly the same reason, data cannot be degraded much - if the interaction of the system with the environment is limited to a few qubits.

1.3 Quantum hardware

The big promise of quantum information theory is the realization of the quantum computer. Like its classical counterpart, a quantum computer will most likely consist of some processors (both active elements, like quantum gates, and passive elements, like quantum memories), that will perform quantum operations on the qubits, and some channels that will share data between the processors and send it to other peripherals.

In classical computers, both the processors and the communication channels are implemented using semiconductors and employ voltages to represent data. For quantum computers, there is not a “canonical” architecture and a wide variety of possible physical implementations has been proposed. We will shortly review here some, following Ladd *et al.* [14].

Photons. Qubits can be encoded in photons in different ways, e.g. in their polarization or in the path they are travelling. The main advantage using photons as qubits is their low interaction with the environment, leading to long decoherence times. For the same reason, one may think that effective interaction between photons is possible only exploiting optical nonlinearities, which is a quite hard task. This conception was broken by the KLM scheme [19] by Knill, Laflamme and Milburn, that showed that it is possible to implement a quantum computer using only single-photon sources and detectors and linear optical circuits. However, despite this major theoretical discovery, there are still limitations in the implementation of architectures based on photons, mainly due to the low efficiency of single-photon sources and detectors and photon losses.

Nuclear magnetic resonance (NMR). Qubits can be effectively encoded in the nuclear spins of atoms in dissolved molecules or in solids. In the future, these systems might constitute the basis of quantum computers thanks to the well-established magnetic resonance technology employed to manipulate them.

In NMR, it is possible to recognize and manipulate nuclear spin through their unique Larmor frequency[2]. Moreover, in a dissolved molecule it is possible to discern the spin of the same atomic species thanks to their chemical shift, i.e. the shift of the Larmor frequency due to the interactions with the different local environments, and this increases the number of physical systems that can store qubits. Nuclear spins can be manipulated using rf pulses to create one-qubit gates and exploiting indirect coupling to realize two-qubit interactions.

Liquid-state NMR has allowed the realization of quantum processors with dozen of qubits [20] and the implementation of several algorithms, e.g. Deutsch's algorithm [21, 22] , Grover's quantum search algorithm [23] and Shor's factorization algorithm [24]. However, the main issues that prevent the construction of large architectures based on liquid-state NMR are the ineffective initialization of the system, i.e. the difficulty in setting the system to an initial known ground state, and the scalability of this technique, since there is an exponential decrease of signal for every qubit added to the system.

[2]Every nucleus has its own Larmor frequency $\omega_N = \gamma_N B$, where γ_N is the gyromagnetic ratio that is characteristic of the nuclear species and B is the external magnetic field.

Solid-state NMR could theoretically offer solutions to the problem of scalability. Since the qubits are fixed, this technique uses dipole-dipole couplings for qubits interactions, leading to faster quantum gates. Anyway, as its liquid counterpart, solid-state NMR suffers from some inefficiencies, mainly in state initialization and measurement capabilities, thus preventing scalability to large architectures.

Trapped atoms. Some species of isolated atoms (both ions and neutral atoms) have specific energy levels that provide very long decoherence times (in the order of seconds or even more). Individual ions can be confined using electric fields and manipulated using lasers and radio-frequency (rf) magnetic fields gradients [25]. Neutral atoms, on the other hand, cannot be confined using electric field, but arrays of them can be formed using a pattern of laser beams creating an optical lattice, which allows a precise control over many parameters of the system.

Interactions between atomic qubits can be achieved in different ways, e.g. through contact interactions or using large electric dipole moments in Rydberg atoms. Anyway, a common problem in both implementations is preserving the high efficiency achieved in small systems while scaling to larger ones, because laser-cooling becomes inefficient, noise and decoherence are greater and collective phenomena arise that can degrade quantum gates performances.

Quantum dots and dopants in solid. The use of quantum dots (QDs) and single dopants in solid could overcome the difficult issues of cooling and trapping single atoms. Quantum dots are systems that exhibit quantum mechanical properties due to their tiny dimensions (in the order of tens of nanometers): in a way, they can be considered giant artificial atoms whose properties can be suitably engineered. The main types of QDs are *electrostatically* defined QDs and *self-assembled* QDs: the former must operate at temperatures lower than 1 K and are controlled electrically while the latter can operate at ≈ 4 K and are controlled optically. QDs could also consist in a single impurity in a crystalline lattice, e.g. a single phosphorus atom in silicon [26].

Electrostatically-defined and impurity-based QDs have short-range interactions that prevent the construction of reliable fault-tolerant gates. Self-

assembled QDs, on the other hand, can offer better performances mainly due to their large size that leads to a better coupling to photons. A major hurdle is their random nature: they assemble in random locations and their properties vary from dot to dot.

Another solution is using optically active dopants, e.g. a negatively charged nitrogen-vacancy centre in a diamond. Systems like this exhibit coherence times longer than QDs even at room temperature.

The main problem in all these implementations is the scalability to larger architectures.

Superconductors. In superconductors at very low temperature, electrons bind in Cooper pairs whose quantum parameters can be finely controlled through inductances and capacitances allowing the construction of qubits. Qubits interactions can be achieved through capacitive or inductive coupling, though this may present problems for large architectures. Another way to let qubits interact is via microwave photons. This way seems more promising, as showed by the implementation of some quantum algorithms by DiCarlo *et al.* [27]. Anyway, even if major progresses have been made to achieve coherence time up to few microseconds, decoherence and noise are the main challenges in this kind of systems.

Other techniques. Other possible systems under investigation are single, ballistic electrons in low-temperature semiconductor nanostructures, rare-earth ions in crystalline hosts and electron-based qubits in fullerenes [28], nanotubes [29] and graphene [30].

It is evident that there is a large number of possible implementations for the quantum hardware and each has its points of strengths and its drawbacks: some may be more suitable for the processing of qubits while others can be used as communication channels. Usually, within a single technology, there is a trade-off between the ability to manipulate the qubits and the efficiency of the transmission of data: often, in order to enable efficient data processing, it is necessary to encode qubits into highly interactive physical systems that perform poorly as transmission channels; vice-versa, low interacting qubits that can be used for data transmissions are usually difficult to manipulate adequately.

1.4 Transmission of qubits

As mentioned above, transmission of qubits is a capital problem in designing a quantum computer. This thesis will address a specific architecture for transmitting qubits, thus it is worth reviewing in some details this topic in the following.

Generally, the transmission of information can be accomplished in two different ways: by sending a low interacting carrier via a channel that does not perturb its state (this will be called the "flying qubit" scheme), or by sending the state through the different nodes that constitute the channel (this will be called the "state over channel" scheme). The former case is similar to a single messenger that travels to bring its message, while the latter is similar to the game of the "Chinese whispers". The two methods differ in one basic way: while the former requires the encoding of the information in a moving qubit that can travel hopefully without interacting with the environment, in the latter the physical blocks are static and they must interact together to allow the state transfer.

One possible theoretical implementation of the "state over channel" scheme consists in a series of SWAP gates: using dynamically controlled systems, it should be possible to bring qubits closer to make them interact and share the state, like in a relay race. Since this technique is prone to control errors, attention was moved to other alternatives.

One of them is to realize the processors with static qubits (e.g. trapped ions or quantum dots) and to communicate using photons as "flying qubits", thanks to their low interaction with the environment. Lots of improvement have been made since Cirac *et al.* [31] proposed a scheme to transmit qubits between two atoms in a cavity using photons (for example [31–34]). Another possible implementation is the physical movements of the ions and the atoms that carry the qubits. Anyway, both these schemes are quite hard to implement, since the former requires performing two information processing realizations, which is not a trivial task, while the latter requires a high degree of precision to move the qubits around without interfering with them and causing decoherence.

Thus, it is interesting to study if there is a way to send a quantum state over a channel that does not require external interactions to propagate the signal or any particular interfacing of different technologies. In 2003,

Bose [35] discovered that a uniform, unmodulated 1D spin chain can indeed propagate qubits with a high degree of fidelity. Since his seminal work, the properties of spin-graphs[3] have been massively investigated [36, 37].

In the following chapter we will present the properties of spin chains and how quantum state transfer can be implemented in this kind of systems.

[3] A spin graph is a collection of interacting 1/2-spin particles arranged in a precise and fixed network.

Chapter 2

Quantum State Transfer in spin chains

2.1 Introduction

There are several reasons to study quantum state transfer (QST) on spin chains:

- They are static channels and this means that they require the minimum possible external interaction in comparison to the encoding of qubits into flying photons or moving ions and atoms.
- They can be engineered within the same technology of quantum processors and quantum memories, leading to a simpler architecture of the entire system.
- In quantum computers, it is conceivable that there will be some kind of quantum register to temporarily store data coming from processors or from external inputs. Spin chains can act as *buffers*, or spacers, between quantum registers or between quantum registers and the macroscopic world of the programmer/end-user.
- It might be possible that, within a single processor, qubits have to be far from each other to reduce mutual interactions. Anyway, to process data, it is necessary to bring together the qubits in the correct logic gate: the implementation of a network of spin chains would be one of the easiest ways to accomplish this task.

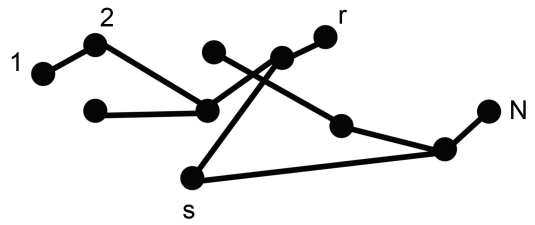

Figure 2.1: Representation of a generic spin graph. The label s and r indicate the site available to the sender and the receiver, respectively. From [35].

- The implementation of spin chains is becoming more and more feasible and the possibility to simulate spin chains with photonic lattices - three-dimensional arrays of evanescently coupled waveguides - allows to study experimentally the properties of these systems [38–43].

In this chapter we will discuss two of the most studied 1D spin chains (section 2.2), the main problems that afflict them (section 2.4), some possible applications that depart from the mere use of spin chains as channels of communication (section 2.5) and some real implementations (section 2.6). At last, we will analyse how these systems - in particular the mirror symmetric spin chain - can be simulated with the use of photonic lattices (section 2.7).

2.2 1D spin chain.

Let us consider a generic system composed of N coupled 1/2-spin particles, labelled $1, 2, \ldots, N$. An example of spin graph is showed in figure 2.1.

We will distinguish the two spin states of each particle as the *ground state*

$$|\downarrow\rangle = |0\rangle = \begin{pmatrix} 0 \\ 1 \end{pmatrix}$$

and the *excited state*

$$|\uparrow\rangle = |1\rangle = \begin{pmatrix} 1 \\ 0 \end{pmatrix}$$

.

The generic Hamiltonian that describes the evolution of the system is

$$\mathcal{H} = \sum_{<i,j>} J_{i,j}\vec{\sigma}_i \cdot \vec{\sigma}_j + \sum_i B_i \sigma_i^z \tag{2.1}$$

$$= \sum_{<i,j>} J_{i,j}(\sigma_i^x\sigma_j^x + \sigma_i^y\sigma_j^y + \sigma_i^z\sigma_j^z) + \sum_i B_i\sigma_i^z \tag{2.2}$$

where $< i, j >$ represent a pair of spins, $J_{i,j} < 0$ is the coupling strength between spin i and spin j, $B_i > 0$ is the *static* magnetic field on spin i and $\vec{\sigma}_i = (\sigma_i^x, \sigma_i^y, \sigma_i^z)$, where $\sigma_i^{x,y,z}$ are the Pauli matrices[1].

The Hamiltonian (2.2) describes an arbitrary ferromagnet with isotropic Heisenberg interactions: this is called the XXX model, since the coupling coefficients are the same in every direction of the space ($J_x = J_y = J_z$). It is possible to conceive other different models, like the XYZ model, where $J_{i,j}^x \neq J_{i,j}^y \neq J_{i,j}^z$, and the XY model, where $J_{i,j}^x \neq J_{i,j}^y$ and no interaction is considered along the z-axis.

As mentioned in section 1.2, the state of a system of N qubits is represented by a complex vector in a 2^N-dimensional space. Anyway, it is possible to simplify the mathematical complexity considering that the Hamiltonian (2.2) commutes with the operator $\sum_i \sigma_i^z$, i.e.

$$[\mathcal{H}, \sum_i \sigma_i^z] = 0$$

as it is shown in appendix B.

This means that the number of excited spins is preserved during the evolution of the system. For this reason, the 2^N-dimensional space can be separated in a series of subspaces, characterized by the number of the qubits in the excited state $|1\rangle$: the subspace where all states have only one excited spin is called the *single excitation subspace*; if there are two excited spins it is the *double excitation subspace*, and so on.

As we will explain in section 2.3, most of the properties of spin chains can be derived considering only the single excitation subspace. Thus, we can restrict our study to the subspace where all the spins are down ($|0\rangle$) except for one spin: this is a major simplification since it allows to study the evolution of the system considering that only one spin is up at a fixed time. This allows to consider a simplified model, the *XX model*, where the

[1] A summary of the relevant properties of Pauli matrices can be found in appendix A.

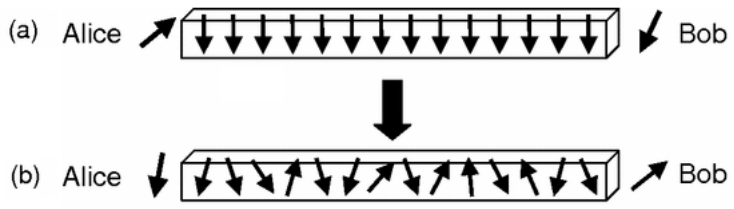

Figure 2.2: Example of one-dimensional spin chain. (a) Alice injects her qubit in the state $|\psi_{in}\rangle$ in the initialized system. (b) After the evolution of the sistem for a suitable time, Bob extracts Alice's original state. From [35]

spin-spin interactions along the z-axis are neglected:

$$\mathcal{H}_{XX} = \sum_{<i,j>} J_{i,j}(\sigma_i^x \sigma_j^x + \sigma_i^y \sigma_j^y) + \sum_i B_i \sigma_i^z \tag{2.3}$$

since $\sigma_i^z \sigma_j^z |0\rangle^{\otimes n-1} |1\rangle |0\rangle^{\otimes N-n} = 0$, $\forall \{i, j, n\}$.

To simplify notation, in the following we will label in boldface the state of the whole chain in the single excitation subspace, while in plain text the state of a single qubit. Therefore, we will identify with $|\mathbf{j}\rangle = |000\ldots010\ldots00\rangle$ the state of the chain where all the spins are in state $|0\rangle$ and spin j is in state $|1\rangle$. With this convention, $|\mathbf{0}\rangle$ represents the ground state $|0\rangle^{\otimes N} = |000\ldots000\rangle$, while $|\mathbf{1}\rangle = |1\rangle |0\rangle^{\otimes N-1} = |100\ldots000\rangle$ and $|\mathbf{N}\rangle = |0\rangle^{\otimes N-1} |1\rangle = |00\ldots001\rangle$.

1D spin chains described by the XX model are the easiest systems to study due to their low dimensionality. Moreover, it can be shown that they are the systems with the best performance, as we will explain in the following sections. A graphical representation of a 1D spin chain is given in figure 2.2.

In the following, we will analyse the simplest protocol to transmit information over a spin chain, following Ref. [35]. We will make the following hypotheses, unless specified otherwise:

1. We consider only nearest-neighbour couplings.

2. The spin controlled by the sender is labelled with $n = 1$, while the receiver's spin is $n = N$.

3. We consider the system initialized to its ground state $|\mathbf{0}\rangle = |0\rangle^{\otimes N}$, whose energy is set to $E_0 = 0$ for simplicity.

4. We consider *perfect injection*, i.e. it is possible to introduce losslessly an unknown state $|\psi\rangle = \alpha|0\rangle + \beta|1\rangle$ into the sender spin.

Under these assumptions, the sum over the generic pair of spin can be simplified ($\sum_{<i,j>} \to \sum_{n=1}^{N-1}$) and the XX Hamiltonian can be written as

$$\mathcal{H}_{XX} = \sum_{n=1}^{N-1} J_n(\sigma_n^x \sigma_{n+1}^x + \sigma_n^y \sigma_{n+1}^y) + \sum_i B_i \sigma_i^z \tag{2.4}$$

or equivalently

$$\mathcal{H}_{XX} = \sum_{n=1}^{N-1} J_n(\sigma_n^+ \sigma_{n+1}^- + \sigma_n^+ \sigma_{n+1}^-) + \sum_i B_i \sigma_i^z \tag{2.5}$$

Let us consider now the system in its ground state $|\mathbf{0}\rangle$. Suppose that Alice, the sender, wants to transmit to Bob, the receiver, the state

$$|\psi_{in}\rangle = \cos\frac{\theta}{2}|0\rangle + e^{i\phi}\sin\frac{\theta}{2}|1\rangle \tag{2.6}$$

She injects the state $|\psi_{in}\rangle$ into the spin $n = 1$ of the chain at $t = 0$ (figure 2.2a). while at time $t = t_0$ Bob extracts the state $|\psi_{out}\rangle$ of the spin N (figure 2.2b). Ideally, he would like to retrieve a state as close as possible to Alice's, i.e.

$$\left|\psi_{out}^{desired}\right\rangle = e^{i\theta}|\psi_{in}\rangle \tag{2.7}$$

The similarity between Alice's and Bob's state is measured by a parameter F called *transfer fidelity*. For two pure states $|\phi\rangle$ and $|\psi\rangle$, the transfer fidelity can be defined[2] as the "overlap" of the normalized vectors representing the two states, i.e. $F = |\langle\phi|\psi\rangle|$.

The aim of studying the properties of spin chains is to understand how the transfer fidelity $F = \langle\psi_{out}|\psi_{in}\rangle$ and the transfer time t_0 depend on the form of the Hamiltonian. If the transfer fidelity is unitary, i.e. if $|\psi_{out}\rangle = e^{i\theta}|\psi_{in}\rangle$, then *perfect state transfer* (PST) is achieved. Note that the perfect state transfer is necessary to share the pair of maximally entangled particles[3]

[2]More generally, for two states defined by the density matrices ρ_1 and ρ_2, the transfer fidelity is defined as $F(\rho_1, \rho_2) = Tr\left[\sqrt{\sqrt{\rho_1}\rho_2\sqrt{\rho_1}}\right]$ [44]. A *pure state* is a state that can be described by a vector in a Hilbert space, as opposed to a *mixed state*, that are ensemble of pure states and can be described only through a density matrix.

[3]The definition of a maximally entangled state is quite complex. A colloquial definition is that it is impossible to retrieve the information stored in a maximally entangled system performing a local measurement, i.e. only on one of the particles of the system.

necessary to perform several QIP protocols, like quantum teleportation and superdense coding [13].

The mathematical derivation of the evolution of a spin chain in the single excitation subspace is clearer if we consider the whole chain as a single system. At time $t = 0$, the state of the whole chain at $t = 0$ (when Alice injects her qubit) can be written as[4]

$$|\Psi_{in}\rangle = |\Psi(0)\rangle = \cos\frac{\theta}{2}|\mathbf{0}\rangle + e^{i\phi}\sin\frac{\theta}{2}|\mathbf{1}\rangle \tag{2.8}$$

while at time $t = t_0$ (when Bob extracts the qubit from the chain) the system should be in a state as close as possible to

$$|\Psi_{out}\rangle = \cos\frac{\theta}{2}|\mathbf{0}\rangle + e^{i\phi}\sin\frac{\theta}{2}|\mathbf{N}\rangle \tag{2.9}$$

With this notation, the transfer fidelity at a generic instant t can be defined as $F(t)=\langle\Psi_{out}|e^{-i\mathcal{H}t}|\Psi_{in}\rangle$ [35].

In the following, we will analyse the two main spin chain models: the *uniform* spin chain, which was the first studied [35], and the so-called J_x spin chain [45, 46].

2.2.1 Uniform spin chain

In the absence of external magnetic fields, the evolution of a spin chain with uniform couplings is described by the Hamiltonian

$$\mathcal{H} = J\sum_{n=1}^{N-1}(\sigma_n^x\sigma_{n+1}^x + \sigma_n^y\sigma_{n+1}^y) \tag{2.10}$$

This Hamiltonian is very simple since it does not require any particular engineering of the couplings between the spins; despite its performance is not optimal, it has two interesting points worth to be highlighted.

First of all, it is possible to perform PST on chains with $N = 2$ or $N = 3$ qubits. This is a fundamental point, since it demonstrates that it is possible to achieve PST in a time independent Hamiltonian. Moreover, this system

[4] We recall that the state $|\mathbf{j}\rangle$ is the state where all spins are in state $|0\rangle$ except spin j, that is in state $|1\rangle$.

can outperform classical transfer fidelity (equal to 2/3, [47]) for spin chains with N as high as 80.

These findings suggest that it is possible to obtain PST over a higher number of sites with the proper engineering of the couplings.

2.2.2 J_x spin chain

It can be demonstrated [36] that, in order to achieve PST from $n = 1$ to $n = N$, the Hamiltonian (2.3) must be mirror symmetric, i.e.

$$J_n^2 = J_{N-n}^2$$
$$B_n = B_{N+1-n}$$

Many different models can be built starting from these simple mathematical constraints. Since it is closely related to the subject of this thesis, we will describe in some details the characteristics of one of these models, the mirror Hamiltonian with linear spectrum, also known as J_x Hamiltonian.

In the absence of external magnetic field, the matrical representation of the generic XX Hamiltonian (2.5) is

$$\mathcal{H} = \begin{bmatrix} 0 & J_1 & 0 & \cdots & 0 \\ J_1 & 0 & J_2 & \cdots & 0 \\ 0 & J_2 & 0 & \cdots & 0 \\ \vdots & \vdots & \vdots & \ddots & J_{N-1} \\ 0 & 0 & 0 & J_{N-1} & 0 \end{bmatrix} \tag{2.11}$$

The form of this matrix closely resembles the form of the J_x operator of a spin-(N-1)/2 particle. Thus, we can draw a correspondence between our N-qubit spin chain and a fictitious spin-(N-1)/2 particle. This helps analysing the problem. Indeed, from quantum mechanics[5] it is known that the angular momentum operator J_x for a spin-(N-1)/2 particle has a representation identical to (2.11), where J_n follows the relation

$$J_n = \frac{1}{2}\sqrt{n(N-n)} \tag{2.12}$$

and its spectrum is linearly spaced. Thus, if we choose a generic $\mathcal{H} = \lambda J_x$,

[5]For example, see [48, chapt. 4] or [49, par. 36].

our system will inherit all the properties of the operator J_x acting on a spin-(N-1)/2 particle. This is fundamental, since the evolution of the system is described by the unitary operator

$$\hat{U}(t) = e^{-i\lambda J_x t} \tag{2.13}$$

and it can be shown that such operator represents a rotation $\mathcal{R}_x(\phi)$ of the spin-(N-1)/2 particle

$$\hat{R}_x(\phi)\psi(x) = e^{-i\phi J_x}\psi(x) \tag{2.14}$$

In this picture, it is easy to figure out that PST between two antipodal points[6] of the chain is equivalent to a rotation $\phi = \pi$ of the "angular moment" of our fictitious particle. Thus, since $\phi = \lambda t$, this means that the rotation of the fictitious particle is achieved in a time $t = \frac{\pi}{\lambda}$. Hence, for the analogy with the spin chain, we can deduce[7] that PST is achieved in $t = \frac{\pi}{\lambda}$.

Summarizing, for a spin chain described by the J_x Hamiltonian

$$\begin{cases} \mathcal{H} = -\sum_{n=1}^{N-1} J_n(\sigma_n^x\sigma_{n+1}^x + \sigma_n^y\sigma_{n+1}^y) \\ J_n = \frac{\lambda}{2}\sqrt{n(N-n)} \end{cases} \tag{2.15}$$

perfect state transfer between *any two antipodal nodes* is achieved in $t_{PST} = \frac{\pi}{\lambda}$. Note that this transfer time is *independent* from the number N of the qubits of the system. An example of perfect state transfer for a system with $N = 25$ qubits is shown in figure 2.3.

This result has a huge technological impact since it demonstrates that it is possible to realize a PST between any two antipodal nodes of a spin chain simply with a proper engineering of the coupling coefficients of the system - no external control is theoretically required during the transmission of the qubits.

It is interesting to see whether this system is affected by timing errors. In fact, until now it has been assumed that Bob can extract the qubit *exactly* at $t = t_{PST}$, but this will not usually be the case. As shown in [36], an analysis on the generic expression of the $1 \leftrightarrow N$ fidelity $F(t) = \langle \mathbf{N}|e^{-i\mathcal{H}t}|\mathbf{1}\rangle$

[6] I.e., between the spin i and $N + 1 - i$

[7] For a more formal derivation, see [36]

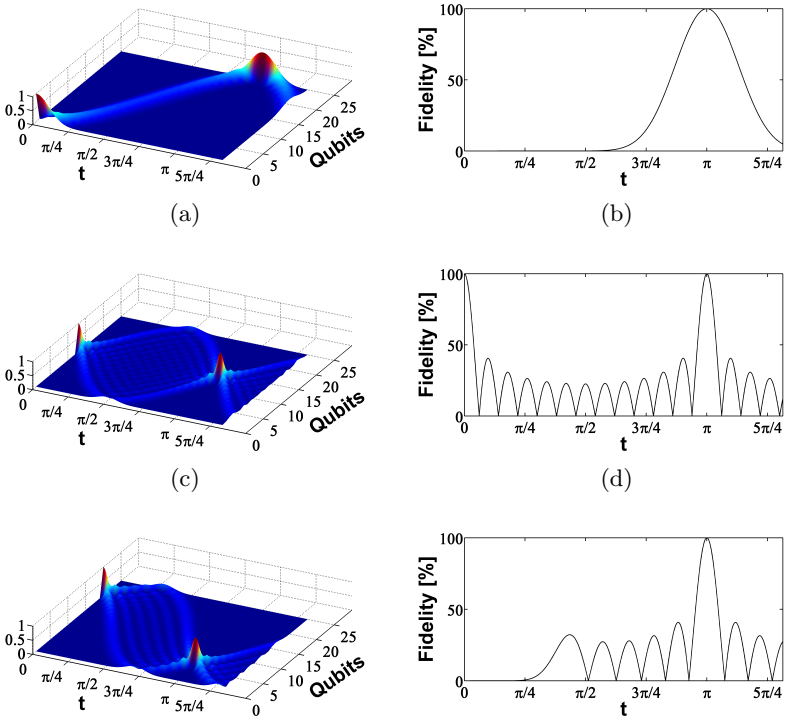

Figure 2.3: Performance of a J_x spin chain with $N = 25$ qubits. $J_n = \frac{\lambda}{2}\sqrt{n(N-n)}$, where $\lambda = 5.9 \times 10^{-2}$.
(a),(c),(e) Propagation of the state injected into qubits $n = 1$, 13, 20 and (b),(d),(f) correspondent fidelities.

shows that, for $t \approx t_{PST}$, the fidelity transfer is $F(t) \approx 1 + \frac{d^2F(t)}{dt^2}\Big|_{t=t_{PST}} = 1-\langle \mathbf{1}|\mathcal{H}^2|\mathbf{1}\rangle$. To reduce timing errors, the term $\langle \mathbf{1}|\mathcal{H}^2|\mathbf{1}\rangle$ must be minimized, and this corresponds to minimizing $J_1^2+B_1^2$. For the J_x Hamiltonian, $B_1 = 0$ and J_1 is only $1/\sqrt{N}$ of the maximum coupling strength: as a result, this system is very robust to timing errors, with respect to most of the other models of spin chains; in addition to this, as can be observed by inspecting the concavity of the local maxima in subfigures 2.3 (b),(d) and (f), it is evident that the transfer between the edges of the J_x spin chain is more robust than the transfer between any other pair of spins.

As we have seen, the success of the J_x Hamiltonian lies in its linearly spaced eigenvalues spectrum. Thus, any type of perturbation that alters this regularity will degrade the transfer fidelity of the system. One of the most relevant sources of perturbation is the presence of long-range interactions: non-nearest neighbour couplings produces interferences that disturb the transfer process and degrade the transfer fidelity, as shown in figure 2.4.

2.3 Higher excitations subspaces.

The advantage of considering the nearest-neighbour XX model (2.3) is evident when we analyse the spin chain in presence of multiple excitations. In this case, it is useful to perform the Jordan-Wigner transformation (see (B.1)), that maps the excitations of the spins into *non-interacting fermions*. The Hamiltonian (2.3) then becomes

$$\mathcal{H}_{JW} = \sum_{n=1}^{N-1} J_n(a_n^\dagger a_{n+1} + a_{n+1}^\dagger a_n) + 2\sum_{n=1}^{N} B_n a_n^\dagger a_n \tag{2.16}$$

where we have introduced $a_j^\dagger$ and a_j, namely the *creation* and *destruction* operators acting on the fermion j.

The main consequence of this transformation is that the individual non-interacting fermions behave like in the single excitation subspace, and only their relative phase has to be taken into account. In this way, it is possible to remove the requirements on the initialization of the system in the state $|\mathbf{0}\rangle$ [36], which is not a trivial task.

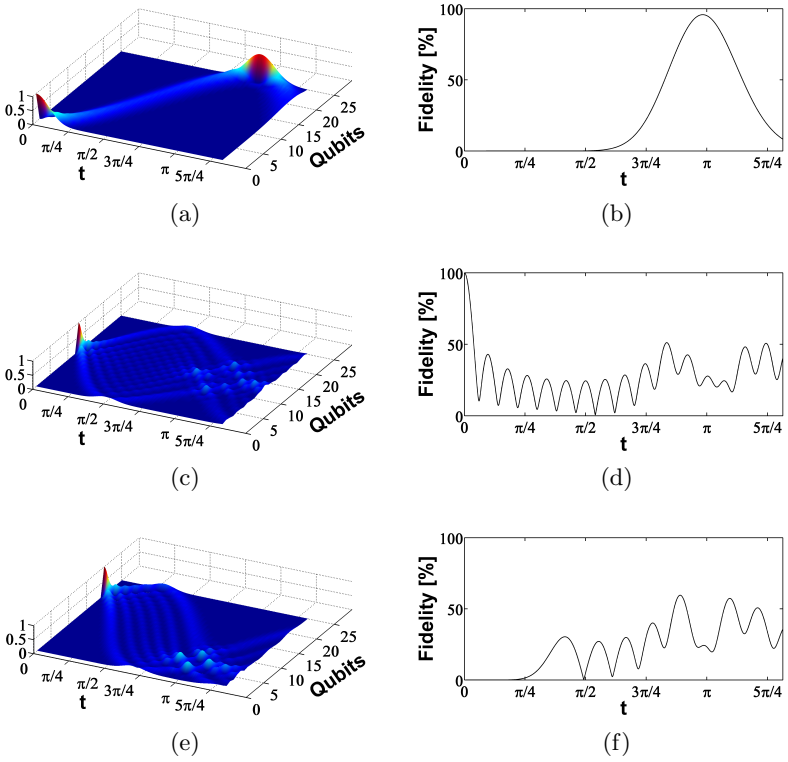

Figure 2.4: Degradation of the performances of the J_x Hamiltonian with $N = 25$ qubits in presence of next-nearest neighbour interaction $J_{n,n+2}$. J_n have the same values as in figure 2.3, while the coupling coefficients of next-nearest neighbours is around one order of magnitude weaker.
(a)-(e) Propagation of the state injected into qubits $n = 1$, 13, 20 and (b)-(f) correspondent fidelities.

2.4 Analysis of the main problematics

2.4.1 Noise

There are two kinds of defects that can degrade the performance of a system: *static* and *dynamic* defects.

The effects of static defects on the performance of spin chains have been widely studied [50, 51]. Depending on their magnitude, these defects, usually related to manufacturing errors, can result in the Anderson localization - i.e. the absence of diffusion waves in presence of large defects - or into small errors in the arrival fidelities for small defects.

On the other hand, dynamic defects, due to the interaction with the environment, are more difficult to take into account, because there can be different types of interaction and different models to describe them. For example, two causes of dynamical noise can be local bit flips or decoherence effects. Local bit flip is the unwanted excitation of a spin caused by interaction with the environment or with its neighbours, and its random nature is very difficult to model. Decoherence effects, on the other hand, can be modelled in different ways, e.g. with the interaction of the whole spin chain with the external environment or as local dephasing (see for example Refs. [36, 52]). All the models that try to consider decoherence are quite complex, but they generally show that state transfer in mirror symmetric systems is more robust than in uniform chains.

An interesting feature of quantum noise is that it has been shown that it can actually *enhance* the transfer ability in general spin graphs where coherent perfect state transfer is impossible [53].

2.4.2 Higher dimensionalities

It is quite straightforward to extend the 1D model to higher spatial dimensions. Consider a planar spin graph constituted by $N \times M$ qubits indexed by their position (x, y): introducing two different nearest neighbour couplings (J_n in the x direction and K_n in the y direction), the Hamiltonian of the

system in absence of a magnetic field B is easily derived as

$$\mathcal{H}_{2D} = \frac{1}{2}\sum_{i=1}^{N-1}\sum_{j=1}^{M} J_n \left[\sigma^x_{(i,j)}\sigma^x_{(i+1,j)} + \sigma^y_{(i,j)}\sigma^y_{(i+1,j)}\right] + \frac{1}{2}\sum_{i=1}^{N}\sum_{j=1}^{M-1} K_n \left[\sigma^x_{(i,j)}\sigma^x_{(i,j+1)} + \sigma^y_{(i,j)}\sigma^y_{(i,j+1)}\right] \quad (2.17)$$

Such a system performs state transfer between opposite points $(i, j) \to (N + 1 - i, M + 1 - j)$.

Anyway, the Jordan-Wigner transformation does not apply to 2D and 3D spin graphs, so it is not possible to guarantee PST in higher excitation subspaces. Moreover, in these systems the problem of non-nearest neighbour couplings is much more relevant and the description of the system is more difficult.

2.5 Different applications of spin chains

By exploiting the properties of spin chains it is possible not only to achieve perfect state transfer but also other goals.

For example, with proper engineering, a spin network can perform logical operations during the transmission, it can act as a sequential quantum storage (basically, a FIFO buffer), it can generate entangled state or it can amplify the signal of a single qubit [36].

Moreover, other types of protocols have been envisioned [37]. For example, the use of a spin chain to share entangled states between two registers in a quantum computer allows the transfer of information via teleportation of qubits. Such protocol is more permissive on the performance of the spin chain since PST of the entangled state is not necessary, thanks to the possibility of performing *entanglement distillation*, an operation that permits the retrieval of maximally entangled states from degraded entangled qubits.

2.6 Implementation of spin chains

Nowadays, the only technological platform that has successfully implemented spin chains is the nuclear magnetic resonance (NMR) [37]. The main reasons of the success of NMR in quantum information processing are the following:

- the qubits, defined through nuclear spins, are easily distinguishable by their Larmor frequencies and chemical shift;
- the Hamiltonians are well characterized;
- this systems have long coherence times;
- there is a good tradition of control techniques.

As mentioned in section 1.3, there are two different types of implementations, namely, liquid-state NMR and solid-state NMR.

In liquid-state NMR, qubits are encoded in magnetically distinct spins of a given molecule immersed in a solvent. The main advantages of this implementation are the easy identification of qubits, the good knowledge of the Hamiltonians and the high level of control. This has allowed the realization of some proof-of-principle experiments that demonstrated the feasibility of quantum state transfer through spin chains. This technique, however, is not scalable for two reasons: for every qubit added to the system, there is an exponential decrease in signal, and there is a limited number of frequency-resolved spins. Coherent transport in liquid-state NMR has been observed [54] even before QST was proposed. More recently, QST has been simulated through a simple XX Hamiltonian implemented on a 3-spin chain system composed of the spins in a trichloroethylene (TCE) molecule [55, 56]. The reported transport fidelity was low due to the experimental timescale ($t \approx 210 - 280\ ms$, much longer than the dephasing time of the molecule), to the presence of single-qubit control pulse errors and to the presence of strong couplings whose effects were neglected in the implementation. With different control techniques, QST has been accomplished on the spins of ^{13}C atoms along the backbone of leucine molecules [57]. Such method used requires a good knowledge of the parameters of the system as well as the different frequencies and chemical shifts of the atoms, but it is a more general method than the one used in [55, 56], since it does not requires the single-qubit control.

In solid-state NMR, qubits are encoded in the spins of the fixed atoms of a lattice. It has been found that one dimensional systems are more likely to exhibit QST since in higher dimensions spin diffusion tends to be indistinguishable from incoherent dynamics. Nowadays, the most important nuclear spin systems to study quasi-1D spin dynamics are apatite crys-

tals, mainly fluorapatite (FAp, $Ca_{10}(PO_4)_6F_2$) and hydroxyapatite (HAp, $Ca_{10}(PO_4)_6(OH)_2$): when the external field is oriented along their c-axis, the ^{19}F (or ^{1}H) systems can be considered as a collection of identical 1D spins, thus providing a natural 1D spin chain. These crystals can be grown synthetically, thus permitting a precise control on the paramagnetic impurities, leading to longer coherence times. Unfortunately, the disposition of the atoms inside the crystal gives little space to the engineering of the Hamiltonian: in one dimension, it is possible to retrieve the $\mathcal{H}_{XX}$ only through a series of rotations along different crystallographic axes (more details can be found in [37]). Even without a deeper treatment, it is evident that solid-state NMR is not as flexible as liquid-state NMR and, even though QST in larger solid-state systems with faster rate has been proven, collective control of spins and ensemble measurement have prevented the characterization of the transport fidelity, so far.

To conclude, even if liquid-state and solid-state NMR techniques are not scalable to proper quantum computers, they can help to design new potentially scalable systems.

2.7 Simulation of spin chains in photonic lattices

The technical difficulties in the implementation of spin chains have forced to devise other ways to mimic their behaviour. Here, we will review the simulation of 1D spin chains in the first excitation subspace using photonic lattices [41–43], which has been possible thanks to the technique of femtosecond waveguide writing[8].

2.7.1 Fundamentals of coupled mode theory.

Photonic lattices are three-dimensional arrays of evanescently coupled waveguides. They are usually described according to the coupled mode theory.

Basically, coupled mode theory is a perturbative theory: we will consider "distant" waveguides, so that the profile of the electric field inside each waveguide can be considered unperturbed by the fields of the neighbouring waveguides. In this model, power is transferred between adjacent waveguides thanks to the overlap of the guided modes' evanescent tails.

[8] In chapter 3 we will describe this technique and its advantages over standard lithography.

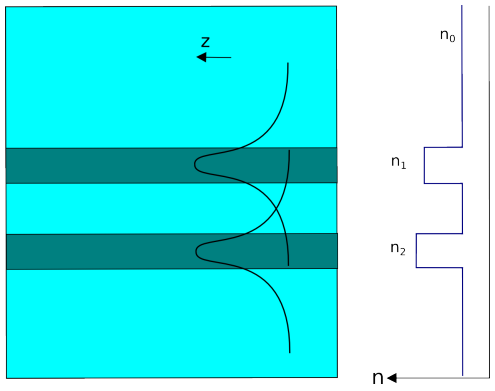

Figure 2.5: Scheme of two weakly coupled waveguides. Top view on the left, refraction index profile on the right.

For simplicity, let us consider the simple case of two adjacent waveguides with their optical axis oriented along the z direction, as in figure 2.5. The refractive index of this structure can be written as

$$n(x,y) = \begin{cases} n_1 & \text{inside waveguide 1} \\ n_2 & \text{inside waveguide 2} \\ n_0 & \text{elsewhere} \end{cases} \tag{2.18}$$

Being $\nabla_\perp^2$ the transverse laplacian $\nabla_\perp^2 = \frac{\partial^2}{\partial x^2} + \frac{\partial^2}{\partial y^2}$, $k_0 = \frac{2\pi}{\lambda_0}$ the wavevector of the radiation, we can solve the Helmholtz equation for the electric field of the system:

$$\nabla_\perp^2 \psi + \frac{\partial^2}{\partial z^2}\psi + k_0^2 \cdot n(x,y)^2 \psi = 0 \tag{2.19}$$

adopting the following Ansatz

$$\psi(x,y,z,t) = A_1(z)\psi_1(x,y)e^{-i\beta_1 z} + A_2(z)\psi_2(x,y)e^{-i\beta_2 z} \tag{2.20}$$

In this expression, $A_{1,2}(z)$ is the envelope of the electric field expressed as a function of the propagation coordinate, $\psi_{1,2}(x,y)$ is the spatial profile in the transversal plane of the waveguide and $e^{-i\beta_{1,2}z}$ is the term describing the propagation of the waves with generic propagation constants β_1 and β_2.

Inserting the Ansatz in the Helmholtz equation and supposing that the envelope $A_i(z)$ varies slowly with respect to the wavelength of the radiation[9],

[9] This is the *slowly varying envelope approximation* (SVEA). Mathematically, this is expressed by the condition $|\partial_z^2 A(z)| \ll |\beta \cdot \partial_z A(z)|$.

it can be shown that the evolution of $A_1(z)$ and $A_2(z)$ is described by the following system of coupled ordinary differential equations

$$\begin{cases} i\frac{\mathrm{d}}{\mathrm{dz}}A_1 = \kappa_{1,1}A_1 + \kappa_{1,2}A_2 e^{i\Delta\beta} \\ i\frac{\mathrm{d}}{\mathrm{dz}}A_2 = \kappa_{2,1}A_1 e^{-i\Delta\beta} + \kappa_{2,2}A_2 \end{cases} \tag{2.21}$$

where

$$\Delta\beta = \beta_1 - \beta_2 \tag{2.22}$$

is the *propagation constant mismatch*, and

$$\kappa_{i,j} = \frac{k_0^2}{2\beta_i} \frac{\int\int \psi_j \Delta n_j^2 \psi_i^* dxdy}{\int\int |\psi_i|^2 dxdy} \tag{2.23}$$

is the *coupling coefficient* between waveguides i and j. $\Delta n_i(x,y)^2$ is defined as $\Delta n_i(x,y)^2 = n(x,y)^2 - n_i(x,y)^2$, being $n_i(x,y)$ a piecewise-defined function equals to n_i inside waveguide i and equals to n_0 elsewhere, so that $\Delta n_i(x,y) \neq 0$ only in waveguide $j \neq i$. $\Delta n_i(x,y)^2$ can be seen as the effective refractive index of one waveguide as seen from the mode confined in the other.

If $i \neq j$, the coupling coefficient describes the spatial overlap of the evanescent wave i with the field in waveguide j - and vice versa; the terms $\kappa_{i,i}$ represent only small perturbations of the propagation constant β_i.

It can be shown [58] that the system (2.21) can be written as

$$\begin{cases} i\frac{\mathrm{d}}{\mathrm{dz}}A_1 = \Delta\beta_1 A_1 + \kappa_{1,2}A_2 \\ i\frac{\mathrm{d}}{\mathrm{dz}}A_2 = \kappa_{2,1}A_1 + \Delta\beta_2 A_2 \end{cases} \tag{2.24}$$

In the general case of an array of N coupled straight waveguides, the last system can be written in a compact form as

$$i\frac{\mathrm{d}}{\mathrm{dz}}\underline{A}(z) = \underline{\underline{M}} \cdot \underline{A}(z) \tag{2.25}$$

where $\underline{A}(z) = [A_1(z), A_2(z), \ldots A_N(z)]^T$ is the vector of the amplitudes of

the fields in the different waveguides and

$$\underline{\underline{M}} = \begin{bmatrix} \Delta\beta_1 & \kappa_{1,2} & 0 & \cdots & 0 \\ \kappa_{1,2} & \Delta\beta_2 & \kappa_{2,3} & \cdots & 0 \\ 0 & \kappa_{2,3} & \Delta\beta_3 & \cdots & 0 \\ \vdots & \vdots & \vdots & \ddots & \kappa_{N-1,N} \\ 0 & 0 & 0 & \kappa_{N-1,N} & \Delta\beta_N \end{bmatrix} \tag{2.26}$$

is the matrix that accounts for all the couplings $\kappa_{i,j}$ and the detunings $\Delta\beta_i$.

If $\underline{\underline{M}}$ is space independent[10], the solution of this system, with initial state $\underline{A}(0) = \underline{A_0}$ is

$$\underline{A}(z) = e^{-i\underline{\underline{M}}z} \cdot \underline{A_0} \tag{2.27}$$

The equations in this section have been derived for coherent laser beams propagating in a photonic lattice. However, following the same derivation, it is possible to demonstrate that the equations (2.25)-(2.27) hold true also for single photons, where the amplitudes A_i are mapped onto the creation operators $a_i^\dagger$.

As a last remark, it is important to underline that the calculation of the coupling coefficients is usually rather complex in the case of waveguides written with femtosecond micromachining, since the distribution of refractive index of the structure usually is irregular. For this reason, the coupling coefficients $\kappa_{i,j}$ are commonly related to the distance $d_{i,j}$ between waveguides i and j and are experimentally characterized by means of the formula [59]

$$\kappa_{i,j} = ae^{-bd_{i,j}} \tag{2.28}$$

2.7.2 Quantum optical analogy of the spin chain

In appendix B, it is demonstrated that the evolution of a spin chain in the *single excitation subspace* is described by a system of coupled equations analogous to (2.25), since the matrical representation (B.2) of the Jordan-Wigner Hamiltonian $\mathcal{H}_{JW}$ has the same structure of the matrix that describes the

[10] The system is invariant under longitudinal translations.

interaction of the waveguides in a photonic lattice (2.26).

$$\mathcal{H}_{JW} = \begin{bmatrix} 2B_1 & J_{1,2} & 0 & \cdots & 0 \\ J_{1,2} & 2B_2 & J_{2,3} & \cdots & 0 \\ 0 & J_{2,3} & 2B_3 & \cdots & 0 \\ \vdots & \vdots & \vdots & \ddots & J_{N-1,N} \\ 0 & 0 & 0 & J_{N-1,N} & 2B_N \end{bmatrix} \leftrightarrow$$

$$\underline{\underline{M}} = \begin{bmatrix} \Delta\beta_1 & \kappa_{1,2} & 0 & \cdots & 0 \\ \kappa_{1,2} & \Delta\beta_2 & \kappa_{2,3} & \cdots & 0 \\ 0 & \kappa_{2,3} & \Delta\beta_3 & \cdots & 0 \\ \vdots & \vdots & \vdots & \ddots & \kappa_{N-1,N} \\ 0 & 0 & 0 & \kappa_{N-1,N} & \Delta\beta_N \end{bmatrix}$$

In this analogy, the coupling coefficients $\kappa_{n,n+1}$ have the role of the coupling strengths J_n, while the detunings $\Delta\beta_i$ between the waveguides have the same role of the external magnetic fields B_i.

Thus, since in the single excitation subspace the behaviour of the two system is the same, we can map directly the temporal evolution of the spin chain into the spatial evolution of light into a waveguide array.

Differences arise when one considers higher excitation subspaces, since the non-interacting fermions derived from the Jordan-Wigner transformation are still linked by a relative phase that cannot be described by the bosonic nature of light. This is irrelevant in experiments performed in the single excitation subspace, while in the other subspaces there are differences in the exchange statistics, as will be highlighted in the following section.

There are two different ways to study spin chains in photonic lattice, namely injecting one (or more) single photons - or *Fock states* - or injecting coherent laser beam. Using Fock states it is possible to perform different types of quantum experiments, e.g studying the statistics of two-photon interference or analysing how entanglement is preserved in these structures. On the other hand, classical light permits to analyse the evolution of the probability distribution of single photons by inspecting the evolution of the intensity pattern

2.7.3 Differences in statistics

As mentioned before, the fundamental difference between photons in a photonic lattice and a spin chain is related to the different statistics of fermions and bosons. In [42], this difference is analysed inspecting the behaviour of the *correlation matrix*

$$\Gamma_{m,n}(z_0) = \left\langle a_m^\dagger a_n^\dagger a_n a_m \right\rangle \tag{2.29}$$

which measures the probability for a pair of particles of arriving in $z = z_0$ at the sites n and m.

With the input state $|\psi_{in}\rangle = |1\rangle |0\rangle^{\otimes N-2} |1\rangle = a_1^\dagger a_N^\dagger |\mathbf{0}\rangle$, the main difference is observed when $z_0 = \pi/2$, since the two particles collide and interference occur. In this case, the correlation matrices for bosons and fermions are, respectively,

$$\Gamma_{m,n}^{bosons} = \begin{cases} 0 & n-m : \text{odd} \\ \frac{1}{2^{2N-4}} \binom{N-1}{m-1} \binom{N-1}{n-1} & n-m : \text{even} \end{cases} \tag{2.30}$$

and

$$\Gamma_{m,n}^{fermions} = \begin{cases} \frac{1}{2^{2N-4}} \binom{N-1}{m-1} \binom{N-1}{n-1} & n-m : \text{odd} \\ 0 & n-m : \text{even} \end{cases} \tag{2.31}$$

For a system with $N = 11$ qubits, the two correlation matrices are shown in figure 2.6, and it is evident that the two matrices have different symmetries.

For this reason, the photonic lattices can easily mimic the dynamic of spin chains in the single excitation subspace, while it is not straightforward to simulate the fermionic dynamic of spin chains in higher excitation subspaces. One possible way to simulate fermionic statistics with photons could be to use singlet entangled state [60, 61].

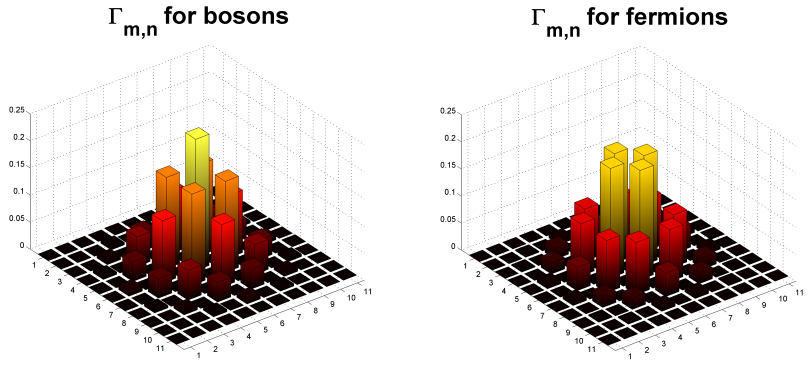

(a) (b)

Figure 2.6: Correlation matrices for (a) bosons and (b) fermions, for $N = 11$ qubits.

2.7.4 Physical implementations

Two implementations of photonic lattices that simulate the J_x Hamiltonian have been reported in [41, 43].

Bellec *et al.* [41] fabricated a photonic lattice in fused silica to perform experiments with coherent laser beams at $\lambda = 633$ nm, in order to study the evolution of the light intensities in the array.

The 10 cm-long device consisted in $N = 9$ waveguides with parabolic interwaveguide distances around $d \sim 22$ μm, whose reported maximum fidelity $1 \to 9$ is 65%. The main problems have been related to the writing process: the low-frequency regime of the laser may have created some local differences in the waveguides, resulting in an asymmetric lattice, and imperfection in the translational stage might have created slight deviations from the optimal couplings. A comparison between the theorical behaviour and the measured one is displayed in figure 2.7.

A similar device has been implemented in [43]: it consisted in a 94 mm-long array with $N = 19$ waveguides inscribed in fused silica, with interwaveguide distances ranging from 14.3 μm to 18.12 μm.

It was reported that the outermost waveguides had different coupling properties due to stress fields in the host material produced during the fabrication. In fact, as we will see in the following chapter, waveguides written by femtosecond micromachining are created inducing a local variation of refractive index exploiting the interaction of the laser beam with the sub-

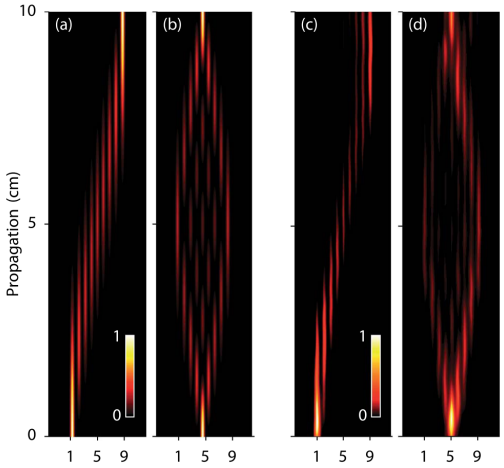

Figure 2.7: Numerical simulation (a)-(b) and experimental fluorescence image (c)-(d) of the device fabricated by Bellec *et al.* [41].

strate. Thus, when writing several waveguides close to each other, it is possible that each waveguide resents from the fabrication of its neighbours. For this reason, since the outermost waveguides have only one neighbour - while the inner ones have two adjacent waveguides - this could create non uniformities that degrade the efficiency of the transfer.

For this reason, two *dummy* waveguides have been inscribed at the edges of the array: their propagation constants β is much different from the ones of the other waveguides ($\Delta\beta = 8.7$ cm^{-1}), so that power transfer from and to them is inhibited. In this way, the array for PST is much more uniform, since each active waveguide has two neighbours.

The reported fidelities are higher than in [41], around 82% for the transfer $1 \leftrightarrow 19$ and 72% for $2 \leftrightarrow 18$. In addition to the analysis of the intensity distribution of coherent light propagating from inputs 1,2,18 and 19, they performed also experiments to measure the correlation matrix 2.29 at $z = 47$ mm, where two-photon intereference is expected to occur. In particular, they mimicked quantum interference using two mutually coherent laser beams ($\lambda = 800$ nm) with random relative phases injected in inputs 1 and 19 and managend to extract the correlation matrix $\Gamma^{bosonic}_{m,n}$ from the expression $\Gamma^{measured}_{m,n} = \Gamma^{bosonic}_{m,n} + I_{m,1}I_{n,1} + I_{n,N}I_{m,N}$, where $\Gamma^{measured}_{m,n}$ is the measured correlation matrix and $I_{m,1}$ is the output intensity from waveguide m when the injection is in 1. The comparison of the theoretical correlation matrix

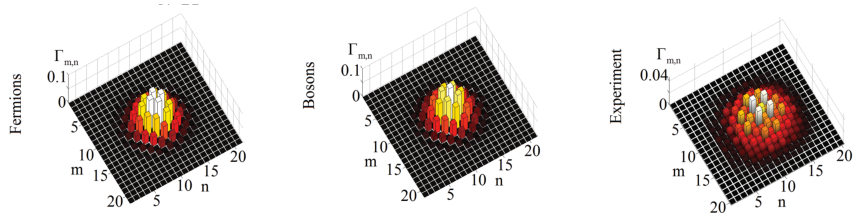

(a) (b) (c)

Figure 2.8: Calculated correlation matrices for (a) fermions and (b) bosons, for $N = 20$ qubits. (c) Experimentally obtained correlation matrix. Observing the disposition and symmetry of the peaks, it can be seen that the experimental correlation is more similar to the bosonic one. Images from [43].

with the experimentally measured is shown in figure 2.8.

Chapter 3

Femtosecond waveguide writing

3.1 Overview

The ability of femtosecond laser pulses to induce permanent modifications in dielectric substrates was demonstrated for the first time in 1996 [62]. Since then, this technology has emerged as one of the most powerful techniques to write micro- and nanometric features into glasses and crystals. This technique has some advantages over its competitors (primarily, photolitography):

- the realization of the devices requires a simpler and less expensive equipment, usually consisting of a laser source, an optical system for the steering and the focusing of the beam and a translation stage;
- it allows rapid prototyping due to its extreme flexibility: the pattern of a device can be changed easily via software control, while in photolitography it is necessary to produce an entire new mask;
- it is intrinsically a 3D technique, while photolitography is a planar technology.

Femtosecond waveguide writing exploits the nonlinear effect of multiphoton or tunnelling ionization to induce local modifications of the structure of transparent substrates. Due to the nonlinearity of the process, the alteration is possible only if the energy deposited from the laser is above a

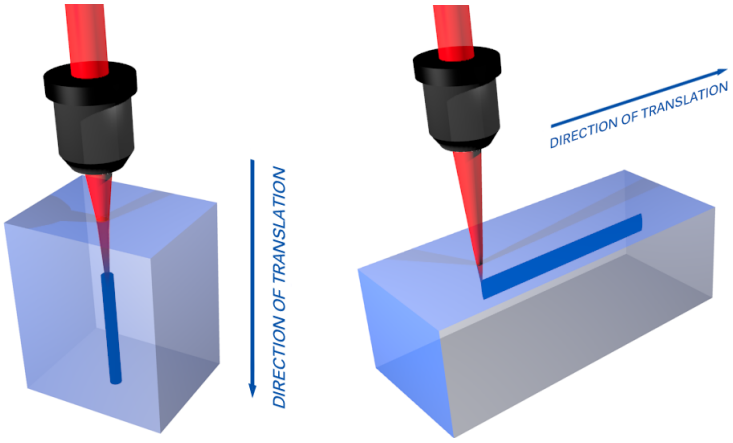

Figure 3.1: (a) Longitudinal and (b) transversal writing schemes. The blue arrows show the direction of translation of the substrate with respect to the laser beam.

precise threshold, and this condition is met only in the focal volume of the beam. Thus, the laser beam acts just like a pen, writing in three dimensions only where its tip passes.

There are two possible writing geometries (figure 3.1):

- *longitudinal geometry*, where the translation of the substrate is parallel to the laser beam. The section of the resulting waveguide has the same symmetry of the transversal section of the beam spot size - usually circular; in this case, however, the maximum length of the waveguides is limited by the focusing capabilities of the system, making this geometry little suitable for writing three-dimensional structures.

- *transversal geometry*, where the translation of the substrate is orthogonal to the laser beam. The section of the resulting waveguide is affected by the longitudinal section of the beam spot size - usually elliptical; this geometry allows to fully exploit the three-dimensional writing capability.

3.2 Laser-substrate interaction

3.2.1 Physical mechanisms

Introduction

Consider the interaction between a laser beam at frequency ν and a dielectric substrate transparent at that frequency, i.e its energy gap E_g is greater than the energy of the photons $h\nu$. In these conditions, light absorption is prevented.

At sufficiently high intensities, though, more than one photon interact simultaneously with the material, leading to nonlinear absorption phenomena. Absorption ionizes the substrate generating *plasma*; when the density of free electrons is high enough, the frequency of the plasma becomes equal to the frequency of the laser, and the plasma becomes locally absorbing. The energy absorbed by the plasma is then partially released in the substrate, that undergoes structural modifications due to heat and pressure.

Nonlinear absorption processes

The nonlinear absorption phenomena that lead to the generation of plasma are *multiphoton ionization*, *tunnelling ionization* and *avalanche ionization*.

Multiphoton ionization takes place when m photons are absorbed simultaneously by the substrate, leading to the ionization of one or more electrons, and this can happen only if $mh\nu > E_g$ (figure 3.2, on the left).

Tunnelling ionization occurs when the high electric field of the laser lowers the Coulomb barrier, enabling the tunnelling of electrons from valence to conduction band (figure 3.2, on the right).

Avalanche ionization is due to the acceleration of one or more free electrons (called *seed electrons*) caused by the electric field of the laser: if these electrons acquire sufficient kinetic energy, they can ionize other electrons that will act as new seeds[1]. This "ionization-acceleration-ionization" process causes the exponential growth of the free electron density and the subsequent generation of an absorbing plasma.

These processes are closely related to the temporal dynamic of the laser pulse. With long laser pulses ($\Delta\tau > 10$ ps), the peak intensity is usually too

[1]The critical parameter is the ratio between the average time of electron-electron scattering and the time needed by one electron to acquire enough energy to ionize others.

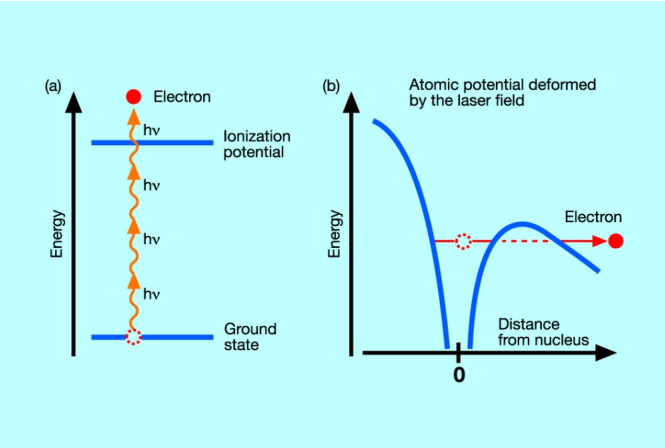

Figure 3.2: Schematic mechanisms of multiphoton ionization (a) and tunnelling ionization (b).

small to produce multiphoton or tunnelling ionization. Avalanche ionization and subsequent absorption can still be triggered by some free electrons in conduction band due to impurities and dislocations; anyway, this process is too much random to be reproducible. For laser pulses shorter than 10 ps, on the other hand, the peak intensity is usually higher than the threshold intensity of nonlinear processes, and multiphoton and tunnelling ionization will take place. The generated free electrons will constitute the seed of the subsequent avalanche ionization. Since the seed is created only where and when the laser pulse has enough intensity, this is a fully deterministic process.

Furthermore, femtosecond pulses evolve on a time scale shorter than the electron-phonon scattering time ($\tau_{elec-phonon} \sim 1$ ps): this means that the light pulse ends well before sites external to the focal volume are thermically excited. Heat diffusion is thus minimized, leading to a more precise writing process.

Mathematical models of the nonlinear phenomena

Typically, in femtosecond pulses, multiphoton ionization is dominant over tunnelling ionization. A parameter to distinguish these two regimes has been found to be [63, 64]

$$\gamma = \frac{\omega\sqrt{m_{reduced}\Delta}}{eE} \tag{3.1}$$

where ω is the laser frequency, $m_{reduced}$ is the reduced effective mass of the electron, Δ is the bandgap of the glass, e is the electric charge and E is the electric field of the laser beam. When $\gamma \gg 1$, multiphoton ionization dominates, while if $\gamma \ll 1$ tunnelling dominates.

Furthermore, if the pulse duration is lower than a certain threshold ($\tau_{threshold} = 150$ fs in fused silica) avalanche ionization is negligible, while if $\Delta\tau > \tau_{threshold}$ avalanche becomes more important than multiphoton ionization [64].

Thus, for glasses, considering only multiphoton and avalanche ionization it is possible to write a model for the free electron density n_e during the excitation of the laser beam [65]:

$$\frac{dn_e}{dt} = W(I, \hbar\omega, \Delta) + \eta I n_e \tag{3.2}$$

In this expression, the term $W(I, \hbar\omega, \Delta)$ describes for the multiphoton ionization: I is the intensity of the laser beam, $\hbar\omega$ is the energy of the photons in the beam and Δ is the glass bandgap. This term can be expressed using the Keldysh formula [66] as

$$W = \sigma(k) I^k \tag{3.3}$$

where k is the order of the multiphoton process, i.e. how many photons are interacting simultaneously, and $\sigma(k)$ is the cross-section of the process. It must be observed that the nonlinearity order k is wavelength dependent[2].

Considering the emission of a Ti:sapphire oscillator at 800 nm, $k = 6$ and $\sigma = 10^9$ $\text{ps}^{-1}\text{cm}^{-3}(\text{cm/TW})^k$ in fused silica, while $k = 3$ and $\sigma = 10^{18}$ $\text{ps}^{-1}\text{cm}^{-3}(\text{cm/TW})^k$ in borosilicate.

The term $\eta I n_e$ describes for avalanche ionization, being η the avalanche coefficient; in fused silica $\eta = 4$ cm^2/J, while in borosilicate $\eta = 1.2$ cm^2/J.

Induced structural modifications

The amount of energy transferred from the plasma to the substrate can lead to different structural modifications. If the amount of energy absorbed by the dielectric is too high, the substrate can exhibit dramatic damages, like

[2]Intuitively, the number of photons required to achieve a nonlinear process depends on their energy $E = h\nu = \frac{hc}{\lambda}$, where $k \cdot E > E_g$.

the forming of voidlike structures or fractures. For lower energies, it acquires a permanent change in the index of refraction, usually in the order of 10^{-3}.

The microscopic processes that lead to the refractive index modification are still not completely clear; however, in dielectrics three possible mechanisms that concur to the creation of a permanent change in the index of refraction have been proposed:

- *colour center formation* - the irradiation generates UV-absorbing color centers that, according to Kramer-Kroenig mechanism, modify the refractive index in the visible and near IR wavelengths;
- *thermal phenomena* - the energy deposited melts the glass locally and the subsequent rapid solidification induce density differences and therefore variations in the index of refraction;
- *direct photostructural change* - the femtosecond radiation induce rearrangements of the network of the chemical bonds inducing a density increase, leading to a higher refractive index.

3.2.2 Process parameters

As we have seen, in femtosecond waveguide writing there is a wide variety of phenomena involved. Thus, there are many different parameters that have to be taken into consideration.

Wavelength. The substrate has to be transparent to the incident radiation, otherwise linear absorption occurs, leading to the damaging of the material. For this reason, usually the incident radiation is in the IR region of the light spectrum. Anyway, for high bandgap materials the nonlinearity order of the absorption is very high, meaning that the process has tighter requirements in terms of peak power, focusing, deposited energy, etc. This could limits the reproducibility and can reduce the degrees of freedom available[3]. To avoid this, it is possible to use the second harmonic of the laser fundamental frequency ν: since the photons have double energy, the nonlinearity order is halved, relaxing the requirements of the process.

[3]For example, objectives with high numerical apertures are used to reduce the focal volume of the beam and increase the peak intensity. This limits the fabrication depth since objectives with high NA have small working distances.

Repetition rate f_{rep}. The repetition rate is another fundamental parameter: being the writing speed relatively low as compared to the spot size times f_{rep}, the laser pulses hit repeatedly the same region in the substrate. This can have different effects, depending whether the energy of the single pulse is dissipated or not by the substrate in the time between two subsequent pulses. Thus, as can bee seen in figure 3.3, two different regimes occur depending on the ratio between the relaxation time $\tau_{heat} \approx 1$ μs and the repetition period $T_{rep} = 1/f_{rep}$.

In the *low-frequency regime* (blue curve), for f_{rep} well below 1 MHz so that $\tau_{heat} f_{rep} \ll 1$, the heat diffusion process is faster than the heat build-up caused by the laser beam. This leads to the rapid melting and solidification of the irradiated region, but each pulse has the same influence on the substrate. The overall effect is that the modification is confined to the focal volume of the laser beam and the section of the waveguide is determined by the elliptical shape of the spot size. It is worth noting that it is possible to obtain a circular section of the focal spot size (and thus of the waveguide) using suitable beam shaping techniques [67, 68], even if it is not always necessary.

On the other hand, in the *high-frequency regime* (red curve), for f_{rep} well above 1 MHz so that $\tau_{heat} f_{rep} \gg 1$, the energy deposited by the laser beam cannot dissipate rapidly enough, so the temperature reached is much higher and the heat diffusion extends more isotropically beyond the focal region. The modified region is thus much more uniform, since it depends mostly on the heat diffusion process and not on the shape of the focal volume.

With the advent of ytterbium oscillator, it has become possible to work within a third regime, the *mid-frequency regime*, where 200 kHz $< f_{rep} <$ 2 MHz. In this regime, the pulses have enough energy to induce modification by heat diffusion, but this effect is confined much closer to the focal volume, allowing a greater control of the shape of the waveguide cross-section.

Writing speed. The writing speed is a parameter that, along with the repetition frequency and the focusing of the beam, directly influences the characteristics of the guided modes in the waveguide. It is usually related to the frequency regime of writing: in the low-frequency regime the writing speed is $v_{writing} \approx 10$ μm/s, in the mid-frequency regime $v_{writing} \approx$ 100 μm/s-1 mm/s and in the high-frequency regime $v_{writing} > 1$ mm/s [70].

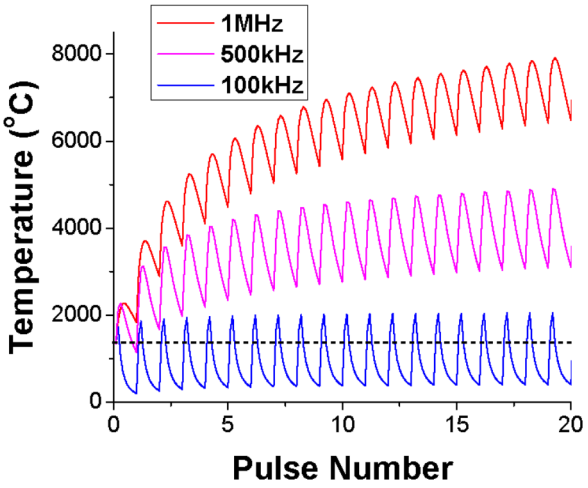

Figure 3.3: Finite difference simulation of the dependence of the local temperature with the repetition frequency at a distance $r = 2\ \mu$m from the centre of the laser beam. From [69].

Focusing. The focusing is important since it directly affects the area irradiated by the laser beam and thus the volume of dielectric that will undergo nonlinear interactions with the beam. This area is crucial since the peak intensity is inversely proportional to the irradiated area A:

$$I_{peak} = \frac{P_{peak}}{A} \approx \frac{2E_{pulse}}{\tau_{pulse}A} = \frac{2P_{avg}}{\tau_{pulse}f_{rep}A} \tag{3.4}$$

The area of the focal spot is related to the beam waist w_0 after the objective ($A = \pi w_0^2$). It can be related directly to the characteristics of the optical system:

$$A = \pi w_0^2 = \frac{4\lambda^2}{\pi}\left(\frac{D}{d}\right)^2 \frac{1}{NA^2} \tag{3.5}$$

where d is the diameter of the beam before the objective, λ is the wavelength of the laser light, NA is the numerical aperture[4] of the objective and D is its diameter.

The focusing system is very critical: since the beam focus has to be

[4]The *numerical aperture* of an optical system characterizes the range of angles over which the system can emit or accept light. It is normally defined as $NA = n\sin\theta$, where n is the index of refraction surrounding the optical element and θ is the half-angle of the maximum cone of light that can enter or exit the system.

inside the glass, the rays suffer from the refraction at the air-glass interface of the substrate. This can lead to excessive aberrations which could lower the effective writing intensity of the pulses and for this reason it must be compensated. This can be done mainly in two ways: by using a *compensated objective*, which has been designed to focus at a fixed distance inside a material with a precise index of refraction, or by using an *oil immersion objective*, that exploits the index matching properties of the synthetic oil posed between the sample and the objective to reduce the aberrations.

3.3 State of the art

3.3.1 Examples of passive and active devices

Femtosecond waveguide writing has been actively explored starting from the pioneering work of Hirao's group [62]. Since then, a wide variety of passive and active device has been realized. Here we will briefly review some of them to show the flexibility and the potential of this technology.

One of the earliest demonstrations of a three-dimensional device is the 1×3 splitter by Nolte *et al.* [71]. Realized in fused silica with a Ti:sapphire laser working at $f_{rep} = 1$ kHz, $v_{writing} = 125$ μm/s and $NA = 0.45$, the three output arms of the splitter are distant 100 μm from each other and exhibit an almost perfect splitting ratio, 32:33:35.

Another example of three-dimensional device is the three-waveguide symmetric diretional coupler, realized by Kowalevicz *et al.* [72]. The writing setup consisted in a Ti:sapphire oscillator providing 150 nJ pulses with a repetition rate of 5.85 MHz. The writing speed was optimized to 10 mm/s and the focusing system consisted in an immersion objective with $NA = 0.86$. The distance between the arms of the device varies from 50 μm in the input and output region to 5 μm in the coupling region.

Li *et al.* [73] has realized an integrated electrooptical modulator, consisting in a Mach-Zehnder interferometer (MZI) written in thermal poled fused silica. After the writing of the MZI, the substrate is heated above 200°C while applying a strong electric field: in this way, the material acquires a permanent non-zero electro-optic coefficient. Two gold electrodes have been deposited to modulate the spectral response of the MZI

Many other examples of passive and active device can be found in [70].

3.3.2 Discrete waveguide array

Femtosecond waveguide writing has been widely employed to study arrays of evanescently coupled waveguides, also known as *photonic lattices*. In fact, the three-dimensional and fast prototyping capabilities of this technology have allowed the investigation of arrays having a wide variety of geometries.

The peculiarity of photonic lattices is that the longitudinal direction of propagation is physically different from the transverse ones, since the former is continuous while these latter are discrete. This influences the way light propagates inside these structures and causes a variety of interesting phenomena that have been studied over the last decade.

For example, in [74, 75] arrays with square and hexagonal geometries have been written in fused silica using a Ti:sapphire oscillator and a focusing objective with NA=0.45. These structure have been implemented to study evanescent-field coupling theory in these types of structures and to demonstrate the phenomenon of discrete diffraction - i.e. the spreading of light into a discrete medium (figure 3.4). By modulating the spatial properties of the arrays it was possible to observe peculiar phenomena, like the suppression of coupling along different transversal directions, the refocusing of light beams and the different coupling properties of the same lattice at different wavelengths [76]. A similar work [77] focused on studying Snell's and Fresnel's laws: two adjacent arrays with different coupling coefficients have been employed to simulate the interface between two different material and the analysis of reflection and refraction has been performed inspecting fluorescent light scattered by the colour centers created during the writing process.

Photonic lattices have been used also to simulate quantum systems with classical coherent light. In fact, if the refractive index along the propagation direction varies little on a spatial scale larger than the wavelength λ, it can be demonstrated that the Helmholtz equation for the electric field can be reduced to a form analogous to the two-dimensional time dependent Schrödinger equation[5] of a particle of mass n_{eff} moving in a potential

[5]The Schrödinger equation for a particle of mass m in a potential $V(x, y, z)$ is

$$i\hbar\frac{\partial}{\partial t}\psi = -\frac{\hbar^2}{2m}\nabla^2_{x,y}\psi + V(x, y, z)\psi$$

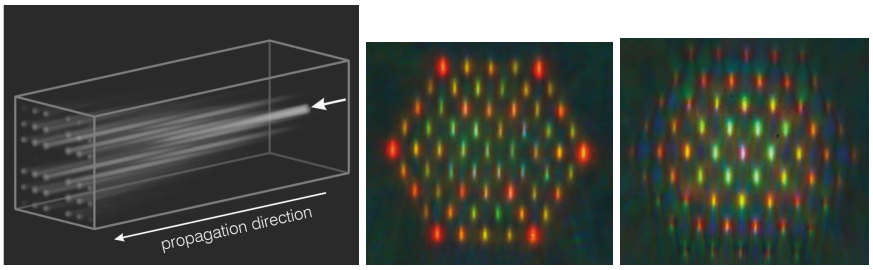

(a) (b) (c)

Figure 3.4: Examples of discrete diffraction. (a) Numerical simulation of light diffraction in a rectangular photon lattice, from [74]. (b) and (c): output color intensity pattern of a hexagonal array excited with white light (interwaveguide distances of 16 μm and 20 μm, respectively), from [75].

$V(x, y, z)$, where n_{eff} is the effective index of the guided mode and the potential V is given by the spatial profile of the index of refraction $n(x, y, z)$ [78]. The peculiar aspect is that photonic lattices map the *temporal* evolution of the 2D Schrödinger equation to the *spatial* propagation of light into the array ($\frac{\partial}{\partial t} \rightarrow \frac{\partial}{\partial z}$). This is interesting because it allows to study the temporal dynamics of fast quantum systems by simulating them with properly engineered photonic lattices. For example, the motion of electron wave packets in crystalline lattice under external fields - known as *Bloch oscillations* - has been investigated with such technique [79], where the external field was simulated varying linearly the refractive index of the waveguides in the array.

This analogy has been also used to simulate the quantum Rabi model and to study light-matter interaction in the deep strong coupling regime [80] and to study the band structure and transport properties of graphene irradiated by linearly and circularly polarized monochromatic light [81] (figure 3.5).

Discrete waveguide arrays have interesting applications also in the field of quantum optics. For example, quantum interference of photons has been studied through the theoretical analysis of photon number correlations in two-dimensional arrays and through simulations using classical light [82, 83]. Photonic lattices are also suitable for the simulation of quantum walk of single or correlated pairs of photons. For example, [84] reports the realization of two-photon quantum walk in a system of six equally spaced

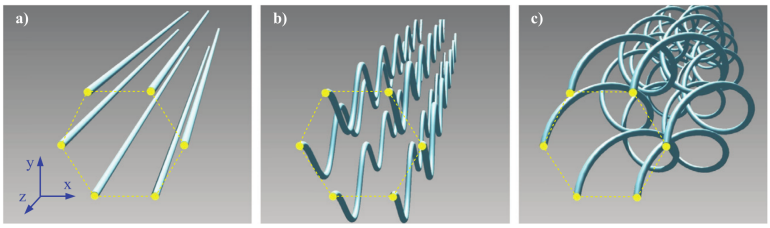

Figure 3.5: Different geometries adopted for the simulation of graphene properties when irradiated by (a) no light, (b) linearly polarized light and (c) circularly polarized light. From [81].

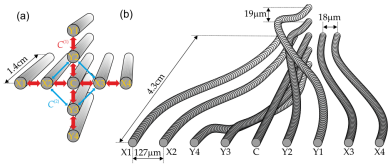

Figure 3.6: Swiss cross configuration of the waveguide array adopted in [85].

waveguides , while [85] has realized quantum walks of correlated photon pairs in 2D arrays arranged in a “swiss cross” configuration (figure 3.6).

Chapter 4

Experimental setup

4.1 Waveguide writing setup

4.1.1 Cavity-dumped Yb:KYW oscillator

All the devices presented in the second part of this thesis have been fabricated with a cavity-dumped Yb:KYW laser oscillator emitting pulses approximately 350-fs long with a maximum energy of 1 μJ at the wavelength of 1030 nm. Taking advantage of the cavity-dumping scheme, the repetition rate of the pulse train can be set in a wide interval between 10 kHz and 1.1 MHz; however, for the fabrication of the devices it was kept fixed at 1.0 MHz.

A scheme of the system is depicted in figure 4.1.

The active medium is constituted by a rod of $KY(WO_4)_2$ doped with ytterbium at 5% concentration. The crystal is pumped at $\lambda = 980$ nm by an InGaAs multiemitter diode bar.

The pulse train is achieved by a passive mode-locking. This regime is obtained using a SESAM (SEmiconductor Saturable Absorber Mirror). The cavity is 8.9 m long, reduced to a footprint of 90 cm$\times$50 cm using 21 mirrors. The natural repetition rate is thus

$$f_{rep} = \frac{c}{2L} \approx 17 \text{ MHz} \tag{4.1}$$

The extraction of the pulses (*cavity dumping*) is achieved through a *Pockels cell* and two *thin film polarizers* (TFPs). The crystal of the Pockels cell is BBO (barium β-borate), a negative uniaxial crystal with large birefringence,

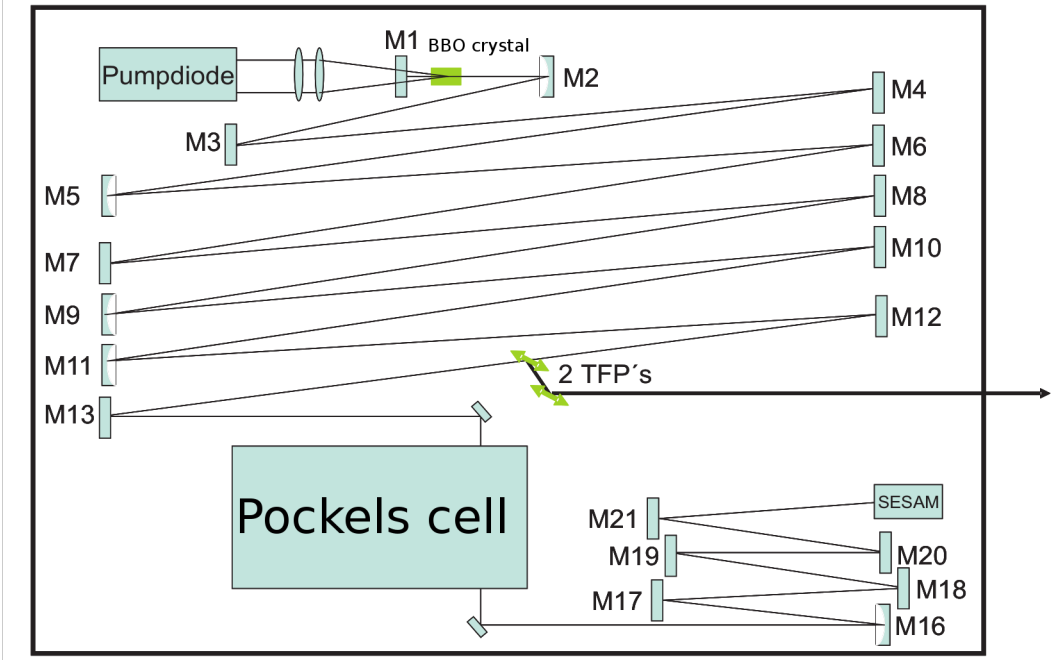

Figure 4.1: Scheme of the cavity-dumped Yb:KYO laser oscillator employed for the fabrication of the devices.

that can be modulated with an external electric field. An external driver modulates the voltage of the electrodes on the BBO synchronously with the mode-locking pulse train. Whenever one of the pulses passes through the BBO while the voltage is high, the induced birefringence causes a rotation of the polarization of the pulse. The higher the voltage on the electrodes, the more the polarization is rotated. The two TFPs send the portion of light with different polarization to the exit of the laser.

It is possible to tune the *amplitude* and the *frequency* of the electric signal sent to the Pockels cell to vary the amplitude and the repetition rate of the pulse train, respectively. The electric signal can have a maximum voltage of 2.2 kV and the repetition rate can be choosen among the integer submultiples of 17 MHz in the above mentioned range between 10 kHz and 1.1 MHz.

Depending on the pump power and on the dumping frequency and amplitude, different pseudo-solitonic regimes can be sustained, so it is possible to finely tune these two parameters to obtain pulses with duration between 250 fs and 400 fs. A complete treatment of the characteristics of this oscillator

can be found in Ref. [86]

4.1.2 Writing setup

The beam exiting the laser oscillator passes through an attenuator consisting of a half-wave plate and a polarizer: by rotating the polarizer, it is possible to set the correct writing power. Three mirrors bring the beam above the focusing objective, that focuses light into the sample collocated underneath. The writing objective can be changed according to the writing requirements.

The motion of the sample under the objective is enabled by *Aerotech FiberGLIDE 3D* three-axis motion stages. Its air bearing and non-contact brushless linear motors allow to maintain very low friction during the different movements. The position of the stages is constantly monitored through optical encoders within a feedback loop, ensuring a resolution of 1 nm and an overall positioning error below 100 nm.

The stages can be controlled and programmed by *G-Code language*, enabling the design of complex structures.

4.2 Device characterization

The basic characterization of a photonic device involves four different stages of analysis, that will be explained in the following. Except from the observation at the optical microscope, all the characterizations make use of laser light to study the device. There are several laser sources available (five laser diodes at 701 nm, 725 nm, 780 nm, 808 nm and 850 nm and one 633-nm HeNe), but in our work we used only the diode at 808 nm.

4.2.1 Optical microscope

The first step of characterization is the observation of the device using an optical microscope (*Nikon ME600*) equipped with a DIC (*Differential Interference Contrast*) module, which allows to identify small differences in the index of refraction by exploiting interference phenomena. It is possible to acquire pictures of the sample through a high resolution CCD camera (*PixeLINK B871*) mounted onto the microscope.

Observation from the top facet of the sample allows to recognize if writing errors have occurred - usually in the form of interrupted or flawed waveg-

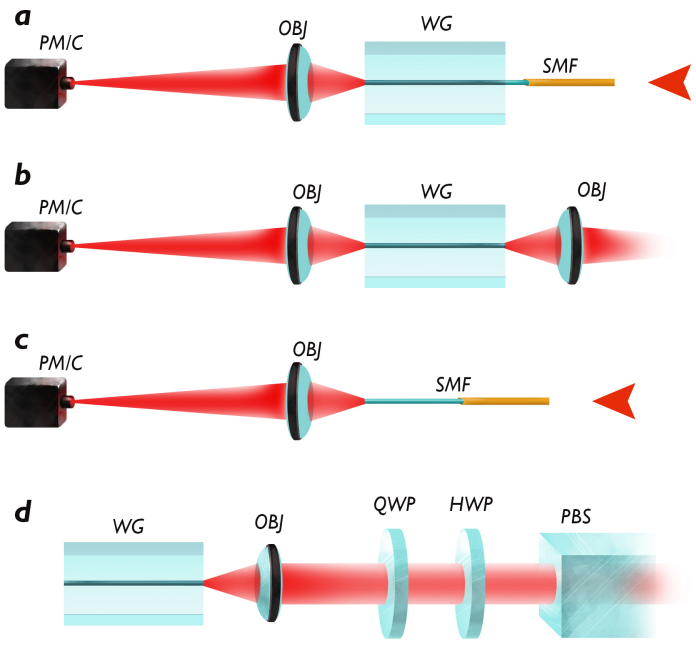

Figure 4.2: Schemes of the setup adopted for the characterization of the fabricated devices, as explained in the text. SMF: single mode fiber; WG: waveguide; OBJ: objective; PM/C: power meter or CCD camera; PBS: polarizing beam splitter; HWP: half-wave plate; QWP: quarter-wave plate.

uides. Observation from the lateral facet enables to verify the cross-section of the waveguides and to measure the interwaveguide distances in arrays.

4.2.2 Optical mode characterization

To study the optical properties of a waveguide - or, more generally, of a device - it is necessary to analyse qualitatively and quantitatively its output mode.

Laser light can be coupled into the waveguide using either a fiber or an objective (figure 4.2 (a)-(b)).

In the first case, one extremity of a single mode fiber (SMF) is brought near the input facet of the waveguide. In the other case, light is injected using an objective focusing on the input facet; the numerical aperture of the objective and the waveguide must be as close as possible (~ 0.10). In both cases, the aim is to overlap at best the injected optical mode with the waveguide one to reduce coupling losses.

Precise and stable alignment between the objective/fiber and the sample is required. For this reason, the objective/fiber is mounted on a three-axis micropositioner (*Melles Griot NanoMAX*), having a resolution of 50 nm. The sample is mounted on a four-axis manipulator (*Melles Griot AMT*) which allows two translation in the plane transversal to the optical axes and two tilt movements.

The output facet is imaged onto a CCD camera (*Edmund Optics EO-1312M*), using a high-NA objective ($NA \sim 0.5 - 0.6$) to collect as much light as possible and to obtain a good magnification ratio. It is possible to save the intensity profile of output mode of the waveguide to perform other quantitative analysis.

In the case of monomodal waveguides, the intensity profile $I(x, y)$ is sufficient to reconstruct the spatial distribution of the electric field of the light, according to the formula

$$|\vec{E}(x, y)| = C\sqrt{I(x, y)} \tag{4.2}$$

Theory assures that no sign inversion is present, thus the calculation of the modulus of $\vec{E}$ is sufficient. Moreover, the constant C is irrelevant, since we are interested in normalized quantities.

It is possible to measure the dimensions of the guided modes using as a reference the output mode of a single mode fiber, whose characteristics are known. Attention must be paid not to change the magnification ratio between the two measurements: after the acquisition of the output modes of the sample, it is important to maintain unaltered the distance between the second objective and the camera (figure 4.2 (c)).

4.2.3 Losses measurement

An important figure that summarizes the main characteristic of a waveguide is its *insertion losses* (IL). Insertion losses are defined as the total losses introduced by the waveguide, and thus can be simply calculated as

$$IL = 10 \log_{10} \left(\frac{P_{out}}{P_{in}} \right) \tag{4.3}$$

The input and the output power (P_{in} and P_{out}) are measured with a setup very similar to the one used for the analysis of the optical modes; the

only difference is that a powermeter (*Anritzu MA 9001A*) is used instead of the CCD camera.

In case of straight waveguides of length l, IL can be decomposed into the sum of three different terms: coupling losses (CL), Fresnel losses (FL) and propagation losses (PL):

$$IL = CL + FL + PL \cdot l \tag{4.4}$$

Coupling losses Coupling losses are due to mode mismatch between the optical fiber and the waveguide and depend on their overlap integral T_C according to:

$$CL = -10 \log_{10} T_C \tag{4.5}$$

The overlap integral is defined as

$$T_C = \frac{|\int\int E_f E_{wg} dxdy|^2}{\int\int |E_f|^2 dxdy \cdot \int\int |E_{wg}|^2 dxdy} \tag{4.6}$$

and it can be evaluated numerically from the field profiles of the fiber (E_f) and the waveguide (E_{wg}) acquired as explained above.

Fresnel losses Fresnel losses are due to the reflection of light at the glass-air interfaces. They are defined as

$$FL_{in/out} = -10 \log_{10} T_F^{in/out} \tag{4.7}$$

where $T_F^{in/out}$ is the Fresnel transmittance of the input/output facet. For a single glass-air interface, Fresnel transmittance T_F can be estimate as

$$T_F = 1 - \frac{(n_{glass} - n_{air})^2}{(n_{glass} + n_{air})^2} \tag{4.8}$$

being n_{glass} and n_{air} the refraction index of glass and air, respectively. For a single interface, being $n_{glass} \sim 1.45$ and $n_{air} \sim 1$, Fresnel reflectance is around 4% and $FL \sim 0.18$ dB. Hence, the total FL can be estimated to be around 0.36 dB.

Anyway, it is possible to reduce this figure by using an index-matching oil in the fiber-waveguide coupling. In this case, in the formula (4.8), n_{air} is replaced by n_{oil}, which is close to n_{glass}, and $T_F^{in} \to 1$, thus reducing the

Fresnel losses.

Propagation losses Propagation losses are the losses suffered per unit length of propagation. They are related to the intrinsic characteristic of the waveguide (roughness, non-uniformity, ...). Theory predicts no propagation losses for a waveguide with perfect translational symmetry along its optical axes.

Propagation losses are difficult to measure directly. For this reason, we have estimated them indirectly from equation (4.4), once measured insertion, coupling and Fresnel losses.

4.2.4 Characterization of polarization behaviour

The last type of characterization is the polarization behaviour, e.g. how light distributes if injected with different polarizations.

Light is injected via an objective, like in the optical mode characterization. Anyway, before entering the injection objective, it must be possible to select a precise light polarization. This is done using a polarizing beam splitter (PBS), a half-wave plate (HWP) and a quarter-wave plate (QWP) (figure 4.2 (d)): laser light passes through the PBS acquiring a vertical polarization; the subsequent HWP and QWP allow to arbitrarily rotate the polarization state of light that will be injected into the waveguide.

Part II

PST of polarization encoded qubits

Chapter 5

Experiment

5.1 Introduction

As we have seen in chapter 1, *entangled* qubits are one of the fundamental elements in several QIP protocols and, for this reason, it is interesting to investigate the preservation of entanglement when it is transferred through a spin chain.

In chapter 2 we have analysed one possible implementation of such spin chains, the J_x spin chain; moreover, it has been shown that it is possible to simulate the behaviour of these systems with properly engineered photonic lattices and we have also discussed some experiments designed to study PST in these structures. However, the preservation of entanglement in such devices has not been verified yet.

The work of this thesis is focused on the design and engineering of a polarization-insensitive photonic lattice to implement an optical analogous of the J_x spin chain exploiting femtosecond laser micromachining. This device (henceforth referred to as *PST waveguide array*) will be the main component in an experiment performed to test the preservation of entanglement of polarization-encoded photon qubits. During this thesis activity the device has been tested only with classical light, while the preservation of entanglement will be verified experimentally by a two-photon experiment performed by the Quantum Photonics Lab of the University of Sydney.

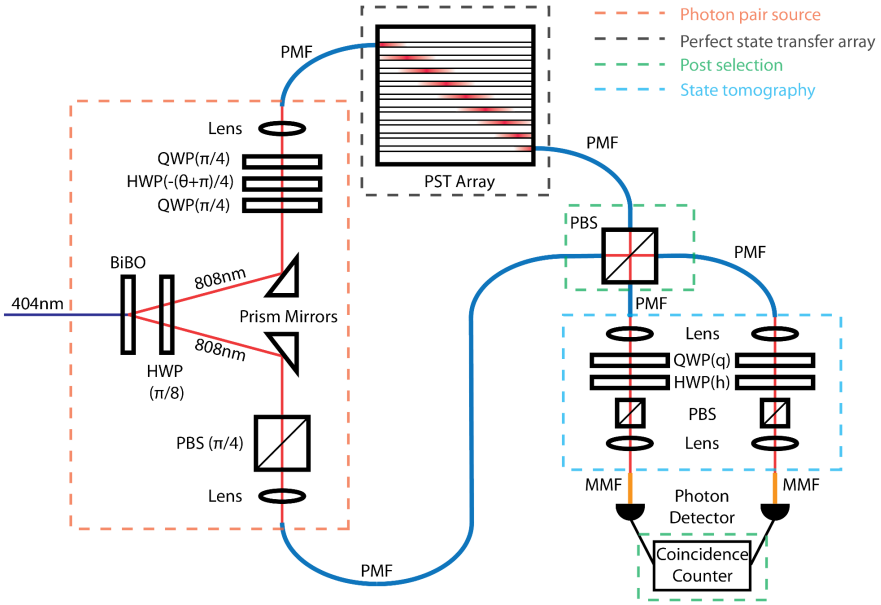

Figure 5.1: Proposed experimental setup to investigate the properties of entangled photons travelling through the PST waveguide array.

5.2 Design of the experiment

The experiment is conceptually simple: after the generation of a suitable pair of polarization-entangled photons, one of them is injected into the PST waveguide array, while the other enters a polarization maintaining fiber (PMF); the two photons are then collected and the final degree of entanglement is compared to the initial one by means of quantum tomography.

Generation of entangled photons and preparation of the state.

A pair of polarized-entangled photons is generated via type I spontaneous parametric down conversion (SPDC) by pumping a 404 nm laser beam into a BiBO crystal[1]. This process generates two identical, H-polarized photons $|H_0 H_1\rangle$ at 808 nm; these photons pass through an half-wave plate (HWP) rotated by $\frac{\pi}{8}$ that projects each input state $|H\rangle$ into $|-\rangle = \frac{|H\rangle - |V\rangle}{\sqrt{2}}$. Then, they take two different paths: one passes through a polarizing beam splitter (PBS) at $\frac{\pi}{4}$ to filter only the states $|\psi_0\rangle = \frac{|H_0\rangle - |V_0\rangle}{\sqrt{2}}$; the other passes through a system of one half-wave plate at an angle $-\frac{\theta+\pi}{4}$ stand-

[1]BiBO is the short name for bismuth (III) orthoborate, $BiBO_3$.

ing between two quarter-wave plates at $\frac{\pi}{4}$, in order to create the state $|\psi_1\rangle = \frac{|H_1\rangle - e^{-i\theta}|V_1\rangle}{\sqrt{2}}$. The purpose of this stage is to prepare the input state $|\psi_{in}\rangle = \frac{(|H_0\rangle - |V_0\rangle)(|H_1\rangle - e^{-i\theta}|V_1\rangle)}{2}$.

State transfer and post-selection

The qubit in the state $|\psi_1\rangle$ enters the PST waveguide array and is transferred from waveguide i to waveguide $N+1-i$, while the other propagates through the PMF. Assuming an ideal operation of the device, the evolution of the state is governed by the global unitary operator

$$U = U_{PST} \otimes I_{PMF} \tag{5.1}$$

where U_{PST} is the unitary matrix of the perfect state transfer, given by

$$U_{PST} = e^{-iH_{PST}t_{PST}} = \begin{bmatrix} 0 & 0 & 0 & \cdots & 1 \\ 0 & 0 & \cdots & 1 & 0 \\ 0 & \cdots & 1 & 0 & 0 \\ \vdots & & \vdots & \vdots & \vdots \\ 1 & \cdots & 0 & 0 & 0 \end{bmatrix}$$

and I_{PMF} is the identity operator relative to the propagation in the PMF.

In the post-selection stage, the photons are sent on the input faces of a PBS. In this way, only the projection on the state $|\phi(\theta)\rangle = \frac{|H_0H_1\rangle + e^{-i\theta}|V_0V_1\rangle}{\sqrt{2}}$ is extracted. By changing the angle θ in the preparation stage it is possible to generate Bell's states $|\phi^{\pm}\rangle = \frac{|H_0H_1\rangle \pm |V_0V_1\rangle}{\sqrt{2}}$ as well as other non-maximally entangled states.

Measurements

Under the assumption of ideal operation of the PST waveguide array, the state of the two-qubit system is unaffected by the propagation into the device. Thus, by reconstructing the state of the two-photon system before and after the PST waveguide array through two-qubit tomography [87], it is possible to determine if the entanglement has been preserved.

5.3 Device requirements

From the description of the experiment it is possible to retrieve the minimum requirements of the device to be developed.

First of all, the waveguides should be optimized to be single mode at 808 nm with low propagation losses.

Secondly, it has to be optimized to perform PST in a J_x photonic lattice. To emulate the behaviour of a real spin chain, photons will be injected in the first guide and collected from the last. So, the minimum requirement is achieving PST at least between site 1 and site N. However, it is interesting to investigate the properties of this lattice when entering from other sites (e.g., from the center of the array) since, theoretically, the J_x Hamiltonian should exhibit PST between any antipodal sites $(i, N+1-i)$. For this reason, it will be important not only to achieve PST for the transfer $1 \rightarrow N$, but also to optimize the transfer for some (or all) other injection guides.

Finally, the last requirement is to fabricate a polarization-insensitive device, since the entanglement is encoded in the polarization of photons.

Chapter 6

Design of a first prototype

6.1 Optimization of the waveguides

The first step of the fabrication process consists in the choice and optimization of the fabrication parameters.

For the substrate, we decided to use the borosilicate glass *Corning EAGLE 2000*. From previous experiment on waveguides written in borosilicate glasses with the setup described in section 4.1, we decided to write the sample using a 20x *Achroplan* objective (NA = 0.45) compensated at 170 μm, a writing speed of 40 mm/s and an average power of 300 mW.

The waveguides written with these parameters have been characterized as explained in section 4.2. As can be seen in figure 6.1, the waveguides sustain a single mode slightly elliptical (9.4 ± 0.9 μm $\times 15.1 \pm 0.6$ μm), accordingly to the shape of their transversal section.

The coupling and the propagation losses of the waveguides are 1.99 ± 0.20 dB and 0.80 ± 0.08 dB/cm, respectively, so that the resulting insertion losses for a 35 mm long waveguide are 5.14 ± 0.40 dB.

6.2 Characterization of the coupling coefficients

The critical parameters for the fabrication of a PST array are the coupling coefficients, since their proper engineering is the key to obtain perfect state transfer.

As mentioned in chapter 2.7.1, the coupling coefficients $\kappa_{i,j}$ follow the

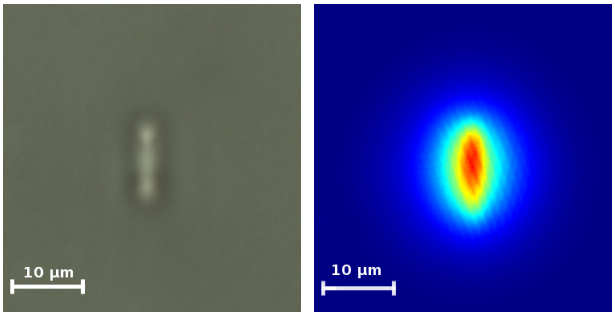

(a) (b)

Figure 6.1: (a) Transversal section of the waveguide characterized in section 6.1 and (b) its guided mode.

exponential law

$$\kappa_{i,j} = ae^{-bd_{i,j}}$$

as a function of the interwaveguide distance d_{ij}.

To determine the correct $d_{i,j}$ to achieve PST, a precise knowledge of the parameters a and b is necessary. To this end, we fabricated and analysed a set of five uniform 5-mm-long arrays with 21 waveguides; the interwaveguide distances were set in the range from 11 μm to 15 μm.

In previous experiments on similar arrays, it had been found that polarization insensitivity was achieved when the array was tilted by an angle around 60° with respect to the horizontal plane. For this reason, we decided to fabricate the structures tilted by this angle to check the polarization behaviour of the array.

Horizontally (H) and vertically (V) polarized light was injected in waveguides 1,11 and 21 and the output distribution has been acquired by a CCD camera and elaborated.

To retrieve the output intensity distribution of the array, one should integrate the output of each waveguide in both spatial dimensions and then normalize to 1 the contribution of all the wavegides. Anyway, assuming that the waveguides are identical, we can consider that the intensity profile of the guided mode is approximately the same for every waveguide, for example $I_n(x,y) = C_n e^{-\left[\frac{x^2}{x_d^2}+\frac{y^2}{y_d^2}\right]}$. For this reason, the spatial integral of the profile of each waveguide will be the same, except for the multiplicative constants C_n. Therefore, since we are interested only in the relative intensities of the

waveguides, it is sufficient to know the values of these constants C_n, and this can be done by inspecting the heights of the different peaks.

To process the acquired image of the output facet, a home-built Matlab script has been developed. The program performs a discrete integration over the axis orthogonal to the plane of the array: in this way, the 2D image acquired by the camera is reduced to a 1D profile, where the peaks of light corresponding to the output of the waveguides can be easily identified and selected. The normalized output distribution is then stored into a vector and saved for future analysis.

It has been possible to characterize the decay of κ by fitting the output intensity distributions of the arrays with a nearest-neighbour coupling model. The results of the fit of κ are reported in graphs 6.2. The R^2 of the fit for both polarizations is 0.92, indicating a good fit. The nearest-neighbour model offers a good fit for interwaveguide distances greater than 11 μm: for shorter spacings, the contribute of non-next-neighbour couplings begins to be relevant. For this reason, in figure 6.2 the values for $d = 11$ μm depart from the fitted curve.

To measure the differences in the output intensity distribution when entering with vertically and horizontally polarized light into the array we have used the parameter F_{HV}, called *HV fidelity*.

Fidelity between two pure states $|\phi\rangle$ and $|\psi\rangle$ has been defined in section 2.2 as the "overlap" of the normalized vectors representing the two states, i.e. $F = |\langle\phi|\psi\rangle|$; anyway, in our measurements it is difficult to retrieve the exact phase of light at the output of the single waveguides, since the CCD camera acquires intensity images. Therefore, we have used a different kind of fidelity: considering two intensity distributions with unitary norm[1] $\vec{I_1}=\{I_{1,m}\}_{m=1,\dots,N}$ and $\vec{I_2}=\{I_{2,n}\}_{n=1,\dots,N}$, the fidelity F is defined as

$$\begin{aligned} F &= \vec{I_1} \cdot \vec{I_2} \\ &= \sum_{i=1}^{N} I_{1,i} \cdot I_{2,i} \end{aligned} \tag{6.1}$$

Mathematically, the fidelity is the dot product of two unitary vectors in the space ${\mathcal{R}_+}^N$; therefore, it measures how much the two unit vectors are

[1] That is, $\|\vec{I}\|=\sqrt{\sum_i I_i}=1$.

"parallel" and it can assume values in the range $[0, 1]$, where 0 corresponds to orthogonal vectors and 1 to parallel vectors. From this property, it is possible to derive the sensitivity of this metric: since the dot product measures the cosine of the "angle" θ between the two states

$$\begin{aligned} F &= \vec{I_1} \cdot \vec{I_2} \\ &= |I_1| \cdot |I_2| \cos(\theta) \\ &= \cos(\theta) \end{aligned}$$

the fidelity is less sensitive to little variations when the states are very similar, i.e.

$$\frac{dF}{d\theta} = -\sin(\theta) \to 0, \qquad \theta \to 0 \tag{6.2}$$

From the definition given above, the HV fidelity of the output intensity distribution can be evaluated as

$$F_{HV} = \vec{I_H} \cdot \vec{I_V} \tag{6.3}$$

where $\vec{I_V}$ and $\vec{I_H}$ are the vectors of the output intensities when injecting V- and H-polarized light.

The measurement of the HV fidelity in the arrays used to fit κ shows that these structures are almost polarization-insensitive: in fact, despite the fitted laws differ from V- to H-polarized light, the HV fidelity of the output is rather high (always above 99% except for one outlier) as can be seen in graph 6.3. This has two consequences: first of all, we can consider the response of the device as polarization insensitive; secondly, it is reasonable to merge the data of the two polarizations to extract an averaged model for the decay of κ. The resulting exponential decay reads:

$$\kappa = 3.190 \cdot e^{-0.193 \cdot d} \tag{6.4}$$

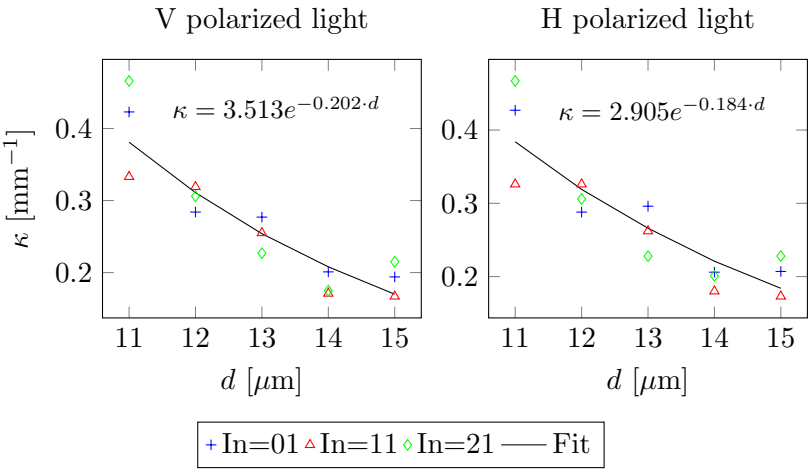

Figure 6.2: Fit of κ for vertical and horizontal polarization.

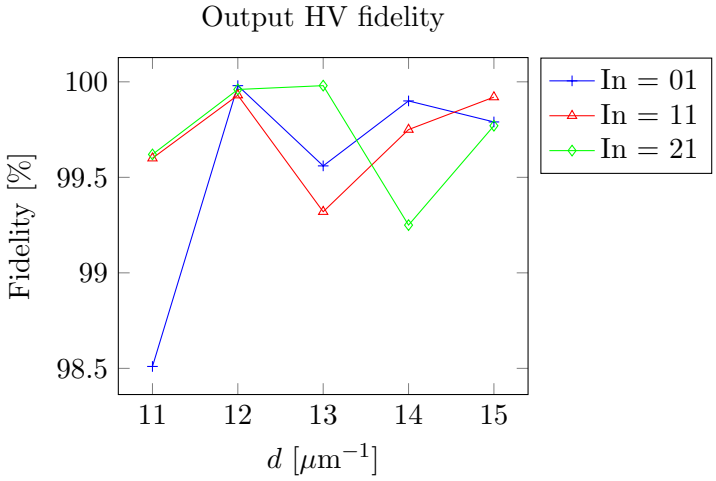

Figure 6.3: HV fidelity in the arrays for the fit of κ.

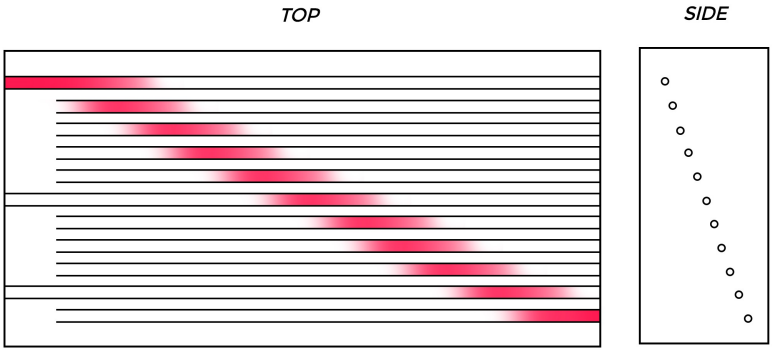

Figure 6.4: Scheme of the device: (a) top view and (b) output side view.

6.3 Analysis of the device parameter

6.3.1 Scheme of the device

In figure 6.4 a sketch of the prototype is proposed. As shown in the top view (figure 6.4a), the array will consist in a series of N waveguides with injection in different sites in order to study the transfer fidelities of different pairs of waveguides ($i \leftrightarrow N + 1 - i$). The interwaveguide distances is not uniform and will be set in order to achieve the correct couplings between the waveguides 2.15.

In figure 6.4b the sketch of the transversal section of the array is shown. As underlined previously, in order to be polarization insensitive, the array will extend diagonally at an angle $\theta \approx 60°$.

6.3.2 Re-parametrization of the problem

For a correct fabrication of the device, it is important to understand which are the main technological parameters that influence the performance of the array.

As explained in section 2.7.2, within the nearest-neighbour approxima-

tion, the Hamiltonian of a N-waveguide photonic lattice for PST is[2]

$$\mathcal{H} = \begin{bmatrix} 0 & \kappa_1 & 0 & \cdots & 0 \\ \kappa_1 & 0 & \kappa_2 & \cdots & 0 \\ 0 & \kappa_2 & 0 & \cdots & 0 \\ \vdots & \vdots & \vdots & \ddots & \kappa_{N-1} \\ 0 & 0 & 0 & \kappa_{N-1} & 0 \end{bmatrix} \tag{6.5}$$

and the evolution of the system with an input state $|\Psi_0\rangle$ is given by

$$|\Psi(z)\rangle = e^{-i\mathcal{H}z} |\Psi_0\rangle \tag{6.6}$$

The coefficients of the hamiltonian follow the "parabolic"distribution

$$\kappa_n = \kappa_0 \sqrt{n(N-n)} \tag{6.7}$$

where κ_0 can be related to the coordinate where perfect state transfer occurs (henceforth denoted by z_{PST}) through the relationship

$$\kappa_0 = \frac{\pi}{2z_{PST}} \tag{6.8}$$

Anyway, these equations give little technological insight since they hold true for any physical implementation of PST devices.

For an array of waveguides, κ_n are the couplings between adjacent waveguides. As mentioned before (section 2.7.1), the coupling of waveguides follows an exponential law, so that κ_n can be written as

$$\kappa_n = a \cdot e^{-b \cdot d_n} \qquad n = 1, \ldots, N-1 \tag{6.9}$$

where d_n is the distance between waveguides $n-1$ and n. For the specific form of eq 6.7, the relation between the coupling coefficients can be written in relation to the maximum κ of the structure:

$$\kappa_n = \kappa_{max} e^{-b \cdot \Delta_n} \tag{6.10}$$

where $\kappa_{max} = a \cdot e^{-b \cdot d_{min}}$, d_{min} is the minimum interwaveguide distance of the structure and Δ_n is the difference $\Delta_n = d_n - d_{min}$.

[2]Note that we have replaced $\kappa_{n,n+1} \to \kappa_n$ for the sake of simplicity.

With this re-parametrization, for an odd number of waveguides[3], the distances d_n follow the simple rule

$$d_n = d_{min} + \frac{1}{b}\log\left\{\frac{1}{2}\sqrt{\frac{N^2-1}{n(N-n)}}\right\} \tag{6.11}$$

which has more technological insight since it is related only to design parameters; PST distance z_{PST} is directly linked to d_{min} and the number of waveguides N by

$$z_{PST} = \frac{\pi\sqrt{N^2-1}}{4\cdot\kappa_{max}}, \qquad \kappa_{max} = a\cdot e^{-b\cdot d_{min}} \tag{6.12}$$

It is evident from the last equation that the three parameters z_{PST}, N and d_{min} are closely related. In the following section we will briefly analyse how these parameters are intertwined.

6.3.3 Analysis of the main design parameters

Usually, in a spin chain, the number of the spins N and their minimum distance d_{min} is given from the constraints of the system - e.g. the distance between the two endings of the chain or the coupling law between the spins - so that the time of perfect state transfer t_{PST} is determined by these two parameters.

In a PST waveguide array there are different constraints: for example, the refocusing distance z_{PST} is mainly limited by the propagation loss of the waveguides. Therefore, to properly design the PST waveguide array, it is necessary to understand how the three parameters z_{PST}, N and d_{min} are linked together.

Number of waveguides. From equation (6.12), it is evident that the number of the waveguides directly influences z_{PST}, since higher N means longer refocusing distances. Theoretically, there are no limitations to N; in practice, though, there are some issues that limit the maximum number of waveguides in the device. The most important one is that, in our tilted-array implementation, N determines the vertical extension of the array inside the glass. One possible problem related to the vertical extension of the

[3]For an even number of waveguides, the relationship is $d_n = d_{min} + \frac{1}{b}\log\left\{\frac{1}{2}\frac{N}{\sqrt{n(N-n)}}\right\}$.

array is related to the fact that the objective used for focusing the writing beam compensates for the spherical aberration only at a precise depth (170 μm); therefore, if the array extends too much vertically, the objective will focus outside its working depth and it could not compensate any more the spherical aberrations. This may lead to greater inhomogeneity within the array and it may cause unwanted side effects, e.g. aberrations could cause a wider spot size of the laser beam, which will deposit less power and induce a lower index change, resulting in waveguides with propagation constants β different from what expected.

Minimum spacing d_{min}. As already mentioned, along with N, also the minimum spacing d_{min} is closely related to the refocusing distance: increasing d_{min} will decrease the magnitude of κ_{max}, thus increasing z_{PST}. Also for d_{min} there are some practical limitations.

First of all, d_{min} determines the vertical extension of the array, with all the consequences already discussed talking about N. For this reason, attention must be paid when writing arrays with high d_{min}. The fabrication process also limits the lower range of d_{min}: in fact, the modification of the substrate induced by the femtosecond pulses to write one waveguide can change the neighbouring waveguides, thus affecting their guiding properties.

Another important issue is related to the interaction between non-next-neighbour waveguides. In fact, considering three waveguides and assuming the relation (6.9), the ratio r of the coupling between waveguides 1 and 3 ($\kappa_{1,3}$) and the coupling between waveguides 1 and 2 ($\kappa_{1,2}$) can be expressed as

$$r = \frac{\kappa_{1,3}}{\kappa_{1,2}} = e^{-b \cdot d_{2,3}}$$

being $d_{2,3}$ the distance between waveguides 2 and 3. This means that the closer the waveguides, the more effective is the coupling beyond the nearest neighbours. If not properly addressed, non-nearest-neighbour coupling leads to a degradation of the performance of the system, as will be analysed more thoroughly in section 7.1.

Coupling exponential law. From the re-parametrization of the problem, it is evident that the two parameters of the coupling law (6.9) give different contributions to the performance of the array.

The parameter a appears only in the denominator of the expression for z_{PST} (6.12), implying that its exact knowledge is of minor importance: an error on its esteem will reflect only in a shift of the refocusing point z_{PST}, and this can be taken in account by writing several devices at different lengths around the theoretical z_{PST} and then measuring the most efficient one.

The parameter b is more critical, since it appears in the equation that provides the interwaveguide spacings. Therefore, it is important to study how the performance of the ideal PST waveguide array depends on the correct esteem of b. With the help of numerical simulations, whose results are displayed in the graphs in figure 6.5, it is possible to analyse the dependence of fidelity and refocusing distance if the b used to design the device is different from the actual one in presence of nearest-neighbour. It can be seen that the fabrication of a device with a b_{real} different from the one adopted in the design stage (b_{design}) does not affect much the maximum fidelity, which remains above well 90% even in presence of large deviations; the error on the esteem of b affects also the refocusing distance z_{PST}, but this issue can be solved writing devices with different lengths and choosing the one with the best performance. It must be noted that, in this model, there is no dependence of fidelity with interwaveguide spacings d_{min}, while the error on z_{PST} have larger impact the higher is d_{min}.

6.4 Fabrication and analysis of the first device

All the fabricated PST waveguide arrays consist in a structure with an odd number of coupled waveguides N; the center of the structure, correspondent to the central waveguide, is located 170 μm below the top surface of the glass. Each array has 3 injections, namely waveguide number 1, $\frac{N+1}{2}$ and $N-1$. An example of the section of an 11-waveguide PST array can be found in figure 6.6.

We decided to focus our attention on the structures with $N = 11$ waveguides to avoid writing arrays extending too much from the nominal working depth of the writing objective. The arrays were tilted at an angle of 60° like the ones to characterize the decay of κ, since they showed satisfying HV fidelities at this angle, as mentioned above.

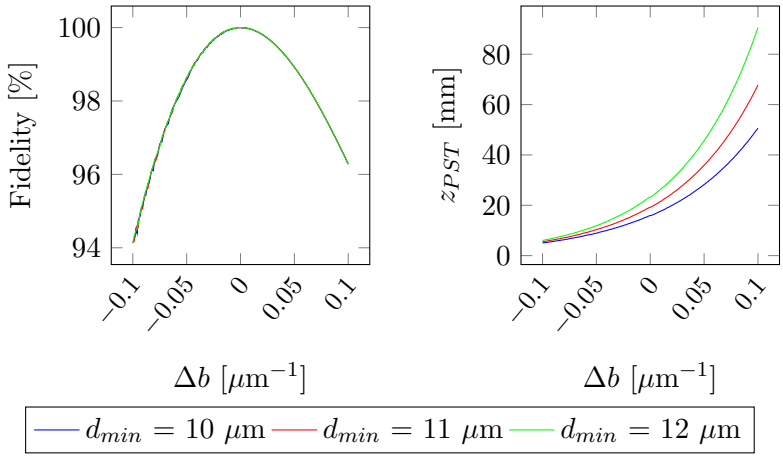

Figure 6.5: Dependence of fidelity (left) and distance of refocusing (right) with $\Delta b = b_{real} - b_{design}$, in case of nearest-neighbour couplings (parameter of the simulation: $b_{design} = 0.190\ \mu\text{m}^{-1}$, $N = 11$). It can be noted that the error on the transfer fidelity does not vary with the interwaveguide spacing (the graphs are superimposed).

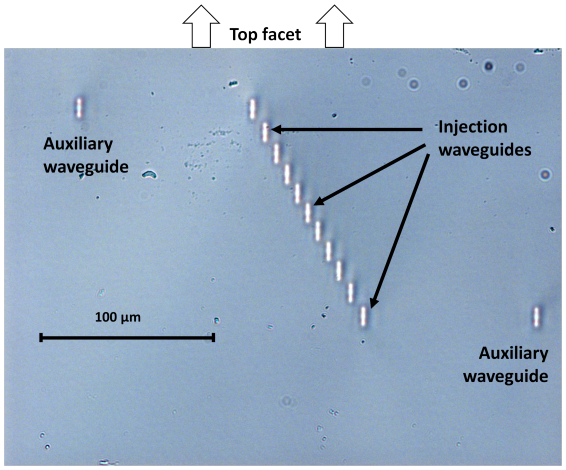

Figure 6.6: Vertical section of an 11-waveguide PST array. The auxiliary waveguides, located 100μm outside the array in correspondence to waveguides 1 and N, help to identify the two outermost injection waveguides, 1 and $N-1$, when coupling the device with a fiber.

Before addressing the fabrication of PST waveguide arrays that could exhibit light refocusing at z_{PST}, we fabricated and characterized ten PST arrays with $d_{min} = 11$ μm and different lengths, ranging from 1 mm to 10 mm, in order to check if the propagation of light was in accordance with the simulations. These structures have been analysed injecting V- and H-polarized light: the map of the propagation of V-polarized light is shown in the top row of figure 6.7, while the numerical simulation is displayed in the bottom row. It is evident that the propagation of light into the array is in accord with the theoretical simulation; anyway, from a closer inspection of the maps in figure 6.7, it appears that the actual propagation is more blurred than what simulated, suggesting that, in the device, light spreads too much with respect to the simulation.

It is possible to describe more quantitatively the propagation of light using the mean μ and the standard deviation σ of light distribution into the arrays. Considering the set $\{I_m\}_{m=1...N}$ of the output intensities of each waveguide m, it is possible to define the *mean* (or barycentre) of the distribution as

$$\mu = \sum_{m=1}^{N} m \cdot I_m \tag{6.13}$$

and its *standard deviation* as

$$\sigma = \sqrt{\sum_{m=1}^{N} (m-\mu)^2 \cdot I_m} \tag{6.14}$$

The informations conveyed by μ and σ are complementary: in fact, the barycentre μ of the distribution gives useful information about the average behaviour of light into the device while the standard deviation σ is important to quantify how the light spreads into the array.

Inspecting the graphs of the barycentre μ of the light in the fabricated arrays (top row of figure 6.8), it is possible to confirm that the propagation of light is overall in accordance with the theoretical simulation. On the other hand, the comparison of the σ of the distributions with the theoretical simulations highlights that the behaviour of the device slightly departs from the theoretical one after $z \sim 5$ mm (bottom row of figure 6.8). This effect may be caused by different non-ideality factors, like non-nearest-neighbour couplings or undesired gradients in the propagation constants.

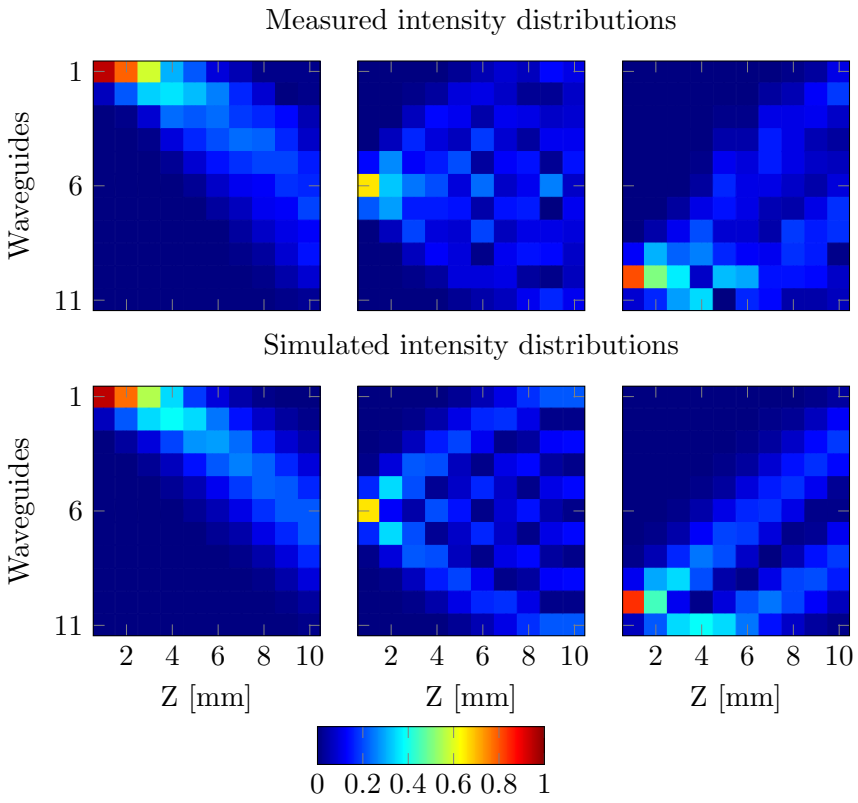

Figure 6.7: Map of the intensity distribution into a PST array with $N = 11$ and $d_{min} = 11$ μm, for z $\in$ [1,10] mm. Measurement obtained injecting vertically polarized light in the PST array (top row) and correspondent simulations with $a = 3.6$ mm^{-1} and $b = 0.190$ μm^{-1} (bottom row).

At last, the analysis of HV fidelity confirms an almost polarization-insensitive propagation (figure 6.9).

In conclusion, it seems that a PST array with $N = 11$ waveguides and $d_{min} = 11$ μm could exhibit perfect state transfer with a good polarization insensitivity.

In these first prototypes we also monitored the accuracy and reproducibility of the fit (6.4) of the decay of the coupling coefficient. We tried to reconstruct the correct exponential decay by replicating numerically the results of the measurement on the PST arrays. The resulting exponential law was found to be

$$\kappa = 3.6 \cdot e^{-0.190 \cdot d} \tag{6.15}$$

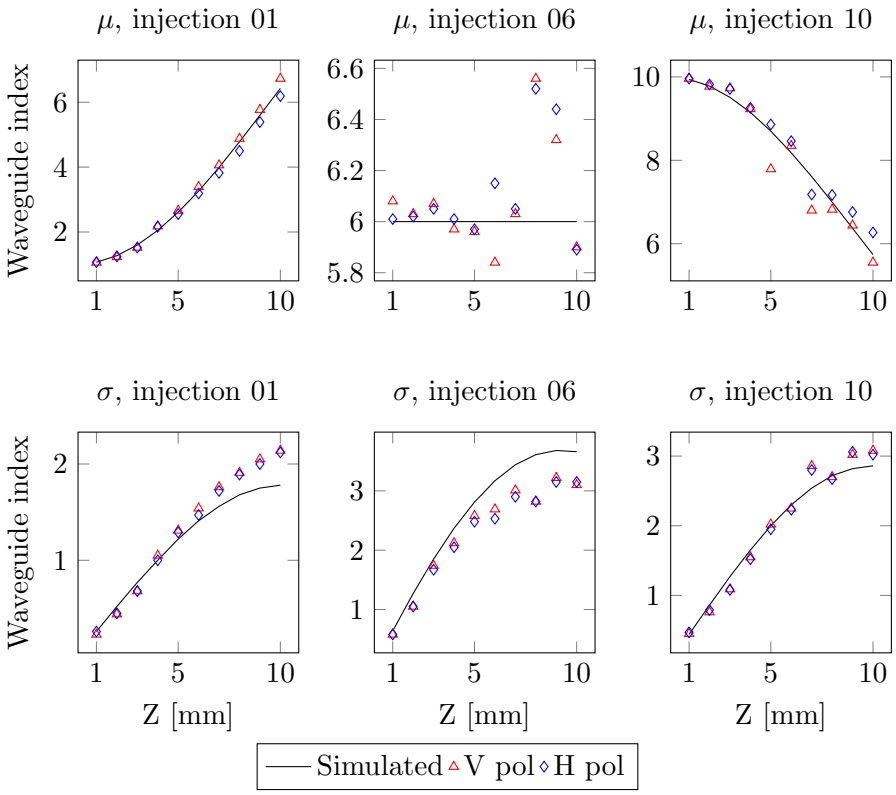

Figure 6.8: Analysis of the mean and variance of the intensity distribution into a PST array with $N = 11$ and $d_{min} = 11$ μm.

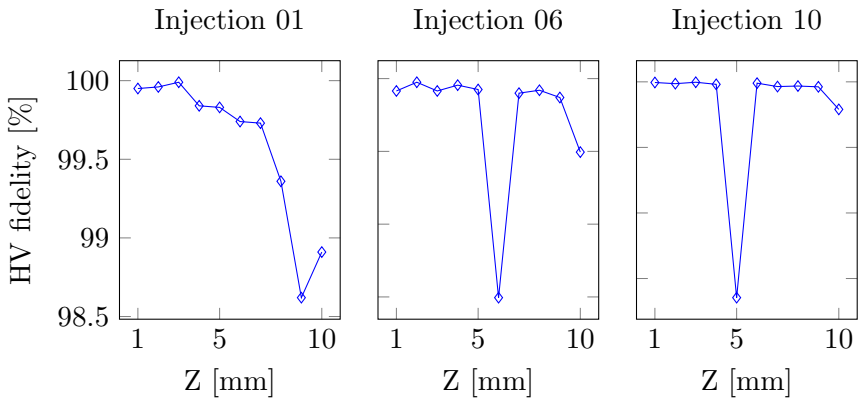

Figure 6.9: HV fidelity of the PST array with $N = 11$ and $d_{min} = 11$ μm, for z $\in$ [1,10] mm.

thus very close to the one found previously.

The parameters of the exponential law are slightly different from the one found from the fit of κ (eq. (6.4). However, the difference on a has little importance, since it influences only the refocusing distance, as seen in the last paragraph; as regards b, the small difference (0.003 μm^{-1}) between the two fits (6.4) and (6.15) reflects in a maximum error of 45 nm in the spacing of the waveguides, leading to a decrease of $\sim 1\%$ of the fidelity.

To realize a first complete device, we fabricated two sets of sixteen structures with $N = 11$ waveguides: the first set has $d_{min} = 11$ μm with lengths ranging from 15.0 mm to 22.5 mm, while the second set has $d_{min} = 12$ μm with lengths ranging from 21.5 mm to 29.0 mm. The lengths of the arrays has been chosen to span around the refocusing distances ($z_{PST} \approx 19.0$ mm and ≈ 23.0 mm, respectively).

The purpose of the second set is to have arrays with greater interwaveguide spacings, to reduce eventual non-nearest-neighbour coupling effects present in the first set: even if in the preliminary trial we found only small deviations from the numerical simulation, it is possible that we were not able to see the contribution of higher-order couplings because their effects become relevant only in longer arrays. A comprehensive representation of the performance of the two sets of devices can be found in figures 6.10, 6.11, 6.12.

The maps of distribution of light inside these structures are shown in

	F_T [V pol]	F_T [H pol]
In 01	87,3%	81.8%
In 06	72.5%	65.8%
In 10	62.7%	57.0%

Table 6.1: Performances of the PST waveguide array with $d_{min} = 12$ μm at $z = 22.5$ mm.

figure 6.10. Comparing the two different devices (top and middle rows) with the theoretical simulations in the nearest-neighbour approximation, it is evident that the overall behaviour of both is coherent with what expected. Anyway, while the transfer $1 \rightarrow 11$ is close to be optimal, when light is injected into waveguides 6 and 10 the degradation of the performance is evident and apparently there is no difference between the structures with $d_{min} = 11$ μm and 12 μm.

The same conclusions can be drawn from the analysis of the *transfer fidelities* in figure 6.11. Following the definition 6.1, the transfer fidelity F_T of the PST waveguide array is defined as

$$F_T = \vec{I}_{out} \cdot \vec{I}^{th}_{out}$$

where $\vec{I}^{th}_{out}$ is the theoretical output in case of perfect state transfer and $\vec{I}_{out}$ is the measured output. This is a synthetic parameter that indicates the efficiency of the state transfer in the array.

From the analysis of the transfer fidelity, we observe that only injecting light into waveguide 1 the measurement are comparable with the numerical simulation. Moreover, we noted that the devices with the highest transfer fidelity where the ones with $d_{min} = 12$ μm.

Concluding, the overall performance of the device with $d_{min} = 12$ μm are reported in table 6.1.

Despite non optimal, these first results are satisfying for two reasons:

- the maximum transfer fidelity, $F_T = 87\%$, is achieved for the $1 \rightarrow 11$ transfer in the array with $d_{min} = 12\,\mu$m and $L = 22.5$ mm injecting V-polarized light. This is a transfer fidelity higher than the one reported by Perez-Leija *et al.* [43]; in addition, our device is almost four time shorter.

- we managed to achieve almost perfect polarization insensitivity, as can

be seen in figure 6.12. In particular, the HV fidelity of the array with $d_{min} = 12\,\mu$m is, on average, higher than 97%.

To understand better the causes of the evidenced non-idealities is necessary to analyse the main sources of noise and non-idealities and to find strategies to address these problems.

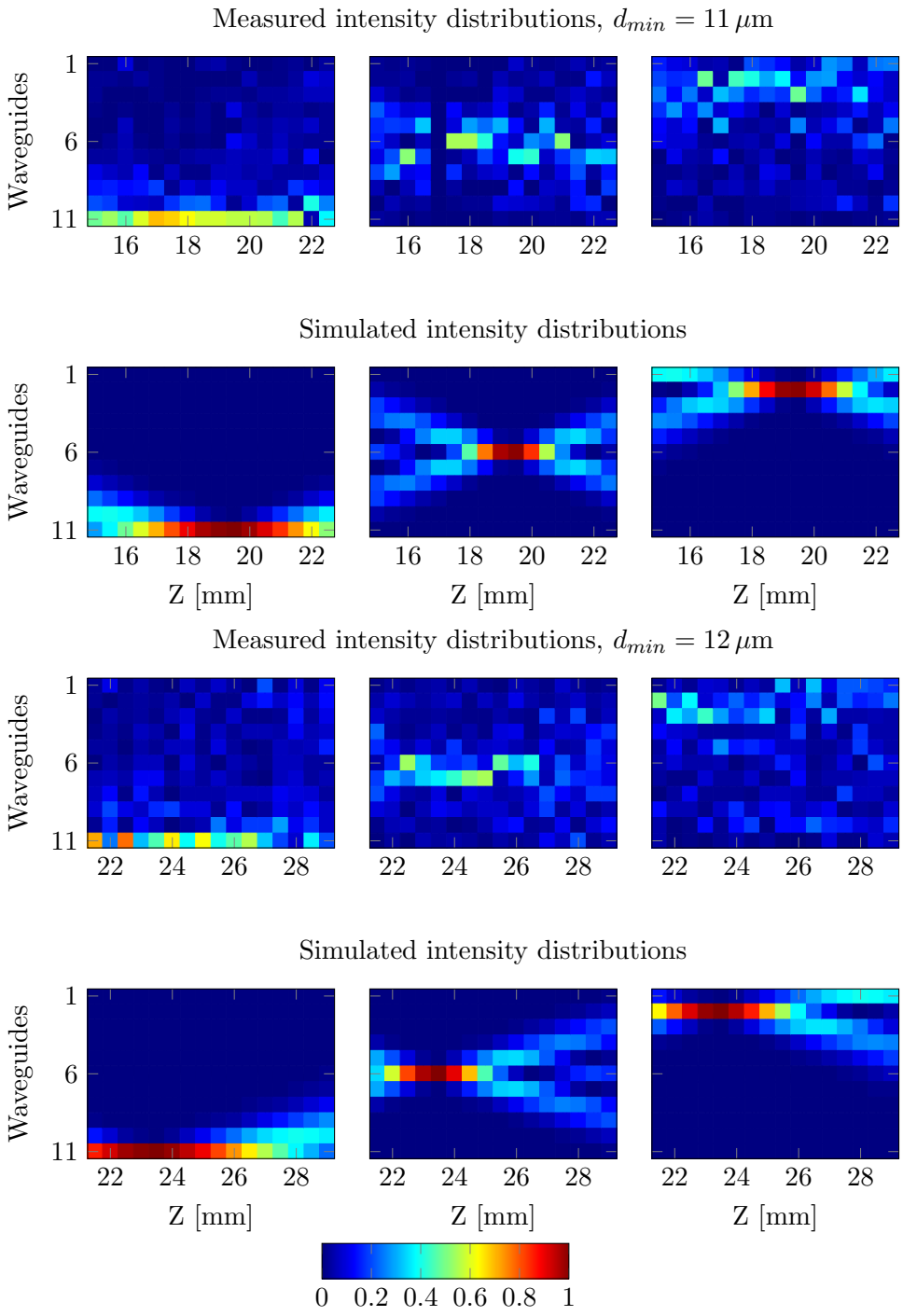

Figure 6.10: Maps of light distribution in the region around z_{PST} for the PST arrays with $N = 11$ waveguides and $d_{min} = 11\,\mu$m (top row) and $d_{min} = 12\,\mu$m (middle row), injecting V-polarized light. In the bottom row, the simulation of the theoretical behaviour of the device around z_{PST}.

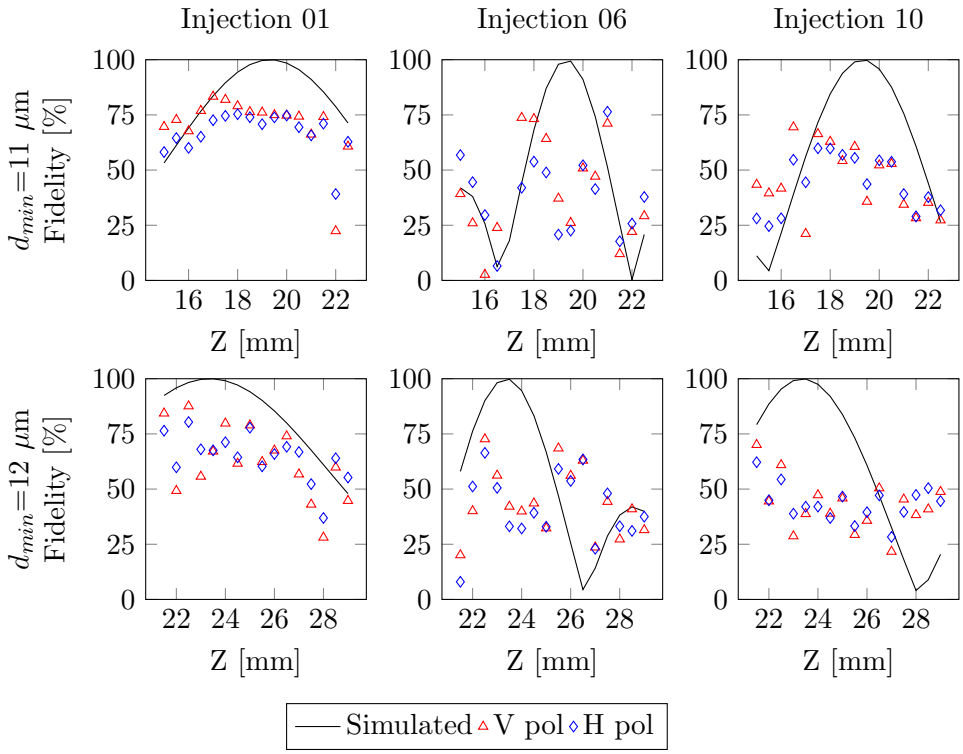

Figure 6.11: Comparison between the theoretical transfer fidelities (solid line) and the measured ones for the arrays with $d_{min} = 11$ μm (top row) and 12 μm (bottom row).

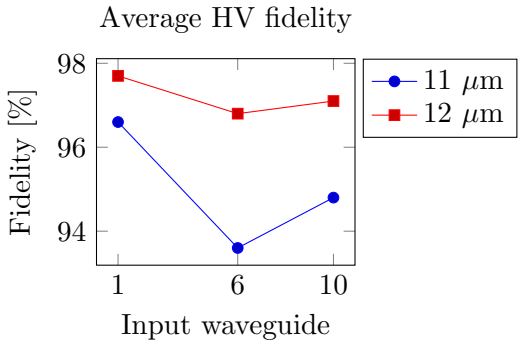

Figure 6.12: Comparison of average HV fidelities of the devices with $d_{min} = 11\,\mu$m and $12\,\mu$m.

Chapter 7

Numerical analysis of possible causes of imperfections

In chapter 6 we reported the fabrication and characterization of a first PST waveguide array that enables state transfer between waveguides $1 \rightarrow 11$, $6 \rightarrow 6$ and $10 \rightarrow 2$.

Despite showing state-of-the-art efficiency for the PST between waveguides 1 and 11, the performances of the device when light is injected in waveguides 6 and 10 are far from being optimal. It is thus necessary to understand the causes of this degradation of the performances in order to define a strategy to improve the overall fidelity of the device.

In this chapter, we will analyse two possible causes of the imperfect behaviour of the fabricated devices by means of numerical simulations.

7.1 Non-nearest-neighbour couplings

The first possible cause of performance degradation is the influence of non-nearest-neighbour interactions. In fact, in the last chapter we analysed the fabricated devices referring to a model that considers only interactions between the nearest-neighbour waveguides (henceforth referred to as *NN model*). Anyway, as already mentioned in section 2.2.2, non-nearest-neighbour couplings could degrade the transfer fidelity of the PST waveguide array. By performing an eigenvalues analysis, it is understood that PST dy-

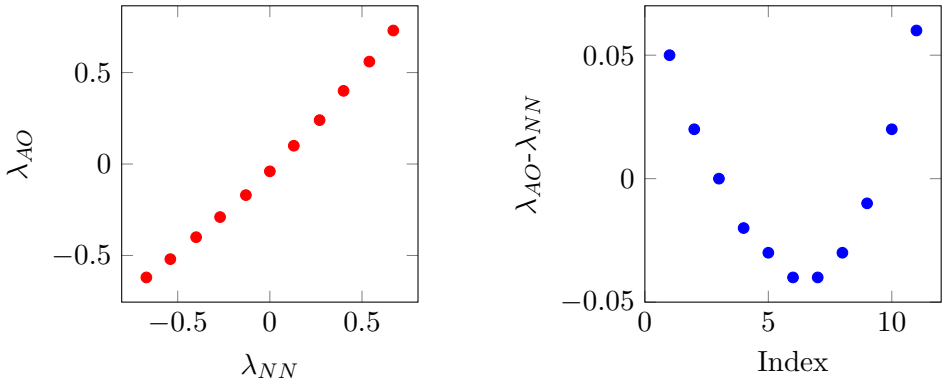

Figure 7.1: Eigenvalue spectra of a PST wavegude array with $d_{min} = 12$ μm, $N = 11$ and $\kappa = 3.6e^{-0.190 \cdot d}$ within the NN and the AO models. On the left: comparison between the eigenvalue spectra of the J_x Hamiltonian in the NN model and in the AO model. On the right: difference between the two spectra $\lambda_{AO} - \lambda_{NN}$.

namics of a J_x chain is actually based on its equally spaced eigenvalues set: this particular conformation of the spectrum leads to proper interference effects between the eigenvectors so that the state injected in waveguide i at $z = 0$ is retrieved exactly in waveguide $N+1-i$ at $z = z_{PST}$. The presence of non-nearest-neighbour couplings distorts the eigenvalue spectrum (figure 7.1) and this leads to wrong interferences effects that spoil the perfect state transfer. For this reason, a more general model considering also non-nearest-neighbour couplings (henceforth referred to as *AO model* - all-order model) has been used to compare the measurement with the simulations.

To understand the main differences between the two approximations, we simulated the behaviour of different devices with increasing interwaveguide spacings within the AO model. In figure 7.2 the propagation of light in the ideal case (top row) and in three different devices with $d_{min} = 11$, 13 and 15 μm is shown. The effect of the perturbation caused by non-nearest-neighbour couplings is evident: light propagation, especially when entering in the centre of the array, is blurred and refocusing is not perfect. Moreover, as can be evinced from the graphs in figure 7.3, as the interwaveguide distances become bigger, the transfer fidelity gets higher, since the non-nearest-neighbour couplings become less effective, as already discussed in section 6.3.3.

From this analysis, it appears that the role of the non-nearest-neighbour

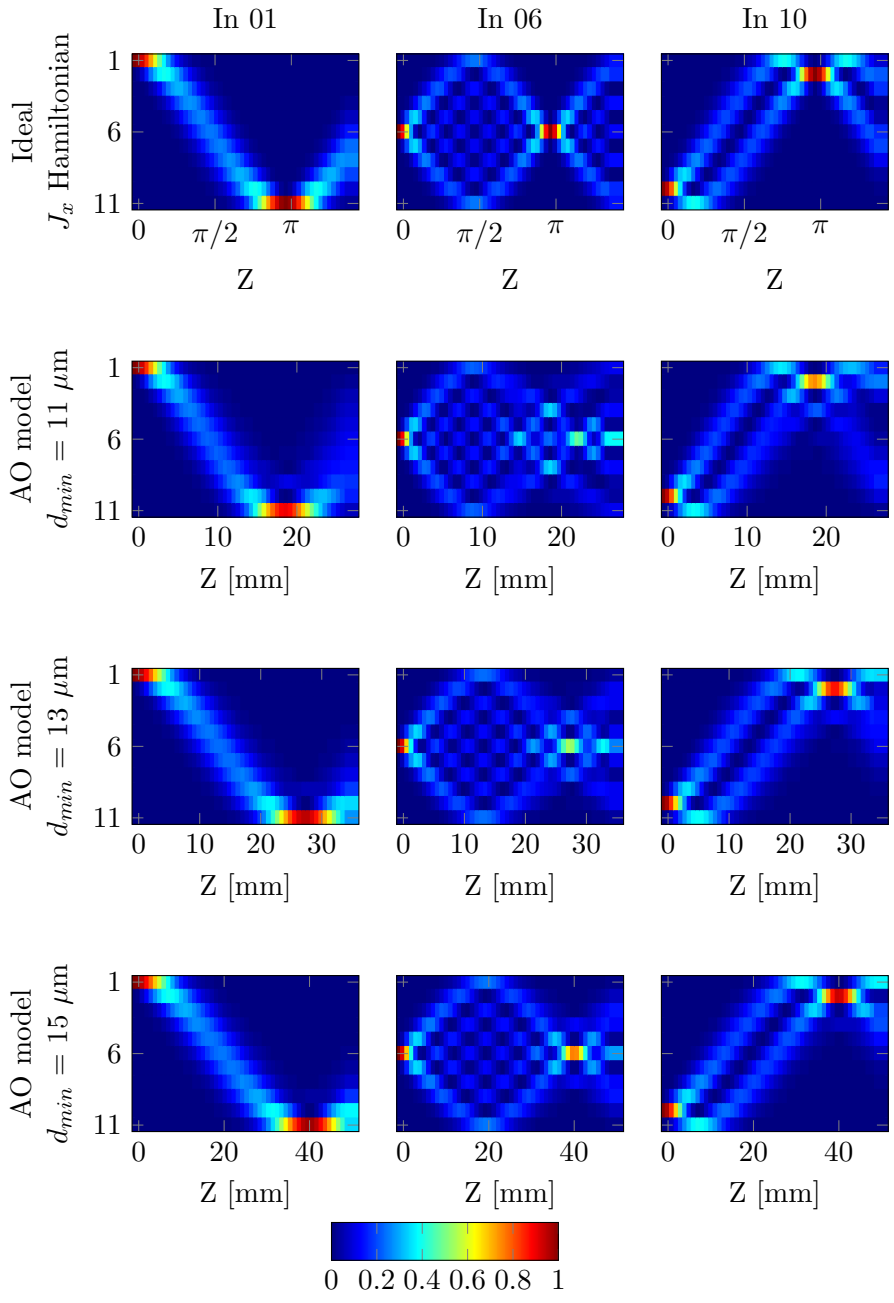

Figure 7.2: Maps of light propagation inside a J_x photonic lattice in the ideal case (top row) and in presence of non-nearest-neighbour couplings, for different interwavguide lengths (d_{min} = 11, 13 and 15 μm).

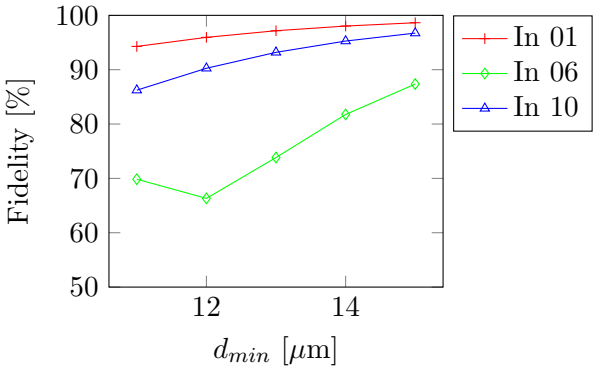

Figure 7.3: Example of the degradation of the theoretical transfer fidelity when non-nearest-neighbour couplings are considered, for d_{min} = 10, 11, 12, 13 and 14 μm and different inputs.

couplings cannot be neglected, since it can drastically affect the transfer fidelity of the device.

7.2 Intrinsic gradient of the propagation constants

Another possible cause of degradation of the performances is the presence of a gradient of the propagation constants β_i of the waveguides in the device. As previously mentioned, the arrays are written using an objective that compensates the spherical aberration 170 μm below the surface of the glass, which means that, at this depth, the focal spot size of the laser beam is the smallest possible. Anyway, since the arrays extend vertically, the beam will be focused outside the working region of the objective, possibly leading to a distortion of the focal volume caused by the aberrations. This results into a lower amount of energy deposited in the substrate and, since the modification of the refractive index is directly related to the energy deposited by the beam, in a difference in the induced refractive index change. Therefore waveguides distant from the optimum writing depth may be *detuned* with respect to the ones at 170 μm, i.e. there is a difference $\Delta\beta$ between their propagation constants. In presence of a gradient of the propagation

constants, the Hamiltonian of the system becomes

$$\mathcal{H} = \begin{bmatrix} \Delta\beta_1 & \kappa_1 & 0 & \cdots & 0 \\ \kappa_1 & \Delta\beta_2 & \kappa_2 & \cdots & 0 \\ 0 & \kappa_2 & \Delta\beta_3 & \cdots & 0 \\ \vdots & \vdots & \vdots & \ddots & \kappa_{N-1} \\ 0 & 0 & 0 & \kappa_{N-1} & \Delta\beta_N \end{bmatrix}$$

Since the detuning $\Delta\beta$ depends monotonically on the spot size and since the latter has a minimum at 170 μm below the glass surface, the lowest order Taylor expansion is parabolic. Therefore, the detuning $\Delta\beta_\nu$ can be generically expressed as $\Delta\beta_\nu = C(\nu - \nu_0)^2$, where ν_0 is the index of the waveguide at 170 μm. Therefore, in the simulations below, we have adopted the following model for the detuning

$$\Delta\beta_\nu = C(\nu - 6)^2 \tag{7.1}$$

Light propagation inside PST waveguides array (N=11, d_{min}=11μm) within the NN model in presence of parabolic gradients of different magnitudes is reported in figure 7.4. These maps show that the presence of gradients contributes to the degradation of the refocusing of light. The entity of this degradation can be assessed inspecting the transfer fidelity $1 \rightarrow 11$ with different values of C, as shown in figure 7.5. It is evident that the presence of a gradient has a great impact on the transfer fidelity.

7.3 Conclusions

After having simulated these possible causes of performance degradation, we tried to understand whether these are present in the fabricated devices. However, from the maps of the PST waveguide arrays discussed in chapter 6 it is difficult to figure out whether the causes of fidelity degradation outlined in this chapter are present or not in our structures. For this reason, we decided to investigate the influence of the non-nearest-neighbour couplings and the presence of an intrinsic gradient of the propagation constants with specific experiments which will be described in the next chapter.

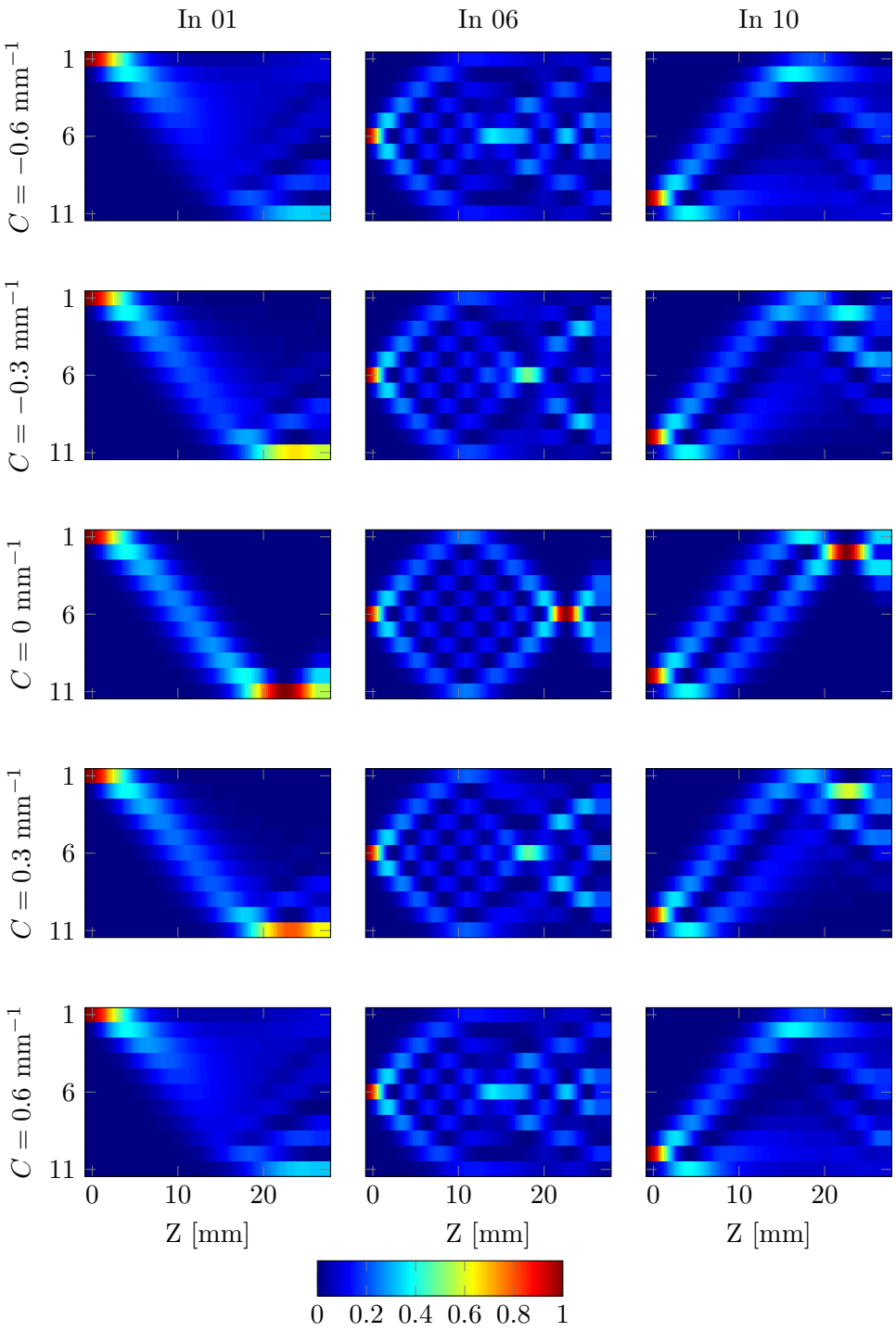

Figure 7.4: Maps of light propagation inside a J_x photonic lattice in the in presence parabolic detuning (7.1), with different C.

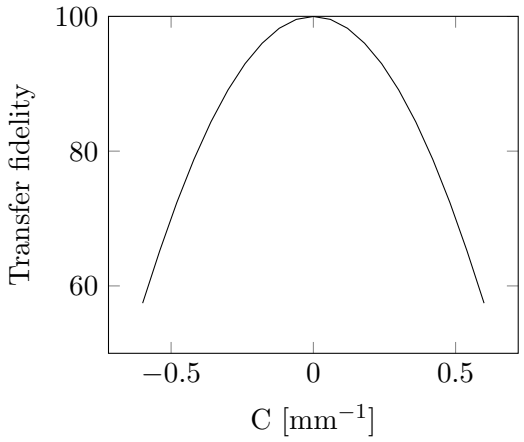

Figure 7.5: Dependence of the transfer fidelity of the light distribution in a PST waveguide array (N=11, d_{min}=12 μm) with the detunings magnitude C, when injecting light into waveguide 1.

Chapter 8

Compensation of the possible causes of imperfection

After having simulated some possible causes of performance degradation, we decided to study them separately. At first, we tried to understand the influence of the interwaveguide distances and then the possible presence of a gradient in the propagation constants.

8.1 Influence of the interwaveguide distance

As seen in the last chapter, within the AO model, it resulted that higher fidelities could be reached writing devices with larger d_{min} (see figure 7.3). Therefore, we decided to investigate the performances of PST waveguide arrays with different interwaveguide distances to check if the actual trend of the fidelity was the one simulated theoretically. Moreover, spacing out the waveguides has the additional advantage that the writing of one waveguide has a lower impact on the neighbouring, which should lead to an overall improvement of the system fidelity.

To this aim, we fabricated[1] three sets of devices as follows:

- ten PST waveguide arrays with $d_{min} = 12$ μm and lengths between 17 and 26 mm

[1] Due to some changes in the writing setup, it has been necessary to characterize again the coupling coefficients. The resulting exponential law was

$$\kappa = 2.84e^{-0.161 \cdot d}$$

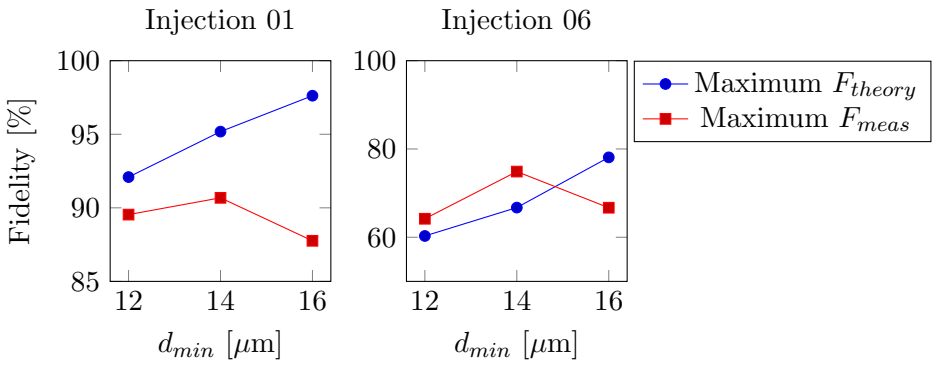

Figure 8.1: Analysis of the simulated and measured transfer fidelities for the PST waveguide arrays with different interwaveguide distances (V-polarized light).

- eleven PST waveguide arrays with $d_{min} = 14$ μm and lengths between 20 and 40 mm
- eleven PST waveguide arrays with $d_{min} = 16$ μm and lengths between 30 and 50 mm.

The performances of the arrays are reported in figure 8.1. From the numerical analysis of the transfer fidelity, we would expect that moving to greater distances will increase the transfer fidelity of the system. Anyway, the experiments reveal a more complex pattern: F_{meas} increases passing from 12 to 14 μm, but it decreases when we consider the array with 16 μm. Moreover, the difference between the theoretical and the experimental fidelity becomes higher as d_{min} increases.

This behaviour could be explained considering that increasing the distances between the waveguides reduces the non-nearest-neighbour couplings and the interferences between the waveguides during the fabrication of the array, but it also leads to longer refocusing distance z_{PST} and thus longer arrays. Therefore, the transfer fidelity is degraded by the interference between adjacent waveguides for arrays with small d_{min}, while, for high d_{min}, the longer propagation distance makes the structure more sensitive to any small imperfection. For example, the propagation constant β of a waveguide is dependent on the characteristics of the beam during the fabrication. Therefore, any small fluctuation in the power of the beam or any variation in the focusing condition (e.g. a local deformation of the substrate) can

	V polarization		*H polarization*		*Simulation*	
	F	z_{PST}	F	z_{PST}	F	z_{PST}
In 01	90.6%	28 mm	81.5%	30 mm	95.2%	28 mm
In 06	74.9%	36 mm	72.0%	38 mm	66.7%	34 mm
In 10	67.9%	28 mm	58.1%	30 mm	88.1%	28 mm

Table 8.1: Performances of the PST waveguide array with $d_{min} = 14$ μm and comparison with the theoretical simulations.

vary β locally. This fluctuations of β have little impact if the couplings with the adjacent waveguides is high, while it becomes relevant if the coupling is relatively weak. For this reason, arrays with higher d_{min} have lower inter-waveguide couplings and longer waveguides, so that these small fluctuations are not negligible. This is why the transfer fidelity and the average fidelity with the simulation drop when moving from $d_{min} = 14$ μm to 16 μm.

The PST waveguide array with $d_{min} = 14$ μm has demonstrated the best performances, so far, and its transfer fidelities are reported in table 8.1.

8.2 Gradient of the propagation constant

To investigate the presence of a gradient of the propagation constants, we decided to work on uniform arrays with waveguides sufficiently spaced to study the phenomenon on simpler structures where only nearest-neighbour couplings are present. Following the discussion in section 7.2, we have performed numerical simulations on these arrays imposing gradients with different parabolic profiles $\Delta\beta_\nu = C(\nu - 6)^2$. Interestingly, we noticed that the entity of the gradient influences the spreading of light inside the array. In particular, monitoring the dependence of the σ of the light distribution[2] with C, we noted that, when injecting light from the central waveguide and when the light distribution has the maximum width, its σ is maximum when no detuning is present (figure 8.2). To study the presence of the intrinsic gradient, we decided to analyse the response of structures where an external counter-gradient has been imposed, so that the resulting detuning can be

[2] As defined in section 6.4, the parameter σ is the standard deviation of the intensity distribution of the light into the array.

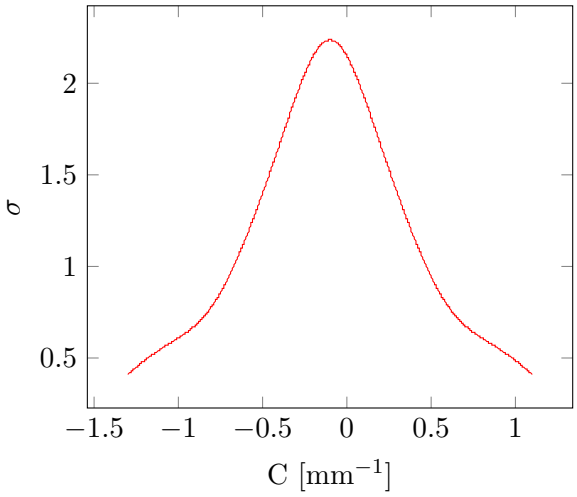

Figure 8.2: Numerical simulation of the dependence of σ in uniform arrays with $L = 24$ mm, intewaveguide distance $d = 19$ μm and $\kappa = 0.066$ mm^{-1}, in presence of parabolic gradients of the detunings $\Delta\beta_\nu$=$C(\nu - 6)^2$.

written as

$$\Delta\beta(\nu) = \Delta\beta_{intrinsic} + \Delta\beta_{external} = C(\nu - 6)^2 + C_{ext}(\nu - 6)^2$$

The maximum σ will be reached when C_{ext}=$-C$ and, in this way, we will be able to retrieve the correct profile of the intrinsic gradient of the structure.

In order to induce such counter-gradient, it is possible to modulate the propagation constant of a waveguide by acting on its writing speed: in fact, acting on this parameter, it is possible to vary the amount of energy deposited locally, therefore inducing different refraction index changes and thus varying propagation constant of the waveguide. Supposing a linear dependence $\Delta\beta \propto \Delta v_{writing}$, we fabricated eleven uniform arrays with interwaveguide spacing d=19 μm and velocity profiles following the law

$$v_\nu^{(i)} = \alpha^{(i)}(\nu - 6)^2 + v_0^{(i)} \tag{8.1}$$

to provide the parabolic counter-gradient. The parameter α varies from -1.2 mm/2 to 1.2 mm/s with steps of 0.24 mm/s, while the offset is set appropriately to obtain the velocity profiles represented in figure 8.3a.

The measured σ are represented in figure 8.3b. The array with the

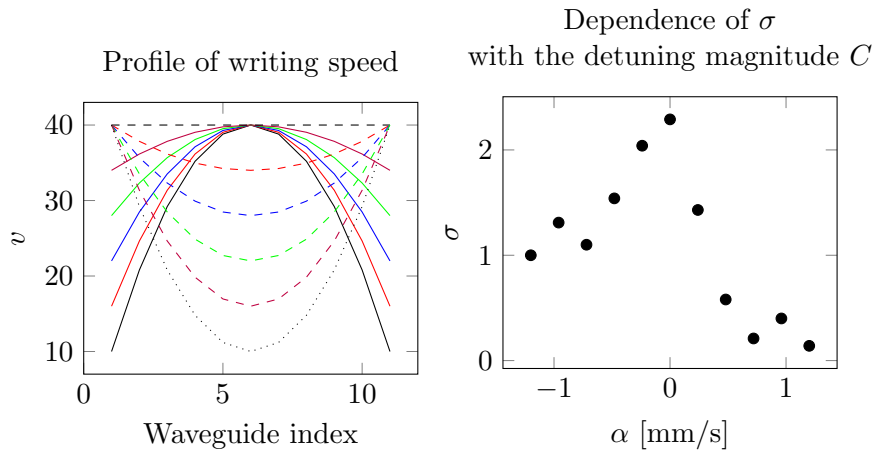

Figure 8.3: (a) Velocity profiles used for the fabrication of the uniform arrays in order to induce an external parabolic gradient; (b) Measured σ of the arrays, identified by the α provided to impose the counter-gradient (equation (8.1)).

maximum σ is the one with no compensation ($\alpha^{(i)}$=0$\rightarrow$ C_{ext}=0), suggesting that the intrinsic gradient is negligible.

8.3 Correction of the eigenvalues

8.3.1 Algorithm for the solution of the inverse eigenvalue problem.

From the previous analysis, we concluded that the non-nearest-neighbour couplings have an important impact on the transfer fidelity, while the effects of the intrinsic gradient are negligible. Since increasing the interwaveguide distances was not sufficient to reach higher fidelities, we had to find alternative ways to improve the performances.

The main limitation of the fabricated PST waveguide arrays appears to be the non-nearest-neighbour couplings, which distort the eigenvalue spectrum of the J_x Hamiltonian, as shown in figure 7.1. In order to solve this issue, we turned our attention to the solution of the inverse eigenvalue problem (IEP) connected to our system.

The study of IEPs is related to the reconstruction of a matrix given

certain constraints of its spectral structure [88]. In particular, we decided to implement the algorithm for the solution of the IEP specific to the 1D-spin chains with non-nearest-neighbour couplings proposed by Kay [89], detailed in the following.

Consider a generic 1D spin chain composed of N spins described by a spin-preserving centro-symmetric Hamiltonian like

$$\begin{cases} \mathcal{H} = -\sum_{n=1}^{N-1} J_n \vec{\sigma}_n \cdot \vec{\sigma}_{n+1} + \sum_{n=1}^{N} B_n \sigma_n^z \\ J_n^2 = J_{N-n}^2 \\ B_n = B_{N+1-n} \end{cases}$$

and suppose that the coupling strengths between non-nearest-neighbour act only as a perturbation to the ideal, nearest-neighbour Hamiltonian. From the hypothesis of mirror symmetry, there are only N free parameters we can act on to correct the eigenvalues of the system, namely $\frac{N+1}{2}$ external magnetic fields B_i and $\frac{N-1}{2}$ distances[3] $r_{i,i+1}$, which can be grouped in a single vector $\vec{\alpha} = \{r_{i,i+1}, B_i\}$. Therefore, in the single excitation subspace, the Hamiltonian of the system can be described by a $N \times N$ matrix $\mathcal{H} = \mathcal{H}(\vec{\alpha})$.

The IEP consists in finding the suitable values $\vec{\alpha}$ for the free parameters so that the eigenvalue spectrum of the Hamiltonian $\mathcal{H}(\vec{\alpha})$ matches a desired one, stored in the matrix Λ_{id}. Starting from a first estimate ($\vec{\alpha_0}$) of $\vec{\alpha}$ and assuming that the perturbation of the non-nearest-neighbour is small, we can consider that $\mathcal{H}(\vec{\alpha_0})$ is diagonalized by U_0 so that

$$\mathcal{H}(\vec{\alpha_0}) = U_0 \Lambda_0 U_0^\dagger = U_0 \Lambda_{id} (\mathbb{I} + \epsilon E_0) U_0^\dagger$$

being E_0 the diagonal matrix containing the error between Λ_0 and Λ_{id}, and ϵ is a small parameter. Then, considering a corrected set of parameters $\vec{\alpha_1} = \vec{\alpha_0} + \epsilon \vec{\delta\alpha}$, the Hamiltonian $\mathcal{H}(\vec{\alpha_1})$ can be diagonalized as follows

$$\mathcal{H}(\vec{\alpha_1}) = U_1 \Lambda_1 U_1^\dagger = U_1 \Lambda_{id} (\mathbb{I} + \epsilon E_1) U_1^\dagger$$

[3] For simplicity, we can consider that the coupling strength is a function of the distance $r_{i,j}$ between two spins and invoke the physical restraint that it should drop off as r increases, e.g. $J_{i,j} \sim 1/r_{i,j}^3$ or $\sim e^{-br_{i,j}}$.

It can be demonstrated that, in order to obtain $\Lambda_1 = \Lambda_{id}$, $\vec{\delta\alpha}$ must be the solution to

$$K \cdot \vec{\delta\alpha} = \vec{e} \tag{8.2}$$

where $\vec{e}$ is the vector of the diagonal elements of $-\Lambda_{id}E_0$ and K is a matrix whose i-th column is given by

$$K(:,i) = U_0^\dagger \left.\frac{\partial \mathcal{H}}{\partial \alpha_i}\right|_{\vec{\alpha_0}} U_0$$

If $\vec{\delta\alpha}$ is small compared to $\vec{\alpha_0}$, the algorithm can be iterated to obtain greater precision. It can be demonstrated that an accuracy of ϵ_0 can be achieved in $O(\log(\epsilon_0))$ iterations.

We implemented the algorithm in Matlab, adapting the algorithm to the problem of finding the correct interwaveguide distances d_n and detunings $\Delta\beta_n$ to impose a linear eigenvalue spectrum on the Hamiltonian of the PST waveguide array.

At first, we calculate the matrix Λ_{id} from the Hamiltonian $\mathcal{H}_{id}$ of the PST waveguide array considering only nearest-neighbour couplings. Then, considering also non-nearest-neighbour couplings, we compute the matrix $\mathcal{H}_0$, in order to extract the matrix of eigenvectors U_0 and the matrix of eigenvalues Λ_0. Therefore, the matrix of the errors E_0 is determine by $E_0 = \Lambda_0 - \Lambda_{id}$, and $\vec{e} = -\frac{E_0}{\epsilon}$, where ϵ is a small parameter. Finally, after having calculated $K(:,i) = U_0^\dagger \left.\frac{\partial \mathcal{H}}{\partial \alpha_i}\right|_{\vec{\alpha_0}} U_0$, it is possible to retrieve $\vec{\delta\alpha} = K/\epsilon$, so that the new corrected parameters are given by $\vec{\alpha_1} = \vec{\alpha_0} + \epsilon\vec{\delta\alpha}$.

From this algorithm, it is possible to extract the correct set of parameters $\vec{\alpha}$=$\{d_n;\ \Delta\beta_n\}$ to fabricate a PST waveguide array whose Hamiltonian has the correct equally spaced spectrum. Anyway, to implement the correction of the eigenvalues, we need to properly detune the waveguides by modulating the writing velocities. It is thus necessary to characterize precisely the dependence between $\Delta\beta$ and the writing velocity v.

8.3.2 Characterization of the relation $\Delta\beta = f(\Delta v)$

The algorithm above allows the retrieval of the correct d_n and $\Delta\beta_n$ to obtain perfect state transfer. Anyway, the relation between $\Delta\beta$ and the writing speed needs to be investigated experimentally.

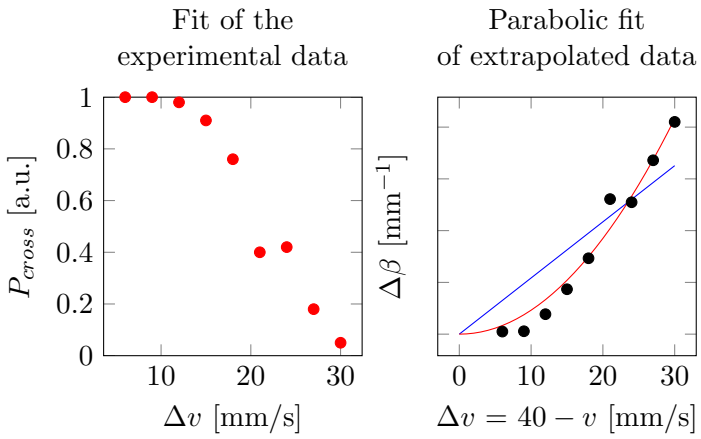

Figure 8.4: Left graph: measured normalized P_{cross}. Right graph: after the inversion of equation (8.3), the experimental data (black dots) have been fitted with a linear and a parabolic fit (blue and red solid line, respectively), to extract the relation between $\Delta\beta$ and Δv.

To extract the relation between $\Delta\beta$ and v, we fabricated eleven directional couplers with $\kappa = 0.28$ mm^{-1} and length $L = 5.5$ mm. The writing velocity for the injection waveguide has been kept fixed at 40 mm/s, while, for the other waveguide, it has been varied from 40 mm/s to 10 mm/s.

As reported in Ref. [58], in a directional coupler the power P_{cross} transferred from the injection waveguide to its neighbour follows the equation

$$P_{cross}(L, \kappa, \Delta\beta) = \frac{4\kappa^2}{4\kappa^2 + \Delta\beta^2} \sin\left(\frac{1}{2}\sqrt{4\kappa^2 + \Delta\beta^2}\, L\right)^2 \tag{8.3}$$

From the fabricated directional couplers we extracted the dependence between P_{cross} and Δv. Then, assuming that κ does not change varying the writing velocity of the second waveguide, we inverted equation (8.3) to extract the $\Delta\beta$ correspondent to each Δv. The best fit of the data is shown in figure 8.4, graph on the right, and is described by the parabolic fit

$$\Delta\beta = 9.25 \times 10^{-4} \cdot (40 - v).^2 \tag{8.4}$$

# waveguide	1	2	3	4	5	6
distance from previous waveguide [μm]		17.602	15.73	14.80	14.29	14.07
detuning [mm$^-$1]	0.152	0.099	0.057	0.026	0.007	0
writing speed [mm/s]	27.18	29.63	32.16	34.74	37.35	40.00

Table 8.2: The table reports the values of the interwaveguide distances, the detunings and the correspondent writing speeds as derived from eq. (8.4), resulting from the solution of the IEP for a PST waveguide array with d_{min} = 14 μm and a coupling law $\kappa = 2.84 \cdot e^{-0.161 \cdot d}$. Since the array is symmetric, only half of the values are reported.

8.3.3 Fabrication of the PST waveguide array

Having established the correspondence between $\Delta\beta$ and Δv, it has been possible to implement the algorithm for the correction of the eigenvalues on the PST waveguide arrays that demonstrated the best performance, i.e. the one with d_{min} = 14 μm. Running 15 iterations of the algorithm provided the set of parameters reported in table 8.2.

We fabricated fourteen arrays with lengths varying from 24 mm to 34.4 mm (z_{PST} = 28.86 mm). Light propagation inside the arrays is shown in figure 8.5. It is evident from the maps and from the analysis on the transfer fidelity (figure 8.6) that the correction of the eigenvalues has degraded the performances of the system. For example, considering the PST 1 $\rightarrow$ 11, its transfer fidelity has dropped from 90.7% in the PST waveguide array without the correction to 67.4% in the array with the correction. This degradation is most likely related to a wrong fabrication of the corrected PST waveguide arrays: in fact, the numerical simulations of the fabricated devices do not describe well light propagation inside these structures. The closeness between the simulation and the experimental data can be evaluated introducing the *simulation fidelity*, i.e. the fidelity between the simulation and the measurement

$$F_{theo-meas} = \vec{I}_{sim} \cdot \vec{I}_{meas}$$

For the PST 1 $\rightarrow$ 11, the average simulation fidelity has dropped from 95.5% - in the uncorrected arrays - to 64.5% - in the arrays with the correc-

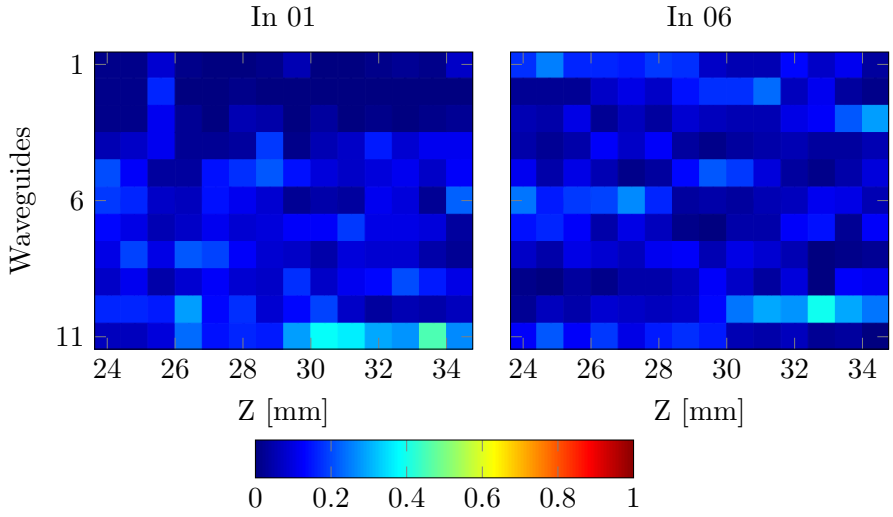

Figure 8.5: Light propagation inside the PST waveguide arrays after the eigenvalue correction. The parameters of the arrays are reported in table 8.2.

tion - thus suggesting that the detuning introduced have a different impact on the array from what we expected.

8.3.4 New characterization of $\Delta\beta{=}f(v)$

Before discarding the eigenvalue correction technique, we decided to analyse more systematically the relation between the $\Delta\beta$ and Δv.

For this reason, we decided to fabricate a new set of twenty-five directional couplers[4] with Δv from 0 mm/s to 30 mm/s. The range from 0 mm/s to 12 mm/s has been investigated with steps of 0.8 mm/s to have greater precision in a region where κ could be considered reliably constant: in fact, there is the possibility that κ may change for the couplers written with high Δv, since waveguides written with different writing speed can guide modes with different shapes, and for this reason κ may change if the range of velocities analysed is big. This allowed us to fit the experimental data directly with the equation for P_{cross} (eq. (8.3)) assuming a linear dependence $\Delta\beta{=}c\Delta v$. This time the fit converged using the previously estimated $\kappa =$

[4]The parameters of fabrication are $d = 20$ μm and $L = 17$ mm.

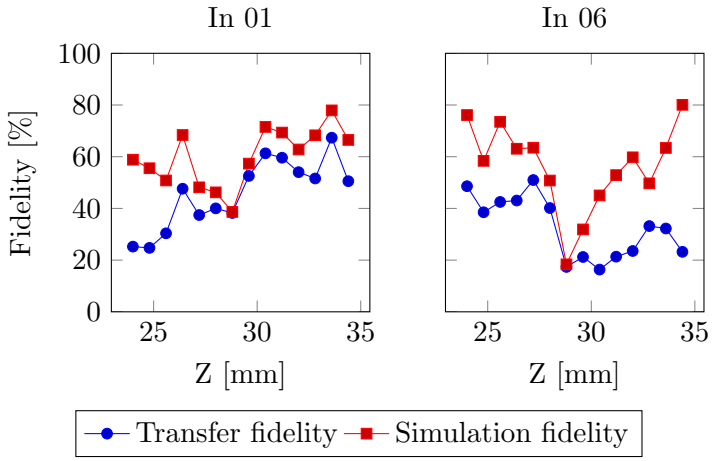

Figure 8.6: Measured transfer fidelity (blue) and fidelity with the simulation (red) of the corrected PST waveguide arrays.

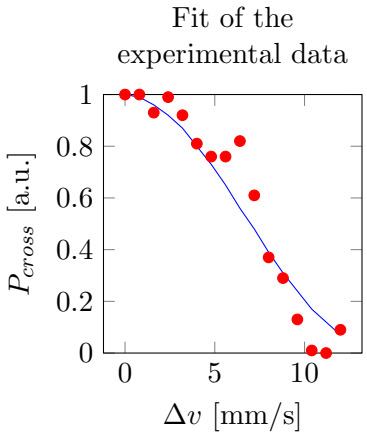

Figure 8.7: Measured P_{cross} (red dots) as function of Δv=40 – v and their fit (blue line), considering a linear dependence $\Delta\beta = c\Delta v$.

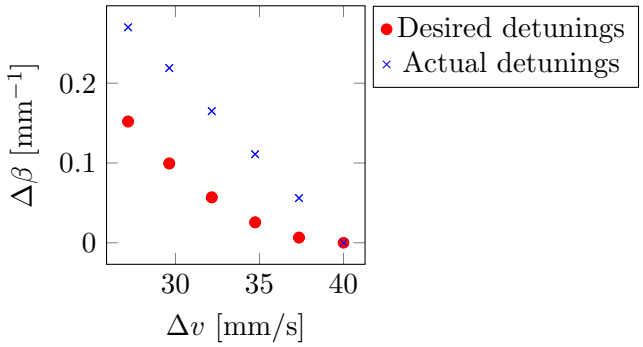

Figure 8.8: Desired and actual detunings implemented in the PST waveguide arrays with the eigenvalue correction.

0.089 mm^{-1} and provided the following relationship

$$\Delta\beta = 2.1 \times 10^{-2}\Delta v \tag{8.5}$$

This result is in agreement with the literature, which reports a linear dependence $\Delta\beta = c\Delta v$ (see, for example, Ref. [90]).

With this more precise characterization, we reconstructed the actual detunings implemented in the PST waveguide array with the eigenvalue correction. As can be seen in graph 8.8, the actual detunings are quite different from the intended ones. In addition to this, we measured the κ in a set of five uniform arrays written to monitor the reproducibility of the decay of the coupling coefficients. It resulted that the coupling law was $\kappa = 3.07e^{-0.168d}$, slightly different from the one used to fabricate the arrays.

The errors in the provided detunings, along with the small difference in the coupling law, can partially explain the reasons of the low performances of the corrected PST waveguide arrays, as shown by the increase of the simulation fidelity reported in figure 8.9, where the model used to design the corrected PST waveguide arrays is compared with the new one.

Concluding, the eigenvalue correction has not been proven successful, due to some technical issues arisen in the design and fabrication stages. With the new calibration of the relationship $\Delta\beta = f(\Delta v)$, it should be possible to implement a more precise correction of the eigenvalues with the algorithm provided above.

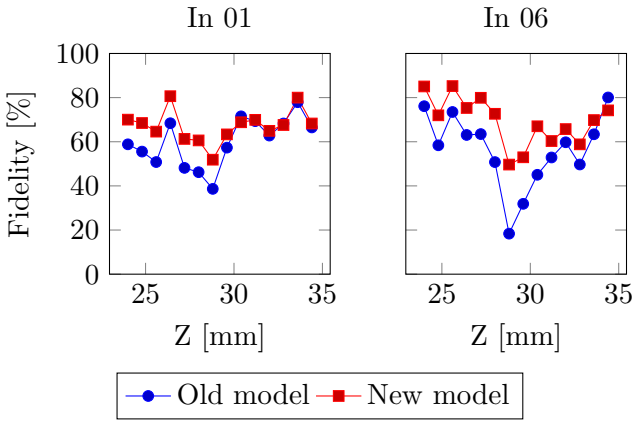

Figure 8.9: Simulation fidelities of the old - $\kappa = 2.84e^{-0.161d}$ and $\Delta\beta = 9.25 \times 10^{-4}\Delta v^2$ - and new - $\kappa = 3.07e^{-0.168d}$ and $\Delta\beta = 2.1 \times 10^{-2}\Delta v$ - models for the corrected PST waveguide arrays.

Chapter 9

Conclusions

The thesis activity has focused on the design, prototyping and analysis of a waveguide array to simulate the dynamics of a linear spin chain in order to study entanglement preservation in this kind of system.

After the optimization of the fabrication parameters, a first prototype has been developed with state-of-the-art efficiency for the state transfer between the ends of the array and with a good polarization insensitivity. The Quantum Photonic Lab of the University of Sydney has already performed some successful experiments on this device and the fidelity of the entangled state after the $1 \rightarrow 11$ propagation has been estimated around 92%.

In a second time, we have investigated both numerically and through dedicated experiments the effects of non-nearest-neighbour couplings and the possible presence of an intrinsic gradient in the propagation constants of the waveguides, to understand the causes of the degrade in the performance of the first prototype. After discarding the presence of an intrinsic detuning of the waveguides, we have tried to compensate the effect of non-nearest-neighbours by increasing the interwaveguide distances, allowing us to reach slightly higher efficiencies.

To increase further the transfer fidelity, we tried to correct the disruptive effect of the non-nearest-neighbour couplings using an algorithm to solve the inverse eigenvalue problem associated with the Hamiltonian of the system. By modulating the writing speed of the waveguides, we inscribed arrays with properly detuned waveguide to compensate for the non-nearest-neighbour effects. The trial did not bring satisfactory results, probably due to an incorrect esteem of the dependence of the detuning with the writing speed.

In conclusion, we have managed to fabricate a compact polarization insensitive waveguide array for the simulation of spin chains, that has provided interesting preliminary results; moreover, we have understood that one of the main cause of degradation in this type of device is the interference of non-nearest-neighbour couplings and we proposed a possible way to compensate this effect.

Appendices

Appendix A

Pauli matrices

Pauli matrices are a set of three 2×2 complex unitary[1] and Hermitian matrices[2]

Let the state of a spin-1/2 particle be described by the kets

$$|\downarrow\rangle = |0\rangle = \begin{pmatrix} 0 \\ 1 \end{pmatrix}$$

and

$$|\uparrow\rangle = |1\rangle = \begin{pmatrix} 1 \\ 0 \end{pmatrix}$$

In this framework, the Pauli matrices are defined as

$$\sigma^x = \begin{bmatrix} 0 & 1 \\ 1 & 0 \end{bmatrix} \tag{A.1a}$$

$$\sigma^y = \begin{bmatrix} 0 & -i \\ i & 0 \end{bmatrix} \tag{A.1b}$$

$$\sigma^z = \begin{bmatrix} 1 & 0 \\ 0 & -1 \end{bmatrix} \tag{A.1c}$$

The Pauli matrices, together with the identity matrix $I = \sigma_0 = \begin{bmatrix} 1 & 0 \\ 0 & 1 \end{bmatrix}$,

[1] Matrix U is *unitary* if $U^\dagger U = UU^\dagger = I$, where $U^\dagger$ denotes the conjugate transpose of U.

[2] The matrix A is *hermitian* if $A = A^\dagger$, where $A^\dagger$ denotes the conjugate transpose of A.

form an orthogonal basis of the complex Hilbert space of all 2×2 matrices[3].

We mention here some of their properties.

Eigenvalues and eigenvectors. Each Pauli matrix has the eigenvalues $\lambda_{1,2} = \pm 1$. The correspondent normalized eigenvectors are:

$$\psi_x^+ = \frac{1}{\sqrt{2}} \begin{pmatrix} 1 \\ 1 \end{pmatrix} \qquad \text{and} \qquad \psi_x^- = \frac{1}{\sqrt{2}} \begin{pmatrix} 1 \\ -1 \end{pmatrix} \tag{A.2a}$$

$$\psi_y^+ = \frac{1}{\sqrt{2}} \begin{pmatrix} 1 \\ i \end{pmatrix} \qquad \text{and} \qquad \psi_y^- = \frac{1}{\sqrt{2}} \begin{pmatrix} 1 \\ -i \end{pmatrix} \tag{A.2b}$$

$$\psi_z^+ = \begin{pmatrix} 1 \\ 0 \end{pmatrix} \qquad \text{and} \qquad \psi_z^- = \begin{pmatrix} 0 \\ 1 \end{pmatrix} \tag{A.2c}$$

As you can see, the vectors we used to represent the states of the spins are the eigenvectors of σ^z. This is not a coincidence and it will have profound consequences as we will see below.

Commutator. The commutator of the Pauli matrices is easily calculated and can be expressed shortly as

$$[\sigma^i, \sigma^j] = 2i\varepsilon^{i,j,k}\sigma^k \tag{A.3}$$

where $\varepsilon_{i,j,k}$ is the Levi-Civita symbol[4], so that, for example, $[\sigma^x, \sigma^y] = 2i\sigma^z$ and $[\sigma^z, \sigma^y] = -2i\sigma^x$.

Ladder operators. The ladder operators σ^+ and σ^- can be expressed as

$$\sigma^+ = \frac{\sigma^x + i\sigma^y}{2} \tag{A.4a}$$

$$\sigma^- = \frac{\sigma^x - i\sigma^y}{2} \tag{A.4b}$$

[3] In other words, all 2×2 complex matrices can be described as a linear combination of σ_0, σ^x, σ^y, σ^z.

[4] $\varepsilon_{i,j,k} = \begin{cases} 1 \text{ if } (i,j,k) = (1,2,3), (2,3,1), (3,1,2) \\ -1 \text{ if } (i,j,k) = (3,2,1), (2,1,3), (1,3,2) \\ 0 \text{ otherwise} \end{cases}$.

and have the following properties:

$$\sigma^+ |\downarrow\rangle = |\uparrow\rangle \tag{A.5a}$$
$$\sigma^+ |\uparrow\rangle = 0 \tag{A.5b}$$
$$\sigma^- |\downarrow\rangle = 0 \tag{A.5c}$$
$$\sigma^- |\uparrow\rangle = |\downarrow\rangle \tag{A.5d}$$

Notice that σ^+ raises $|\downarrow\rangle$ to $|\uparrow\rangle$, while σ^- lowers $|\uparrow\rangle$ to $|\downarrow\rangle$.

Appendix B

Mathematical analysis of the XXX Hamiltonian

Let us consider the XXX model, whose Hamiltonian reads

$$\mathcal{H} = \sum_{<i,j>} J_{i,j}(\sigma_i^x \sigma_j^x + \sigma_i^y \sigma_j^y + \sigma_i^z \sigma_j^z) + \sum_i B_i \sigma_i^z$$

Since it is an isotropic model, throughout the calculation we will consider $J_{i,j} = 1 \ \forall i, j$ without losing generality.

B.1 Commutation relationship $[\mathcal{H}, \sum_i \sigma_i^z] = 0$

To begin with, recall that the commutator of a sum of operator is equal to the sum of their commutators, i.e. $[A, B + C] = [A, B] + [A, C]$. We can thus simplify

$$[\mathcal{H}, \sum_k \sigma_k^z] = \sum_k [\mathcal{H}, \sigma_k^z]$$

and focus our attention on the term

$$[\mathcal{H}, \sigma_k^z] = \sum_{<i,j>} [\vec{\sigma}_i \cdot \vec{\sigma}_j, \sigma_k^z] + \sum_i B_i [\sigma_i^z, \sigma_k^z]$$

The term $\sum_i B_i [\sigma_i^z, \sigma_k^z]$ in the last equation is zero since $[\sigma_i^z, \sigma_j^z] = 0$, $\forall \, i, j$, and we can neglect henceforth. As regards the term $\sum_{<i,j>} [\vec{\sigma}_i \cdot \vec{\sigma}_j, \sigma_k^z]$, it can be simplified considering that, if $k \neq i$ and $k \neq j$, then the matrices act on different spins, so they commute: $[\sigma_i, \sigma_j] = 0$.

We can thus restrict our analysis to the case $k = i$ and $k = j$ and expand

$$\begin{aligned}
&[\mathcal{H}, \sigma_i^z] + [\mathcal{H}, \sigma_j^z] = \\
&\quad = \sum_{<i,j>} [\sigma_i^x\sigma_j^x + \sigma_i^y\sigma_j^y + \sigma_i^z\sigma_j^z, \sigma_i^z] + [\sigma_i^x\sigma_j^x + \sigma_i^y\sigma_j^y + \sigma_i^z\sigma_j^z, \sigma_j^z] = \\
&= \sum_{<i,j>} \Big\{\sigma_i^x\sigma_j^x\sigma_i^z + \sigma_i^y\sigma_j^y\sigma_i^z + \sigma_i^z\sigma_j^z\sigma_i^z - \sigma_i^z\sigma_i^x\sigma_j^x - \sigma_i^z\sigma_i^y\sigma_j^y - \sigma_i^z\sigma_i^z\sigma_j^z + \\
&\quad + \sigma_i^x\sigma_j^x\sigma_j^z + \sigma_i^y\sigma_j^y\sigma_j^z + \sigma_i^z\sigma_j^z\sigma_j^z - \sigma_j^z\sigma_i^x\sigma_j^x - \sigma_j^z\sigma_i^y\sigma_j^y - \sigma_j^z\sigma_i^z\sigma_j^z\Big\}
\end{aligned}$$

Now, we can simplify the expression following this criteria:

- Matrices acting on different spins commute.
- $\sigma_i^z\sigma_i^z = 1$

Hence

$$\begin{aligned}
&\sum_{<i,j>} \Big\{\sigma_j^x\sigma_i^x\sigma_i^z + \sigma_j^y\sigma_i^y\sigma_i^z + \sigma_j^z - \sigma_j^x\sigma_i^z\sigma_i^x - \sigma_j^y\sigma_i^z\sigma_i^y - \sigma_j^z + \\
&\qquad + \sigma_i^x\sigma_j^x\sigma_j^z + \sigma_i^y\sigma_j^y\sigma_j^z + \sigma_i^z - \sigma_i^x\sigma_j^z\sigma_j^x - \sigma_i^y\sigma_j^z\sigma_j^y - \sigma_i^z\Big\} = \\
&\qquad = \sum_{<i,j>} \Big\{\sigma_j^x(\sigma_i^x\sigma_i^z - \sigma_i^z\sigma_i^x) + \sigma_j^y(\sigma_i^y\sigma_i^z - \sigma_i^z\sigma_i^y) + \\
&\qquad\quad + \sigma_i^x(\sigma_j^x\sigma_j^z - \sigma_j^z\sigma_j^x) + \sigma_i^y(\sigma_j^y\sigma_j^z - \sigma_j^z\sigma_j^y)\Big\} = \\
&\qquad\quad = \sum_{<i,j>} \Big\{\sigma_j^x[\sigma_i^x, \sigma_i^z] + \sigma_j^y[\sigma_i^y, \sigma_i^z] + \sigma_i^x[\sigma_j^x, \sigma_j^z] + \sigma_i^y[\sigma_j^y\sigma_j^z]\Big\}
\end{aligned}$$

Summarizing,

$$[\mathcal{H}, \sum_i \sigma_i^z] = \sum_{<i,j>} \Big\{\sigma_j^x[\sigma_i^x, \sigma_i^z] + \sigma_j^y[\sigma_i^y, \sigma_i^z] + \sigma_i^x[\sigma_j^x, \sigma_j^z] + \sigma_i^y[\sigma_j^y\sigma_j^z]\Big\}$$

Since $[\sigma^\alpha, \sigma^\beta] = 2i\varepsilon^{\alpha\beta\gamma}\sigma^\gamma$

$$[\mathcal{H}, \sum_k \sigma_k^z] = 2i \sum_{<i,j>} \sigma_i^y\sigma_j^x - \sigma_j^x\sigma_i^y + \sigma_j^y\sigma_i^x - \sigma_i^x\sigma_j^y = 0 \ \blacksquare$$

B.2 Development in the first excitation subspace

As mentioned in chapter 1, the state of a system of N particles is described by a vector in a 2^N-dimensional Hilbert space. Anyway, in the case of a N-particle spin chain described by an XXX Hamiltonian a major simplification applies. In fact, since $[\mathcal{H}, \sum_k \sigma_k^z] = 0$, the Hamiltonian preserves the number of excited spins in the system: this means that the 2^N-dimensional Hilbert space is subdivided into many subspaces, each one characterized by a constant number of excited spins. For this reason, considering the simplest protocol for spin chains where only one spin is excited by the sender, we can restrict our analysis into the single excitation subspace, spanned by the states[1]

$$|j\rangle = |0\rangle^{\otimes j-1} |1\rangle |0\rangle^{\otimes N-j}$$

Moreover, since $\sigma_i^z \sigma_j^z |k\rangle = 0$ for every possible $\{i, j, k\}$, we can analyse a reduced form of $\mathcal{H}$:

$$\mathcal{H} = \sum_{<i,j>} J_{i,j}(\sigma_i^x \sigma_j^x + \sigma_i^y \sigma_j^y) + \sum_i B_i \sigma_i^z$$

Introducing the ladder operators

$$\sigma^{\pm} = \sigma^x \pm i\sigma^y$$

we can extract σ^x and σ^y

$$\begin{cases} \sigma^x &= \sigma^+ + \sigma^- \\ \sigma^y &= -i(\sigma^+ - \sigma^-) \end{cases}$$

Hence

$$\mathcal{H} = \sum_{<i,j>} J_{i,j}(\sigma_i^+ \sigma_j^- + \sigma_i^- \sigma_j^+) + \sum_i B_i \sigma_i^z$$

The passages above are formally correct, but introduce wrong commutation relationships for the fermions in the spin chain; in fact, $[\sigma_i^+, \sigma_j^-] = 0$ for $i \neq j$, so spins on different sites commutes, while fermions should anticommute. For this reason, it is necessary to introduce the Jordan-Wigner

[1] This notation is the same adopted for the description of spin chains in single excitation subspace in chapter 2, with the difference that here the state is indicated in roman (instead of boldface).

transformations

$$\begin{cases} a_j^\dagger = e^{+i\pi \sum_{k=1}^{j-1} \sigma_j^+ \sigma_j^-} \sigma_j^+ \\ a_j = e^{-i\pi \sum_{k=1}^{j-1} \sigma_j^+ \sigma_j^-} \sigma_j^- \\ a_j^\dagger a_j - \frac{1}{2} = \sigma_j^+ \sigma_j^- - \frac{1}{2} \end{cases} \tag{B.1}$$

where $a_i^\dagger$ and a_i are the creation and destruction operators of the non-interacting fermion on site j introduced by the Jordan-Wigner transformation.

With these relations, the Hamiltonian can be correctly rewritten as

$$\mathcal{H} = \sum_{<i,j>} J_{i,j}(a_i^\dagger a_j + a_j^\dagger a_i) + 2\sum_i B_i a_i^\dagger a_i$$

Considering only a nearest-neighbour coupling,

$$H = \sum_{j=1}^{N-1} J_{j,j+1}(a_j^\dagger a_{j+1} + a_j a_{j+1}^\dagger) + \sum_{j=1}^{N} 2B_j a_j^\dagger a_j$$

We can rewrite this last expression in the chosen basis of the space $|n\rangle$:

$$H = \sum_{j=1}^{N-1} J_{j,j+1}(|j+1\rangle\langle j| + |j\rangle\langle j+1|) + \sum_{j=1}^{N} 2B_j |j\rangle\langle j|$$

Imposing $\hbar = 1$, the evolution of the system is given by Schrödinger's equation

$$i\frac{d|\psi\rangle}{dt} = H|\psi\rangle$$

We can write ψ in the basis $|i\rangle$

$$|\psi\rangle = \sum_{i=0}^{N} A_i(t)|i\rangle$$

Hence

$$i\frac{d|\psi\rangle}{dt} = H|\psi\rangle \Rightarrow$$

$$i\frac{d}{dt}\sum_{i=0}^{N} A_i(t)\,|i\rangle = \sum_{j=1}^{N} J_{j,j+1}(|j+1\rangle\langle j+1| + |j\rangle\langle j+1|)\cdot\sum_{i=0}^{N} A_i(t)\,|i\rangle + \\ + \sum_{j=1}^{N} 2B_j\,|j\rangle\langle j|\cdot\sum_{i=0}^{N} A_i(t)\,|i\rangle \Rightarrow$$

$$i\sum_{i=0}^{N}|i\rangle\,\frac{dA_i(t)}{dt} = \sum_{j=1}^{N-1}\sum_{i=0}^{N} A_i(t)J_{j,j+1}\left(|j+1\rangle\langle j|\,i\rangle + |j\rangle\langle j+1|\,i\rangle\right) + \\ + \sum_{j=1}^{N}\sum_{i=0}^{N} A_i(t)2B_j\,|j\rangle\langle j|i\rangle$$

The elements in the right hand side are different from zero iff $j = i$ or $j+1 = i$, hence

$$i\sum_{i=0}^{N}|i\rangle\,\frac{dA_i(t)}{dt} = \sum_{i=2}^{N-1} A_i(t)(J_{i,i+1}\,|i+1\rangle + J_{i-1,i}\,|i-1\rangle) + \sum_{i=1}^{N} 2B_i\,|i\rangle$$

Left-multiplying for the generic $\langle k|$, we get

$$i\sum_{i=0}^{N}\langle k\,|i\rangle\,\frac{dA_i(t)}{dt} = \sum_{i=0}^{N} A_i(t)(J_{i,i+1}\,\langle k\,|i+1\rangle + J_{i-1,i}\,\langle k\,|i-1\rangle) + \sum_{i=1}^{N} 2B_i\,\langle k|i\rangle$$

$$i\frac{dA_k(t)}{dt} = J_{k,k+1}A_{k+1}(t) + J_{k-1,k}A_{k-1}(t) + 2B_iA_k(t)$$

that can be written in the matrical form

$$i\frac{d}{dt}\underline{A} = \underline{\underline{M}}\cdot\underline{A}$$

where

$$\underline{\underline{M}} = \begin{bmatrix} 2B_1 & J_{1,2} & 0 & \cdots & 0 \\ J_{1,2} & 2B_2 & J_{2,3} & \cdots & 0 \\ 0 & J_{2,3} & 2B_3 & \cdots & 0 \\ \vdots & \vdots & \vdots & \ddots & J_{N-1,N} \\ 0 & 0 & 0 & J_{N-1,N} & 2B_N \end{bmatrix} \tag{B.2}$$

Bibliography

[1] R. S. Ingarden, "Quantum information theory", *Reports on Mathematical Physics*, vol. 10, no. 1, 1976.

[2] M. Keyl, "Fundamentals of quantum information theory", *Physics Reports*, vol. 369, no. 5, 2002.

[3] P. W. Shor, "Algorithms for quantum computation: discrete logarithms and factoring", in *Foundations of Computer Science, 1994 Proceedings., 35th Annual Symposium on*, IEEE, 1994.

[4] P. Shor, "Polynomial-time algorithms for prime factorization and discrete logarithms on a quantum computer", *SIAM Journal on Computing*, vol. 26, no. 5, 1997.

[5] C. Pomerance, "A tale of two sieves", *Notices Amer. Math. Soc*, vol. 43, 1996.

[6] R. P. Feynman, "Simulating physics with computers", *International journal of theoretical physics*, vol. 21, no. 6, 1982.

[7] S. Somaroo, C. H. Tseng, T. F. Havel, R. Laflamme, and D. G. Cory, "Quantum simulations on a quantum computer", *Phys. Rev. Lett.*, vol. 82, 26 1999.

[8] C. H. Tseng, S. Somaroo, Y. Sharf, E. Knill, R. Laflamme, T. F. Havel, and D. G. Cory, "Quantum simulation of a three-body-interaction hamiltonian on an nmr quantum computer", *Phys. Rev. A*, vol. 61, 1 1999.

[9] J. Du, N. Xu, X. Peng, P. Wang, S. Wu, and D. Lu, "Nmr implementation of a molecular hydrogen quantum simulation with adiabatic state preparation", *Phys. Rev. Lett.*, vol. 104, 3 2010.

[10] C. H. Bennett and G. Brassard, "Quantum cryptography: public key distribution and coin tossing.", in *Proceedings of IEEE International Conference on Computers, Systems and Signal Processing.*, vol. 175, 1984.

[11] P. W. Shor and J. Preskill, "Simple proof of security of the bb84 quantum key distribution protocol", *Phys. Rev. Lett.*, vol. 85, 2 2000.

[12] C. H. Bennett, F. Bessette, G. Brassard, L. Salvail, and J. Smolin, "Experimental quantum cryptography", English, *Journal of Cryptology*, vol. 5, no. 1, 1992.

[13] C. H. Bennett and D. P. DiVincenzo, "Quantum information and computation", *Nature*, vol. 404, no. 6775, 2000.

[14] T. D. Ladd, F. Jelezko, R. Laflamme, Y. Nakamura, C. Monroe, and J. L. O'Brien, "Quantum computers", *Nature*, vol. 464, no. 7285, 2010.

[15] A. S. Holevo, "Bounds for the quantity of information transmitted by a quantum communication channel", *Problemy Peredachi Informatsii*, vol. 9, no. 3, 1973.

[16] C. H. Bennett, G. Brassard, C. Crépeau, R. Jozsa, A. Peres, and W. K. Wootters, "Teleporting an unknown quantum state via dual classical and einstein-podolsky-rosen channels", *Phys. Rev. Lett.*, vol. 70, 13 1993.

[17] W. K. Wootters and W. H. Zurek, "A single quantum cannot be cloned", *Nature*, vol. 299, no. 5886, 1982.

[18] J. Preskill, "Reliable quantum computers", *Proceedings of the Royal Society of London. Series A: Mathematical, Physical and Engineering Sciences*, vol. 454, no. 1969, 1998.

[19] E. Knill, R. Laflamme, and G. J. Milburn, "A scheme for efficient quantum computation with linear optics", *Nature*, vol. 409, no. 6816, 2001.

[20] C. Negrevergne, T. S. Mahesh, C. A. Ryan, M. Ditty, F. Cyr-Racine, W. Power, N. Boulant, T. Havel, D. G. Cory, and R. Laflamme, "Benchmarking quantum control methods on a 12-qubit system", *Phys. Rev. Lett.*, vol. 96, 17 2006.

[21] J. A. Jones and M. Mosca, "Implementation of a quantum algorithm on a nuclear magnetic resonance quantum computer", *The Journal of chemical physics*, vol. 109, no. 5, 1998.

[22] I. L. Chuang, L. M. K. Vandersypen, X. Zhou, D. W. Leung, and S. Lloyd, "Experimental realization of a quantum algorithm", *Nature*, vol. 393, no. 6681, 1998.

[23] J. A. Jones, M. Mosca, and R. H. Hansen, "Implementation of a quantum search algorithm on a quantum computer", *Nature*, vol. 393, no. 6683, 1998.

[24] L. M. K. Vandersypen, M. Steffen, G. Breyta, C. S. Yannoni, M. H. Sherwood, and I. L. Chuang, "Experimental realization of shor's quantum factoring algorithm using nuclear magnetic resonance", *Nature*, vol. 414, no. 6866, 2001.

[25] C. Ospelkaus, C. E. Langer, J. M. Amini, K. R. Brown, D. Leibfried, and D. J. Wineland, "Trapped-ion quantum logic gates based on oscillating magnetic fields", *Phys. Rev. Lett.*, vol. 101, 9 2008.

[26] B. E. Kane, "A silicon-based nuclear spin quantum computer", *Nature*, vol. 393, no. 6681, 1998.

[27] L. DiCarlo, J. M. Chow, J. M. Gambetta, L. S. Bishop, B. R. Johnson, D. I. Schuster, J. Majer, A. Blais, L. Frunzio, S. M. Girvin, and R. J. Schoelkopf, "Demonstration of two-qubit algorithms with a superconducting quantum processor", *Nature*, vol. 460, no. 7252, 2009.

[28] J. J. L. Morton, A. M. Tyryshkin, A. Ardavan, S. C. Benjamin, K. Porfyrakis, S. A. Lyon, and G. A. D. Briggs, "Bang-bang control of fullerene qubits using ultrafast phase gates", *Nat Phys*, vol. 2, no. 1, 2006.

[29] N. Mason, M. Biercuk, and C. Marcus, "Local gate control of a carbon nanotube double quantum dot", *Science*, vol. 303, no. 5658, 2004.

[30] B. Trauzettel, D. V. Bulaev, D. Loss, and G. Burkard, "Spin qubits in graphene quantum dots", *Nat Phys*, vol. 3, no. 3, 2007.

[31] J. I. Cirac, P. Zoller, H. J. Kimble, and H. Mabuchi, "Quantum state transfer and entanglement distribution among distant nodes in a quantum network", *Phys. Rev. Lett.*, vol. 78, 16 1997.

[32] S. J. van Enk, J. I. Cirac, and P. Zoller, "Ideal quantum communication over noisy channels: a quantum optical implementation", *Phys. Rev. Lett.*, vol. 78, 22 1997.

[33] T. Pellizzari, "Quantum networking with optical fibres", *Phys. Rev. Lett.*, vol. 79, 26 1997.

[34] A. S. Parkins and H. J. Kimble, "Quantum state transfer between motion and light", *Journal of Optics B: Quantum and Semiclassical Optics*, vol. 1, no. 4, 1999.

[35] S. Bose, "Quantum communication through an unmodulated spin chain", *Phys. Rev. Lett.*, vol. 91, 20 2003.

[36] A. Kay, "Perfect, efficient, state transfer and its application as a constructive tool", *International Journal of Quantum Information*, vol. 8, no. 04, 2010.

[37] G. M. Nikolopoulos and I. Jex, *Quantum state transfer and network engineering*. Springer, 2014.

[38] P. Cappellaro, C. Ramanathan, and D. G. Cory, "Dynamics and control of a quasi-one-dimensional spin system", *Phys. Rev. A*, vol. 76, 3 2007.

[39] J. Zhang, M. Ditty, D. Burgarth, C. A. Ryan, C. M. Chandrashekar, M. Laforest, O. Moussa, J. Baugh, and R. Laflamme, "Quantum data bus in dipolar coupled nuclear spin qubits", *Phys. Rev. A*, vol. 80, 1 2009.

[40] C. Ramanathan, P. Cappellaro, L. Viola, and D. G. Cory, "Experimental characterization of coherent magnetization transport in a one-dimensional spin system", *New Journal of Physics*, vol. 13, no. 10, 2011.

[41] M. Bellec, G. M. Nikolopoulos, and S. Tzortzakis, "Faithful communication hamiltonian in photonic lattices", *Opt. Lett.*, vol. 37, no. 21, 2012.

[42] A. Perez-Leija, R. Keil, A. Kay, H. Moya-Cessa, S. Nolte, L.-C. Kwek, B. M. Rodriguez-Lara, A. Szameit, and D. N. Christodoulides, "Coherent quantum transport in photonic lattices", *Phys. Rev. A*, vol. 87, 1 2013.

[43] A. Perez-Leija, R. Keil, H. Moya-Cessa, A. Szameit, and D. N. Christodoulides, "Perfect transfer of path-entangled photons in j_x photonic lattices", *Phys. Rev. A*, vol. 87, 2 2013.

[44] C. A. Fuchs and C. M. Caves, "Ensemble-dependent bounds for accessible information in quantum mechanics", *Phys. Rev. Lett.*, vol. 73, 23 1994.

[45] M. Christandl, N. Datta, A. Ekert, and A. J. Landahl, "Perfect state transfer in quantum spin networks", *Phys. Rev. Lett.*, vol. 92, 18 2004.

[46] C. Albanese, M. Christandl, N. Datta, and A. Ekert, "Mirror inversion of quantum states in linear registers", *Phys. Rev. Lett.*, vol. 93, 23 2004.

[47] M. Horodecki, P. Horodecki, and R. Horodecki, "General teleportation channel, singlet fraction, and quasidistillation", *Phys. Rev. A*, vol. 60, 3 1999.

[48] L. Landau and E. Lifshitz, *Quantum Mechanics: Non-Relativistic Theory*. Ser. Course of Theoretical Physics. Pergamon Press, 1977, vol. Vol. 3.

[49] P. Dirac, *The Principles of Quantum Mechanics*. Oxford University Press, 1958.

[50] P. W. Anderson, "Absence of diffusion in certain random lattices", *Phys. Rev.*, vol. 109, 5 1958.

[51] G. De Chiara, D. Rossini, S. Montangero, and R. Fazio, "From perfect to fractal transmission in spin chains", *Phys. Rev. A*, vol. 72, 1 2005.

[52] J.-M. Cai, Z.-W. Zhou, and G.-C. Guo, "Decoherence effects on the quantum spin channels", *Phys. Rev. A*, vol. 74, 2 2006.

[53] F. Caruso, A. W. Chin, A. Datta, S. F. Huelga, and M. B. Plenio, "Highly efficient energy excitation transfer in light-harvesting complexes: the fundamental role of noise-assisted transport", *The Journal of Chemical Physics*, vol. 131, no. 10, 105106, 2009.

[54] Z. Mádi, B. Brutscher, T. Schulte-Herbrüggen, R. Brüschweiler, and R. Ernst, "Time-resolved observation of spin waves in a linear chain of nuclear spins", *Chemical Physics Letters*, vol. 268, no. 3, 1997.

[55] J. Zhang, G. L. Long, W. Zhang, Z. Deng, W. Liu, and Z. Lu, "Simulation of heisenberg xy interactions and realization of a perfect state transfer in spin chains using liquid nuclear magnetic resonance", *Phys. Rev. A*, vol. 72, 1 2005.

[56] J. Zhang, X. Peng, and D. Suter, "Speedup of quantum-state transfer by three-qubit interactions: implementation by nuclear magnetic resonance", *Phys. Rev. A*, vol. 73, 6 2006.

[57] G. A. Álvarez, M. Mishkovsky, E. P. Danieli, P. R. Levstein, H. M. Pastawski, and L. Frydman, "Perfect state transfers by selective quantum interferences within complex spin networks", *Phys. Rev. A*, vol. 81, 6 2010.

[58] A. Yariv, "Coupled-mode theory for guided-wave optics", *Quantum Electronics, IEEE Journal of*, vol. 9, no. 9, 1973.

[59] A. Szameit, F. Dreisow, T. Pertsch, S. Nolte, and A. Tünnermann, "Control of directional evanescent coupling in fs laser written waveguides", *Optics express*, vol. 15, no. 4, 2007.

[60] L. Sansoni, F. Sciarrino, G. Vallone, P. Mataloni, A. Crespi, R. Ramponi, and R. Osellame, "Two-particle bosonic-fermionic quantum walk via integrated photonics", *Phys. Rev. Lett.*, vol. 108, 1 2012.

[61] J. C. F. Matthews, K. Poulios, J. D. A. Meinecke, A. Politi, A. Peruzzo, N. Ismail, K. Wörhoff, M. G. Thompson, and J. L. O'Brien, "Observing fermionic statistics with photons in arbitrary processes", *Sci. Rep.*, vol. 3, 2013.

[62] K. M. Davis, K. Miura, N. Sugimoto, and K. Hirao, "Writing waveguides in glass with a femtosecond laser", *Opt. Lett.*, vol. 21, no. 21, 1996.

[63] M. Lenzner, J. Krüger, S. Sartania, Z. Cheng, C. Spielmann, G. Mourou, W. Kautek, and F. Krausz, "Femtosecond optical breakdown in dielectrics", *Phys. Rev. Lett.*, vol. 80, 18 1998.

[64] A Kaiser, B Rethfeld, M Vicanek, and G Simon, "Microscopic processes in dielectrics under irradiation by subpicosecond laser pulses", *Physical Review B*, vol. 61, no. 17, 2000.

[65] A. M. Streltsov and N. F. Borrelli, "Study of femtosecond-laser-written waveguides in glasses", *J. Opt. Soc. Am. B*, vol. 19, no. 10, 2002.

[66] L. Keldysh, "Ionization in the field of a strong electromagnetic wave", *Sov. Phys. JETP*, vol. 20, no. 5, 1965.

[67] G. Cerullo, R. Osellame, S. Taccheo, M. Marangoni, D. Polli, R. Ramponi, P. Laporta, and S. De Silvestri, "Femtosecond micromachining of symmetric waveguides at 1.5 μm by astigmatic beam focusing", *Opt. Lett.*, vol. 27, no. 21, 2002.

[68] R. Osellame, S. Taccheo, M. Marangoni, R. Ramponi, P. Laporta, D. Polli, S. D. Silvestri, and G. Cerullo, "Femtosecond writing of active optical waveguides with astigmatically shaped beams", *J. Opt. Soc. Am. B*, vol. 20, no. 7, 2003.

[69] S. Eaton, H. Zhang, P. Herman, F. Yoshino, L. Shah, J. Bovatsek, and A. Arai, "Heat accumulation effects in femtosecond laser-written waveguides with variable repetition rate", *Opt. Express*, vol. 13, no. 12, 2005.

[70] G. Della Valle, R. Osellame, and P. Laporta, "Micromachining of photonic devices by femtosecond laser pulses", *Journal of Optics A: Pure and Applied Optics*, vol. 11, no. 1, 2009.

[71] S Nolte, M Will, J Burghoff, and A Tuennermann, "Femtosecond waveguide writing: a new avenue to three-dimensional integrated optics", *Applied Physics A*, vol. 77, no. 1, 2003.

[72] A. M. Kowalevicz, V. Sharma, E. P. Ippen, J. G. Fujimoto, and K. Minoshima, "Three-dimensional photonic devices fabricated in glass by use of a femtosecond laser oscillator", *Opt. Lett.*, vol. 30, no. 9, 2005.

[73] G. Li, K. A. Winick, A. A. Said, M. Dugan, and P. Bado, "Waveguide electro-optic modulator in fused silica fabricated by femtosecond laser direct writing and thermal poling", *Opt. Lett.*, vol. 31, no. 6, 2006.

[74] T. Pertsch, U. Peschel, F. Lederer, J. Burghoff, M. Will, S. Nolte, and A. Tünnermann, "Discrete diffraction in two-dimensional arrays of coupled waveguides in silica", *Opt. Lett.*, vol. 29, no. 5, 2004.

[75] A. Szameit, D. Blömer, J. Burghoff, T. Pertsch, S. Nolte, and A. Tünnermann, "Hexagonal waveguide arrays written with fs-laser pulses", English, *Applied Physics B*, vol. 82, no. 4, 2006.

[76] I. L. Garanovich, A. Szameit, A. A. Sukhorukov, T. Pertsch, W. Krolikowski, S. Nolte, D. Neshev, A. Tünnermann, and Y. S. Kivshar, "Diffraction control in periodically curved two-dimensional waveguide arrays", *Opt. Express*, vol. 15, no. 15, 2007.

[77] A. Szameit, H. Trompeter, M. Heinrich, F. Dreisow, U. Peschel, T. Pertsch, S. Nolte, F. Lederer, and A. Tünnermann, "Fresnel's laws in discrete optical media", *New Journal of Physics*, vol. 10, no. 10, 2008.

[78] S. Longhi, "Quantum-optical analogies using photonic structures", *Laser & Photonics Reviews*, vol. 3, no. 3, 2009.

[79] A. Szameit, T. Pertsch, S. Nolte, A. Tünnermann, U. Peschel, and F. Lederer, "Optical bloch oscillations in general waveguide lattices", *J. Opt. Soc. Am. B*, vol. 24, no. 10, 2007.

[80] A. Crespi, R. Ramponi, R. Osellame, L. Sansoni, I. Bongioanni, F. Sciarrino, G. Vallone, and P. Mataloni, "Integrated photonic quantum gates for polarization qubits", *Nat Commun*, vol. 2, 2011.

[81] A. Crespi, G. Corrielli, G. D. Valle, R. Osellame, and S. Longhi, "Dynamic band collapse in photonic graphene", *New Journal of Physics*, vol. 15, no. 1, 2013.

[82] R. Keil, A. Szameit, F. Dreisow, M. Heinrich, S. Nolte, and A. Tünnermann, "Photon correlations in two-dimensional waveguide arrays and their classical estimate", *Phys. Rev. A*, vol. 81, 2 2010.

[83] R. Keil, F. Dreisow, M. Heinrich, A. Tünnermann, S. Nolte, and A. Szameit, "Classical characterization of biphoton correlation in waveguide lattices", *Phys. Rev. A*, vol. 83, 1 2011.

[84] J. O. Owens, M. A. Broome, D. N. Biggerstaff, M. E. Goggin, A Fedrizzi, T Linjordet, M Ams, G. D. Marshall, J Twamley, M. J. Withford, and A. G. White, "Two-photon quantum walks in an elliptical direct-write waveguide array", *New Journal of Physics*, vol. 13, no. 7, 2011.

[85] K. Poulios, R. Keil, D. Fry, J. D. A. Meinecke, J. C. F. Matthews, A. Politi, M. Lobino, M. Gräfe, M. Heinrich, S. Nolte, A. Szameit, and J. L. O'Brien, "Quantum walks of correlated photon pairs in two-dimensional waveguide arrays", *Phys. Rev. Lett.*, vol. 112, 14 2014.

[86] A. Killi, A. Steinmann, J. Dörring, U. Morgner, M. J. Lederer, D. Kopf, and C. Fallnich, "High-peak-power pulses from a cavity-dumped $yb : ky(wo_4)_2$ oscillator", *Opt. Lett.*, vol. 30, no. 14, 2005.

[87] D. F. V. James, P. G. Kwiat, W. J. Munro, and A. G. White, "Measurement of qubits", *Phys. Rev. A*, vol. 64, 5 2001.

[88] M. T. Chu, "Inverse eigenvalue problems", *SIAM review*, vol. 40, no. 1, 1998.

[89] A. Kay, "Perfect state transfer: beyond nearest-neighbor couplings", *Phys. Rev. A*, vol. 73, 3 2006.

[90] G. Corrielli, A. Crespi, G. Della Valle, S. Longhi, and R. Osellame, "Fractional bloch oscillations in photonic lattices", *Nat Commun*, vol. 4, 2013.

Ringraziamenti

Mi ero ripromesso di non scrivere ringraziamenti, avendoli sempre trovati fuori luogo all'interno di una tesi di laurea. Eppure, giunto al termine di questo lavoro e di questi anni universitari, non posso non ringraziare alcune persone che hanno reso possibile tutto questo.

Innanzi tutto, ringrazio in professor Osellame per avermi accolto nel suo gruppo di lavoro, dimostrandomi costantemete stima e fiducia. Un grande grazie va anche ad Andrea Crespi, che con infinita pazienza mi ha accompagnato, sopportato ed soprattutto introdotto all'arte della fabbricazione a femtosecondi.

Non posso non ringraziare Davide per i momenti di nerdaggine ignorante e per i profondi scambi socio-filosofico-politico-culturali, sempre fonte di interessante riflessioni.

Un ringraziamento speciale alla mia famiglia, per i sacrifici fatti (economici e affettivi) e soprattutto per avermi sempre donato il luogo più bello dove crescere.

Infine ringrazio Melania, per la sua costante presenza, per il suo infinito supporto, perché mi ha donato un futuro da progettare insieme.